AD NUMBER

AD473862

LIMITATION CHANGES

TO:

Approved for public release; distribution is unlimited.

FROM:

Distribution authorized to U.S. Gov't. agencies only; Administrative/Operational Use; SEP 1965. Other requests shall be referred to Office of Naval Research, Washington, DC 20360.

AUTHORITY

ONR ltr 4 May 1977

SECURITY MARKING

The classified or limited status of this report applies to each page, unless otherwise marked.
Separate page printouts MUST be marked accordingly.

HTC-AD 65-15

Volume I

SUMMARY TECHNICAL REPORT
ROTOR/WING CONCEPT STUDY

September 1965

HUGHES TOOL COMPANY · AIRCRAFT DIVISION
Culver City, California

HTC-AD 65-15

Volume I

SUMMARY TECHNICAL REPORT
ROTOR/WING CONCEPT STUDY

September 1965

Prepared by Robert E. Head

Contract Number: Nonr-4588(00)
Authority: NR 212-162/12-8-64

An Experimental Research Program sponsored by Air Programs, Office of Naval Research, and Airframe Design Division, Bureau of Naval Weapons, U. S. Navy

HUGHES TOOL COMPANY -- AIRCRAFT DIVISION
Culver City, California

FOREWORD

This report presents the results of whirlstand and wind tunnel tests of a one-sixth scale model of the Rotor/Wing high-speed VTOL aircraft. The main body of the report, presented as Volume I, discusses highlights of the test results, includes a discussion of the application of the test results to full-scale, and describes the characteristics of such an aircraft. Volume II, which includes Appendixes A through F, contains detailed analyses and test data from the model research program. Volume III*, which includes Appendixes G and H, contains a collection of the detailed drawings of the model and the stress analysis used in the design.

*Because of the specialized nature of the information in Volume III, Volume III is not given wide distribution. If copies are desired, they may be obtained from DDC with prior approval of Air Programs, Office of Naval Research.

TABLE OF CONTENTS

	Page
FOREWORD	I-ii
LIST OF ILLUSTRATIONS	I-iv
SUMMARY	I-vii
INTRODUCTION	I-1
DESCRIPTION OF MODEL	I-11
General Arrangement	I-11
Installation	I-12
Systems	I-13
ANALYSES OF DYNAMIC CHARACTERISTICS	I-31
Natural Frequencies	I-31
Rotor Flutter Characteristics	I-32
Conversion Characteristics	I-32
WIND TUNNEL TESTS	I-35
Powered Rotor	I-37
Autorotating Rotor	I-42
Conversion	I-43
Stopped-Rotor	I-47
APPLICATIONS TO FULL-SCALE ROTOR/WING AIRCRAFT	I-91
CONCLUSIONS AND RECOMMENDATIONS	I-103
REFERENCES	I-105
DISTRIBUTION LIST	I-106

LIST OF ILLUSTRATIONS

Figure		Page
1	Rotor/Wing Wind Tunnel Model.	I-ix
2	Rotor/Wing Flight Modes.	I-5
3	Propulsion System Schematic	I-6
4	Rotor/Wing Model Whirlstand - Hughes Tool Company, Aircraft Division	I-7
5	Rotor/Wing Wind Tunnel Model, Series I - David Taylor Model Basin Aerodynamics Laboratory	I-8
6	Rotor/Wing Wind Tunnel Model, Series II - David Taylor Model Basin Aerodynamics Laboratory	I-9
7	Rotor/Wing Wind Tunnel Model, Series III - David Taylor Model Basin Aerodynamics Laboratory	I-10
8	General Arrangement, Rotor/Wing Wind Tunnel Model	I-17
9	Assembly and Installation - ONR Rotor/Wing Wind Tunnel Model - Inboard Profile - Series II	I-18
10	Assembly and Installation - ONR Rotor/Wing Wind Tunnel Model - Plan View - Series II	I-19
11	Revised Assembly and Installation - ONR Rotor/Wing Wind Tunnel Model - Inboard Profile - Series III.	I-20
12	Rotor/Wing Model Installation in Wind Tunnel	I-21
13	Schematic of Model Mounting System	I-22
14	Schematic Hydraulic Circuit Diagram	I-23
15	Control System Schematic	I-24
16	Hydraulic Power Supply.	I-25
17	Model Controls and Instrumentation.	I-26
18	Control Wiring Block Diagram	I-27
19	Instrumentation Wiring Block Diagram.	I-28
20	Conversion Control Programmer	I-29
21	Conversion Control Schematic	I-30
22	Rotor/Wing Model Vibration Mode Frequencies	I-33
23	Conversion Control Program	I-34
24	Rotor/Wing Wind Tunnel Tests - David Taylor Model Basin - Aerodynamics Laboratory - Hovering Thrust and Torque Coefficients.	I-54
25	Powered Rotor Aerodynamic Characteristics, $A_2 = 0^\circ$	I-55

Figure		Page
26	Powered Rotor Aerodynamic Characteristics, $A_2 = 5^\circ$	I-56
27	Ratio of Power Required by Rotor/Wing Model to Power Required by NACA Theory	I-57
28	Ratio of Power Required by Rotor/Wing Model to Power Required by Conventional Helicopter	I-58
29	Blade Root and Shaft Alternating Bending Moments	I-59
30	Roll Control in Helicopter Flight	I-60
31	Pitch Control in Helicopter Flight	I-61
32	Autorotating Rotor Characteristics	I-62
33	Blade Root and Shaft Alternating Bending Moments in Autorotation	I-63
34	Control Characteristics During Pseudoconversion Test	I-64
35	Control Characteristics and Lift and Moment Variations During Automatic Conversion - Run 82-P	I-65
36	Control Characteristics and Lift and Moment Variations During Automatic Conversion - Run 93-P	I-66
37	Rotor/Wing Rolling and Pitching Moments During Acceleration From RPM = 0	I-67
38	Lift, Rolling, and Pitching Moments Versus Azimuth Angle - Series I	I-68
39	Rotor/Wing Rolling and Pitching Moments - Zero Rotational Velocity - Series I	I-69
40	Blade Root and Shaft Alternating Bending Moments During Automatic Conversion	I-70
41	Oscillograph Records - Automatic Conversion, Acceleration, $A_2 = 0^\circ$	I-71
42	Oscillograph Records - Automatic Conversion, Deceleration, $A_2 = 0^\circ$	I-72
43	Oscillograph Records - Automatic Conversion, Acceleration, $A_2 = 5^\circ$	I-73
44	Oscillograph Records - Automatic Conversion, Deceleration, $A_2 = 5^\circ$	I-74
45	Stopped-Rotor Maximum Lift/Drag Ratio	I-75
46	Wing Span Efficiency Factor - Tail Off, Rotor Sealed to Fuselage	I-76
47	Rotor/Wing Stopped-Rotor Stall Pattern - Long-Nosed Fuselage	I-77
48	Rotor/Wing Stopped-Rotor Stall Pattern - Short-Nosed Fuselage	I-78
49	Rotor/Wing Stopped-Rotor Stall Pattern - Short-Nosed Fuselage - Forward Blade Off - Aft Blade Incidence = 0°	I-79
50	Rotor/Wing Stopped-Rotor Stall Pattern - Short-Nosed Fuselage - Forward Blade Off - Aft Blade Incidence = 5°	I-80

Figure		Page
51	Rotor/Wing Stopped-Rotor Stall Pattern - Short-Nosed Fuselage - All Blades Off	I-81
52	Rotor/Wing Stopped-Rotor Stall Pattern - Long-Nosed Fuselage - Wing Fences	I-82
53	Rotor/Wing Stopped-Rotor Stall Pattern - Short-Nosed Fuselage - Forward Blade Incidence = 90° - Aft Blade Incidence = -10°	I-83
54	Stopped-Rotor Aerodynamic Characteristics	I-84
55	Lift and Pitching Moment Characteristics	I-85
56	Lateral-Directional Stability Characteristics	I-86
57	Vertical Tail Sidewash Study	I-87
58	Dynamic Pressure Ratio at Tail	I-88
59	Downwash Angle at Tail	I-89
60	Roll Control Effectiveness	I-90
61	Hot Cycle Rotor/Wing VTOL ASW Aircraft	I-97
62	Full-Scale Rotor/Wing Performance	I-98
63	Ratio of Power Required by Rotor/Wing Model to Power Required by Modified NACA Theory	I-99
64	Estimated Maximum Trimmed Lift/Drag Ratio	I-100
65	Hovering Figure of Merit	I-101
66	Aircraft Rolling Amplitudes During Conversion	I-102

SUMMARY

This report describes the analysis, design, and wind tunnel evaluation of a wind tunnel model (Figure 1) representative of a Rotor/Wing VTOL aircraft, a new concept pioneered by Hughes Tool Company - Aircraft Division for a high-speed VTOL aircraft that has the hovering efficiency and low downwash velocity of a helicopter. The Rotor/Wing is a rigid rotor with a central hub fairing large enough to act as a wing and at the same time provide sufficient structural support for the rotor so that it may be stopped in flight. By stopping the rotor in flight, the speed limitations of the helicopter are eliminated. For hovering and low flight speeds the Rotor/Wing acts as a powered rotor; for cruise flight it is stopped and locked to the fuselage so the large hub may act as a fixed wing with conventional jets propelling the craft.

This model research program was conducted under sponsorship of the U. S. Navy, Office of Naval Research (ONR Contract Nonr-4588(00)), Reference 1), in cooperation with the Bureau of Naval Weapons. The major item of investigation was the conversion between helicopter and stopped-rotor flight to demonstrate that the Rotor/Wing could be stopped and started in flight. Additional items evaluated were the overall aerodynamic characteristics of the complete model in both the running-rotor and stopped-rotor flight modes.

The tests were conducted in the 8- by 10-foot subsonic wind tunnel at the David Taylor Model Basin Aerodynamics Laboratory. They showed that:

a. Conversion in flight from the running- to stopped-rotor mode and back again is a simple and straightforward procedure that a pilot should be able to carry out manually without resorting to automatic programming devices.

b. Powered-rotor helicopter flight is similar to that of a conventional helicopter with the exception that there is a penalty of approximately 25 percent in power required for a given rotor lift. This results from the short blades and download on the large hub.

c. Autogyro flight is feasible, and contributes an important safety aspect in that autorotation may be entered following a complete powerplant failure using only aerodynamic forces to accelerate the rotor so that gentle emergency landings may be made.

d. Stopped-rotor aerodynamic characteristics are similar to those of a low aspect ratio airplane with respect to performance, stability, and control. Maximum L/D ratios in the range of 9 to 10 were measured for the model; going to full scale, maximum L/D's greater than 10 are anticipated for the basic Rotor/Wing configuration tested. For disc-to-hub area ratios greater than basic, the tests showed that full-scale aircraft may expect a maximum lift/drag ratio of 12 or more.

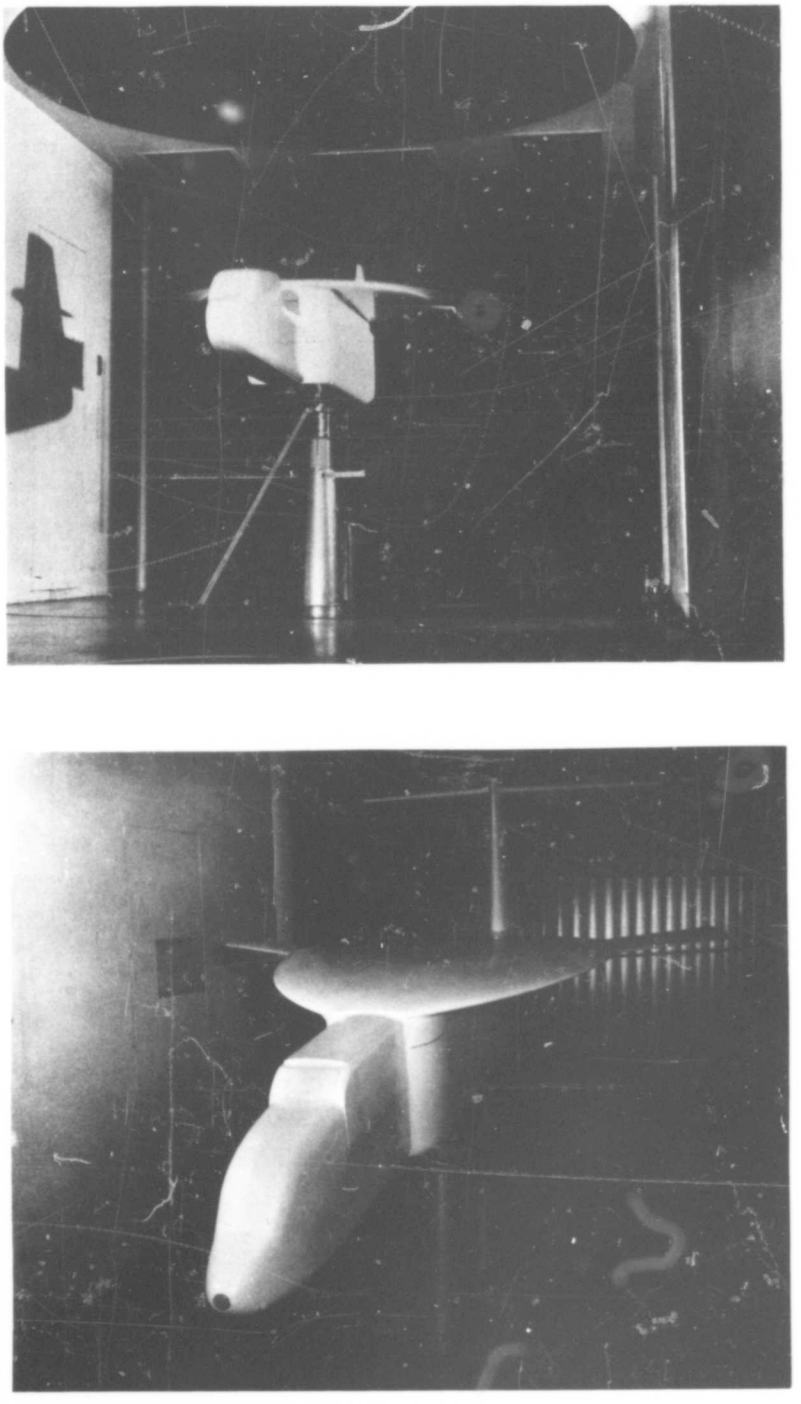

Figure 1. Rotor/Wing Wind Tunnel Model

INTRODUCTION

The Rotor/Wing concept, which was evolved in 1962, consists of a dual-purpose lifting device that is a tip-jet-powered rotor for low-speed flight and stops to become a fixed-wing for high-speed cruising flight. Figure 2 shows schematically the various modes in which the Rotor/Wing vehicle may fly. They may be described as follows:

a. Helicopter
   Where the rotor is powered and control is primarily from rotor cyclic and collective pitch

b. Autogyro
   Where the rotor autorotates and the engines function as conventional turbojets; control is primarily from cyclic pitch augmented by the tail

c. Airplane
   Where the rotor is stopped and locked to act as a fixed wing; the engines function as turbojets; control is from the tail surfaces.

The Hot Cycle propulsion system shown schematically in Figure 3 is an integral part of the Rotor/Wing concept. This system transmits power pneumatically from turbojet gas generators to rotor blade tip-jets or airplane-type thrust nozzles; it permits reductions in propulsion system weight and eliminates the need for a torque-reacting tail rotor.

To initiate an experimental research program for investigating the characteristics of the Rotor/Wing, Hughes sponsored a comprehensive whirlstand test program during the winter of 1962-63 using a series of Rotor/Wing models (see Figure 4). The hovering characteristics were determined for a number of combinations of hub and blade configurations. Three hubs were tested, all of equal plan-form area: one was circular (which should be best for hovering), one was triangular (which should be best for cruise flight with the rotor stopped), and the third was intermediate in shape between the circle and triangle (which should be a good compromise for both hovering and stopped-rotor flight). Four kinds of blade airfoil section, all with the same 15-percent blade thickness ratio and blade tip diameter, were tested: NACA 0015, elliptical, cambered elliptical, and circular arc with parabolic leading and trailing edges. The latter three were symmetrical fore and aft for operation in the stopped-rotor condition wherein one blade is in "reversed" flow, compared with the normal helicopter sense, and symmetry is thought necessary. These model tests showed that the intermediate "trisector" hub, in combination with the circular arc blades, was optimum, and that the penalty in hovering for this configuration was only about 20 percent in thrust, compared with a conventional rotor. This should be quite acceptable for a VTOL configuration with a maximum L/D greater than 10, the capability of 500-knot flight speeds, and overall superiority to the high-disc-loading VTOL concepts. Details of the hovering performance of this Rotor/Wing configuration are given in Appendix D.

Preliminary subsonic wind tunnel tests of the Rotor/Wing in the stopped-rotor mode were conducted at the David Taylor Model Basin Aerodynamics Laboratory under sponsorship of the U.S. Navy, Bureau of Naval Weapons, in the spring of 1964. The circular and triangular hub models, and blades of NACA 0015 and elliptical airfoil section were tested, as shown in Figure 5. These tests indicated satisfactory aerodynamic characteristics,

with Rotor/Wing alone lift/drag ratios as high as 12.5. Data from these tests are given in Appendix E.

In June 1964, Hughes entered into contract (ONR Contract Nonr-4588(00)) with the U.S. Navy, Office of Naval Research, in cooperation with the Bureau of Naval Weapons, to further investigate the Rotor/Wing principle through analysis and model testing. The work under this contract covered the design, analysis, construction, and testing of the model. A main item of investigation was the conversion process required to start and stop the rotor in flight. The model was designed to investigate fully this conversion flight regime to show its practicability, as well as to determine the overall aerodynamic characteristics of the aircraft in powered-rotor, autorotating-rotor, and stopped-rotor flight.

The research model, shown in Figures 6 and 7, was designed around existing model components available from the whirl test program insofar as possible; that is, trisector rotor hub fairing, circular arc blades, blade spars, blade tips, and blade pitch arms were used with minimum rework. Concurrently with the mechanical and structural design of the model, analyses were made of its vibration characteristics, flutter characteristics, and conversion procedures, to assure proper operation in the wind tunnel. Reference 2 describes the design and analysis phases of this research project.

The wind tunnel tests were conducted in two test series, during the spring of 1965. These were designated Series II and Series III (Series I was the Rotor/Wing-alone tests, in 1964). Series II tests were preliminary in nature; they checked out the operation of the model and provided basic data for all modes of flight, including conversion. Certain modifications were made to the model between the two test series, to improve its

characteristics. The Series III tests evaluated these modifications and gave positive, final proof of the feasibility of the conversion procedure.

For convenience in studying this report, a list of symbols and nomenclature may be found in Table 2, page I-51.

Volume I summarizes the findings of this research program and the appendixes, Volumes II and III, present greater details. Volume II includes analytical and test data; Volume III contains detail drawings of the model and the stress analysis.

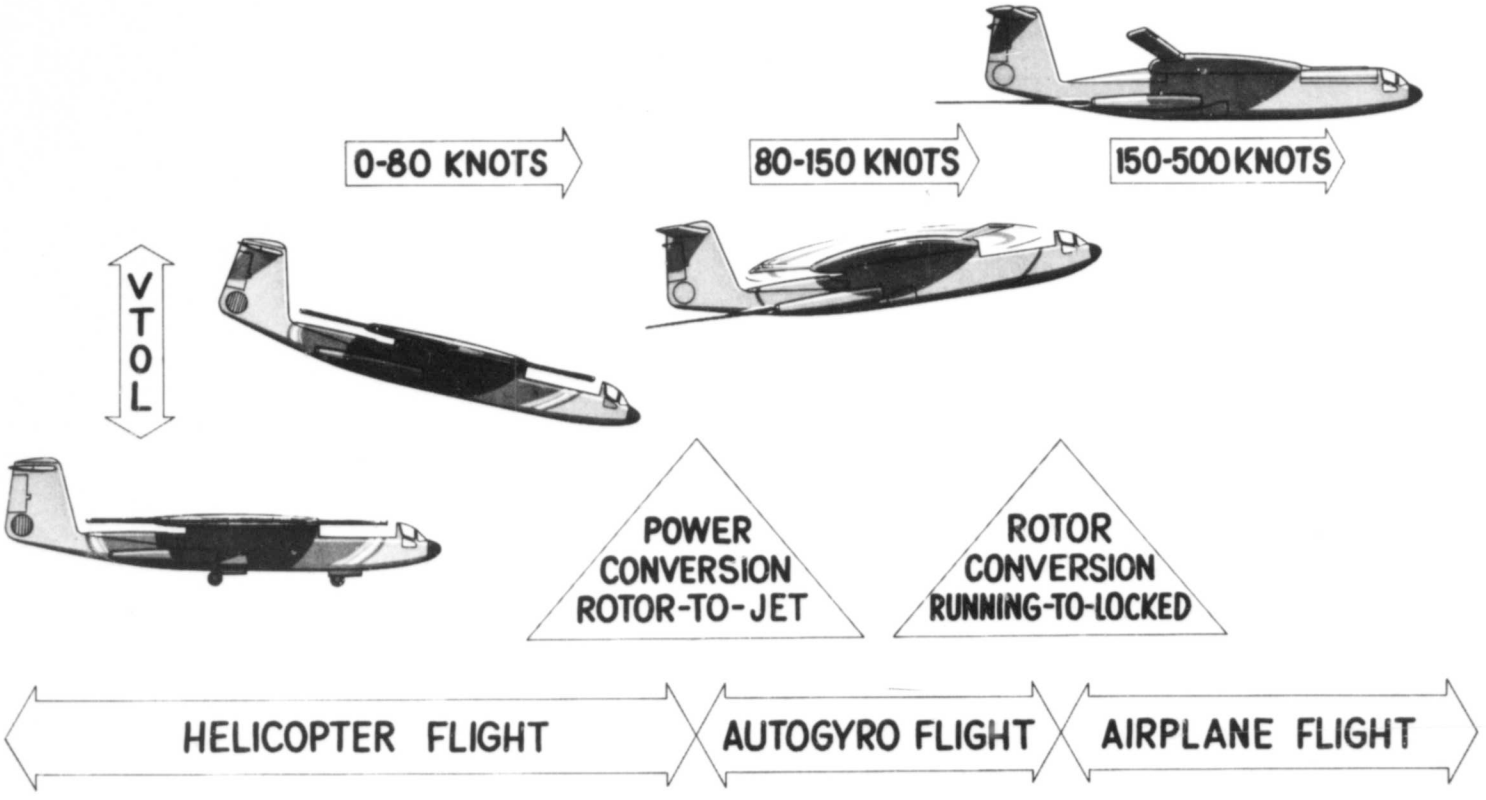

Figure 2. Rotor/Wing Flight Modes

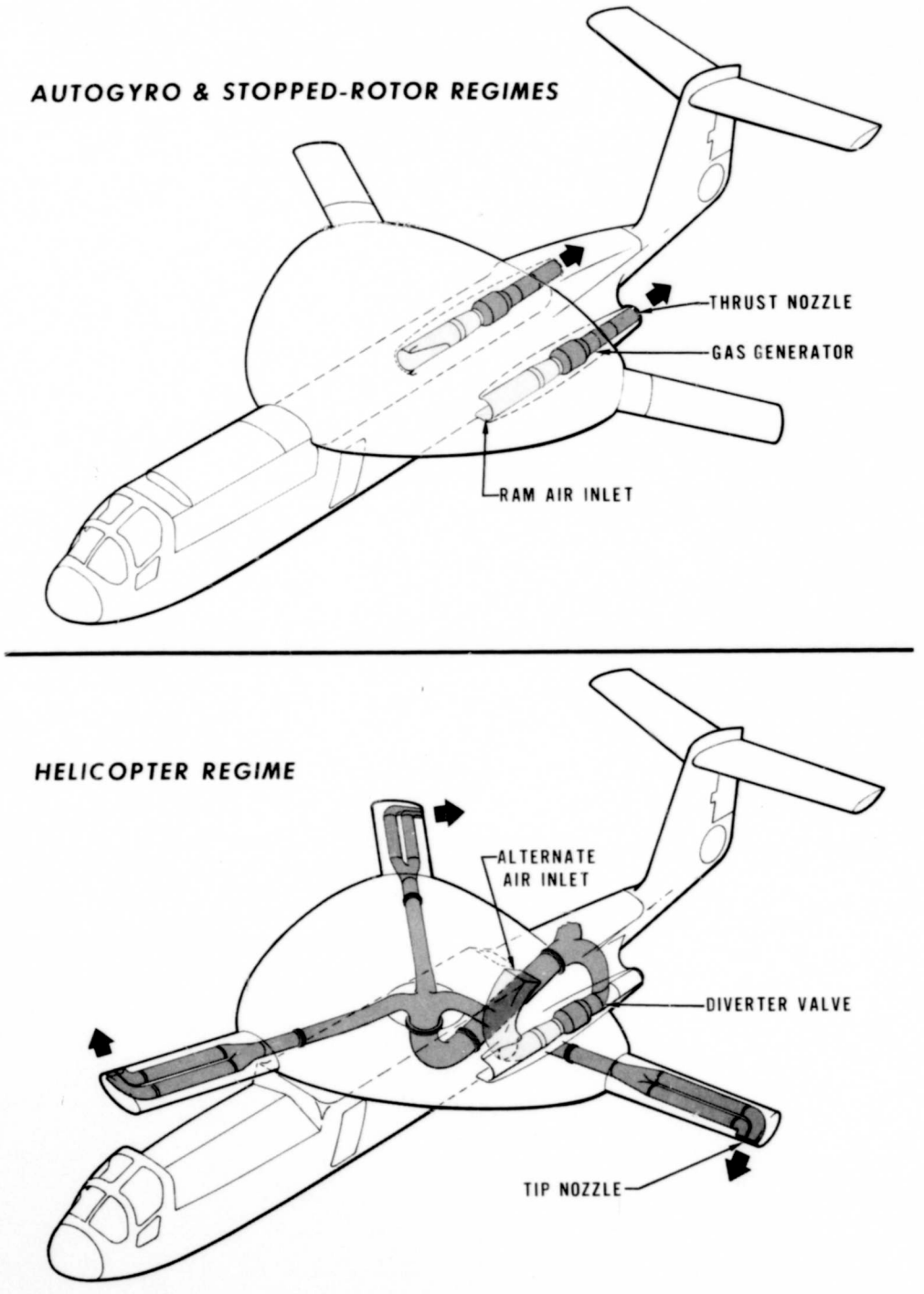

Figure 3. Propulsion System Schematic

Figure 4. Rotor/Wing Model Whirlstand - Hughes Tool Company, Aircraft Division

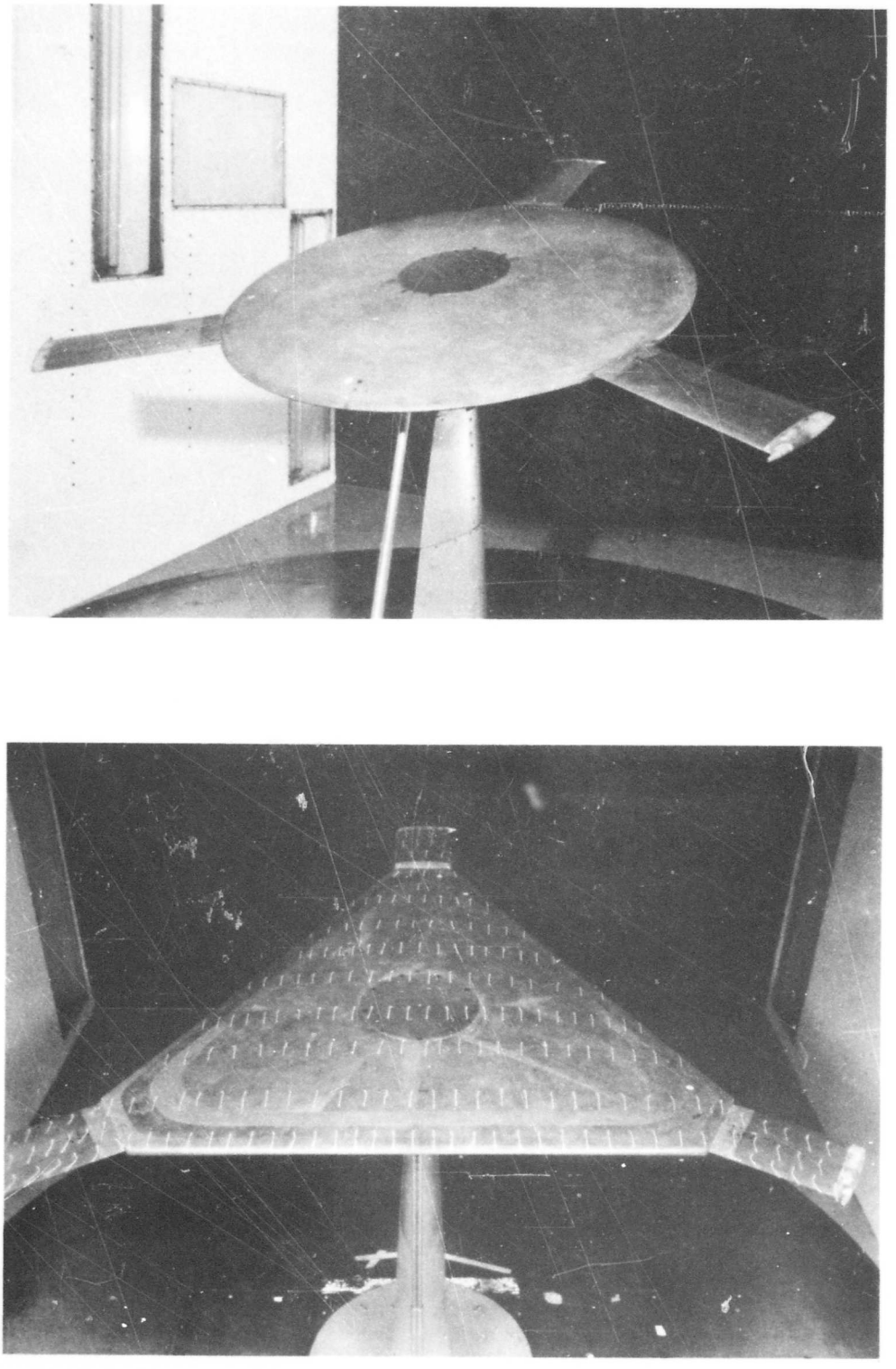

Figure 5. Rotor/Wing Wind Tunnel Model, Series I - David Taylor Model Basin Aerodynamics Laboratory

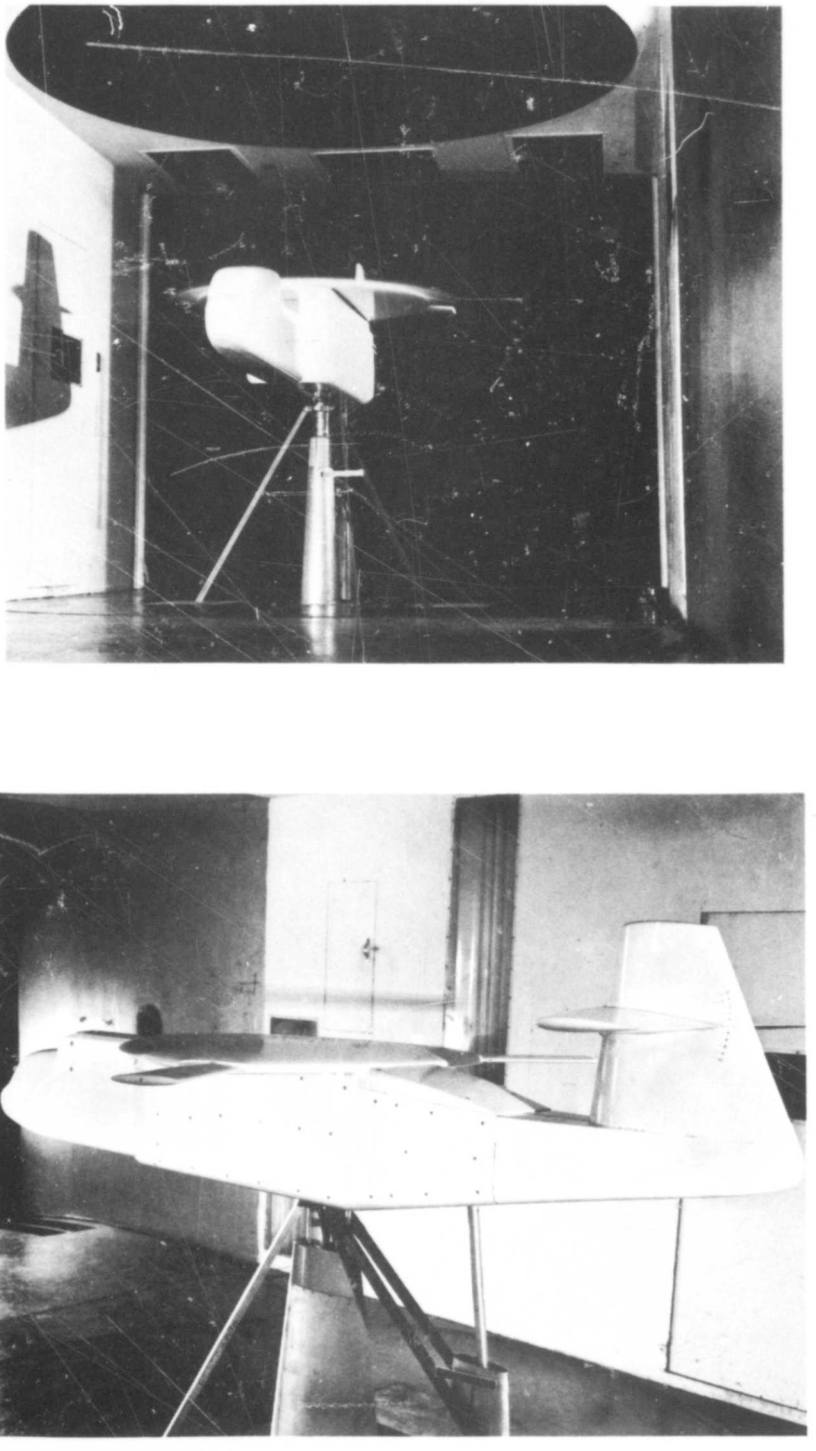

Figure 6. Rotor/Wing Wind Tunnel Model, Series II - David Taylor Model Basin Aerodynamics Laboratory

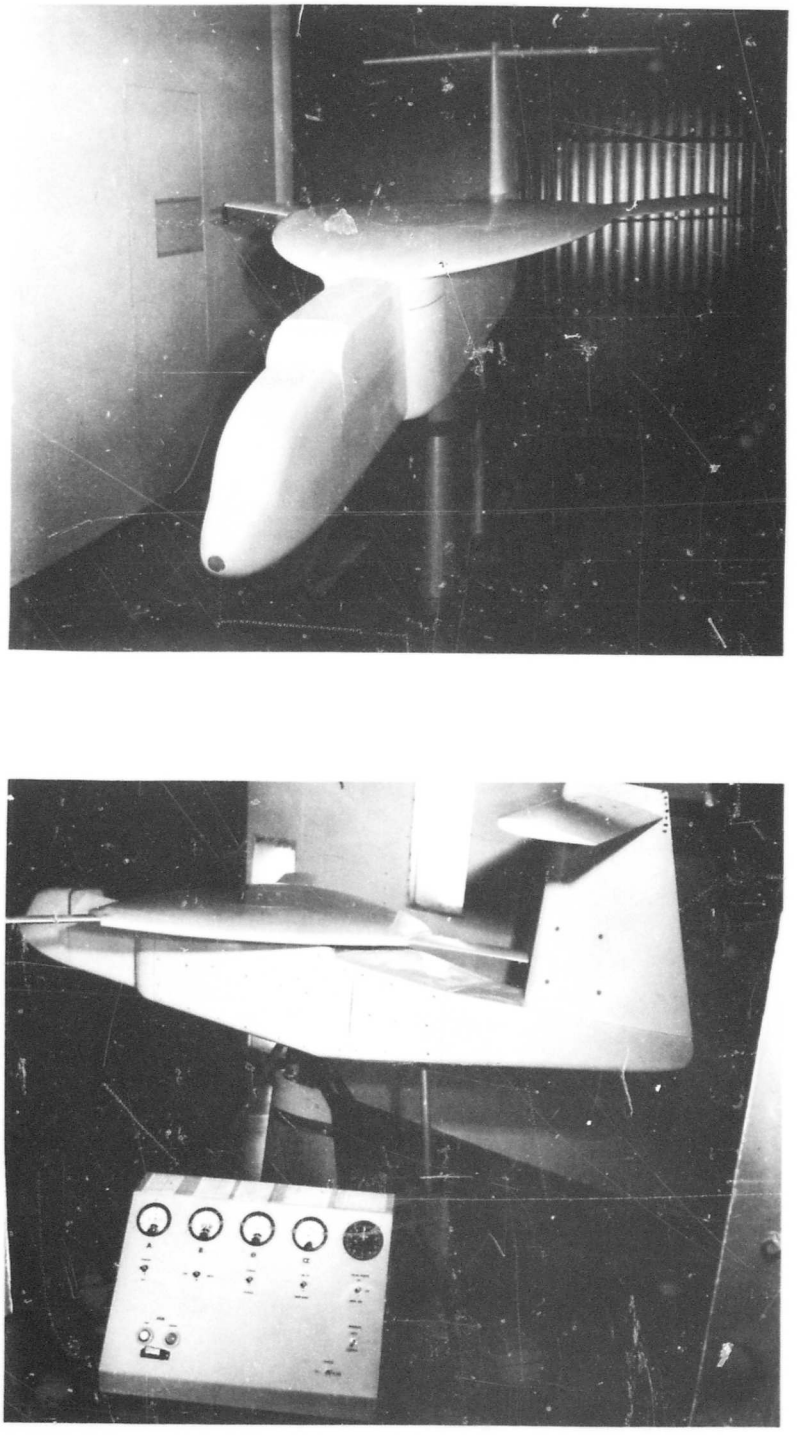

Figure 7. Rotor/Wing Wind Tunnel Model, Series III - David Taylor Model Basin Aerodynamics Laboratory

DESCRIPTION OF MODEL

In late 1962, HTC-AD designed and built a series of Rotor/Wing models and conducted whirlstand tests to evaluate their hovering performance (see Appendix D). The optimum model configuration from this test series was chosen as the Rotor/Wing for the ONR-BuWeps-sponsored wind tunnel model. It consisted of the trisector hub and extended blades of the modified circular arc airfoil section. This existing Rotor/Wing therefore determined the size of the wind tunnel model.

GENERAL ARRANGEMENT

The general arrangement of the Rotor/Wing model is shown in Figure 8. It consisted of a fuselage, tail, Rotor/Wing mounted atop the fuselage, and a series of nose blocks to simulate different forward fuselage arrangements. Figures 9, 10, and 11 are layouts of the internal mechanisms of the model; Figures 9 and 10 show the model in the configuration tested in Series II, and Figure 11 is an inboard profile of the Series III configuration. Detail drawings of the model may be found in Appendix G, and the structural analysis of the model is given in Appendix H.

The fuselage was basically a box built up of aluminum plate and covered with mahogany to provide the proper external contours. Inside the box structure were located the Rotor/Wing support bearings, hydraulic driving motor, cyclic and collective pitch mechanism, and instrumentation.

A tail support structure was mounted to the rear of the structural box. Either one of two nose configurations could be bolted to the front of the box. The pitch strut and the model support trunnion (which was also a hydraulic swivel for directing oil to and from the hydraulic motor) attached to the bottom of the box structure.

The vertical tail bolted to the top of the aft fuselage. The horizontal tail was mounted from the vertical tail by a mechanism that permitted manual setting of the horizontal tail incidence angle and of two fixed differential incidence angles for investigating horizontal tail effectiveness as a roll control.

The Rotor/Wing itself consisted of a mahogany hub fairing over an aluminum hub and mahogany blades mounted on steel spars. Both the hub fairing and blades were covered with fiberglass. There were spanwise lightening holes through the blades, and certain regions of the hub fairing between the blade spars were cut out and filled with plastic foam to reduce weight and inertia.

An electrically-actuated control system described under Systems permitted remote control of the collective and cyclic pitch angles of the rotor.

INSTALLATION

The complete Rotor/Wing model was designed for testing in the 8- by 10-foot subsonic wind tunnel at the David Taylor Model Basin Aerodynamics Laboratory, Washington, D. C. Figure 12 is an installation drawing of the model mounted on tandem support struts. A short length of the main strut was permanently built into the model and served the dual function of model support and hydraulic fluid supply line to and from

the hydraulic motor that drove the Rotor/Wing in the powered rotor mode. A hydraulic swivel was concentric with the model pitch-change axis. This short strut plugged into, and was pinned to, the wind tunnel's lower yaw strut. The wind tunnel's regular telescoping pitch strut was used to control the angle of attack of the model.

During all Rotor/Wing tests in which the rotor turned (powered or autorotating), additional braces were required to stiffen the model support strut. Without these, the natural frequency of the model on its support would have been too low for the test requirements. Figure 13 is a schematic sketch of these external braces.

Hydraulic fluid was supplied to the model through hoses arranged to minimize interference with proper operation of the balance system. Electrical control and instrumentation signals were delivered to the model through a wire bundle.

SYSTEMS

ROTOR DRIVE

The rotor was driven hydraulically by a Vickers Model MF40-3918-30Y-4 hydraulic motor mounted in the fuselage just forward of the rotor shaft and parallel with it. A roller chain drive connected the motor with the rotor shaft. Figure 14 is a schematic diagram of the hydraulic circuitry. The variable-displacement hydraulic pump could either supply power to the Rotor/Wing or absorb power from it. For autorotation tests, the drive chain was removed, to minimize mechanical and hydraulic restriction to free rotation.

ROTOR CONTROL

Cyclic and collective pitch control was accomplished through a swashplate system. The nonrotating portion of the swashplate was positioned through a mixing linkage by linear electric actuators - one each for collective pitch, lateral cyclic pitch, and longitudinal cyclic pitch. From the rotating portion of the swashplate, vertical pitch links reached to pitch arms on the inboard end of the blade spars. Driver links kept the upper swashplate rotating with the rotor, and the lower swashplate indexed with the fuselage. Each blade spar was mounted at its inboard end in a tapered roller bearing that resisted the centrifugal force of the blade and permitted feathering; sleeve bearings at the outer edge of the hub supported the spars. Figure 15 is a schematic of the control system.

For the Series II tests, the swashplate was an ordinary helicopter swashplate; but for Series III tests, it was changed to a cam-type swashplate that could supply a fixed amount of twice-per-revolution cyclic pitch change in addition to the collective pitch and once-per-revolution cyclic pitch.

INSTRUMENTATION

Instrumentation for this model was of three types: one that gave a visual presentation of data to the operator, one that permitted recording the data, and one that supplied information to an automatic programming device for making conversions between stopped and running rotor conditions.

A small control panel was provided for instruments, showing:

Rotor speed
Collective pitch angle

Lateral cyclic pitch angle

Longitudinal cyclic pitch angle

Fuselage angle of attack

Rotor lock on-off

Switches on the panel permitted controlling all of these functions except rotor speed and fuselage angle of attack. Rotor speed was controlled through the hydraulic power supply unit (Figure 16); angle of attack by the tunnel operator.

A direct-reading oscillograph was provided for permanently recording data. These included the above items plus:

Rotor azimuth position

Rotor shaft bending moment about two mutually perpendicular axes

Blade spar flapwise bending moment at inboard end of blade (1 blade)*

Blade spar chordwise bending moment at inboard end of blade (1 blade)*

Fuselage accelerations in the longitudinal and lateral directions

Wind tunnel balance scale readings**

The control panel may be seen in Figure 17, while the wiring diagram for the controls is shown in Figure 18 and the wiring diagram for the instrumentation is given in Figure 19.

* All three blades were instrumented, but data were taken from only one at a time.

**Only during conversion tests in Series III.

CONVERSION CONTROL

A conversion control unit was built to control the rotor collective pitch, cyclic pitch, and fuselage angle of attack as a function of rotor speed, to make the rotor start or stop as desired. Figure 20 is a photograph of this device and Figure 21 shows its schematic arrangement. It was designed to plug into the model control circuits through the operator's control panel. The control functions built into this programmer were based on the conversion analysis discussed under Conversion Characteristics and on experimental data from the Series II and Series III wind tunnel tests.

ROTOR/WING

Diameter	85.90 in.
Disc area	40.30 sq ft
Solidity ratio	0.149
Wing area	19.87 sq ft (hub + 2 blades), 14.68 sq ft (hub + 3 blades)
Aspect ratio	2.98 (hub + 2 blades). 2.82 (hub + 3 blades)
Collective pitch	-10 to +20 deg
Cyclic pitch	
Lateral	±15 deg
Longitudinal	±15 deg
Blade chord	6.66 in.
Blade thickness ratio	15 percent
Blade airfoil section	Modified circular arc

HORIZONTAL TAIL	SERIES II	SERIES III
Span	39.40 in.	54.00 in.
Area	3.61 sq ft	4.17 sq ft
Root chord (theoretical)	16.50 in.	12.00 in.
Aspect ratio	3.00	4.50
Taper ratio	0.60	0.83
Leading edge sweepback	25 deg	20 deg
Tail length (to ℄ rotor)	50.00 in.	52.41 in.
Airfoil section		
Root	NACA 0015	NACA 0015
Tip	NACA 0012	NACA 0012

VERTICAL TAIL

Span	19.60 in.	25.00 in.
Area	2.10 sq ft	2.88 sq ft
Root chord	21.20 in.	21.20 in.
Aspect ratio	1.27	1.50
Taper ratio	0.46	0.57
Leading edge sweepback	6 deg	5 deg
Tail length (to ℄ rotor)	50.30 in.	50.57 in.
Airfoil section		
Root	NACA 0019	NACA 0019
Tip	NACA 0009	NACA 0012

FUSELAGE

1. Tandem cockpit forward of blade tip, leading blade faired into fuselage
2. Tandem cockpit forward of blade tip, fuselage fairings open for blade clearance
3. Tandem cockpit beneath blade, leading blade not faired into fuselage

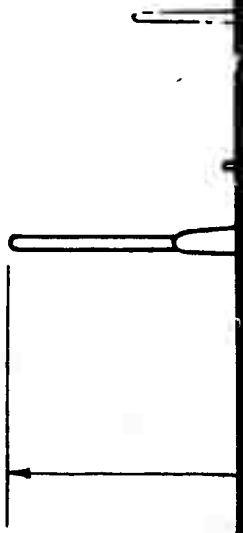

ides)
ides)

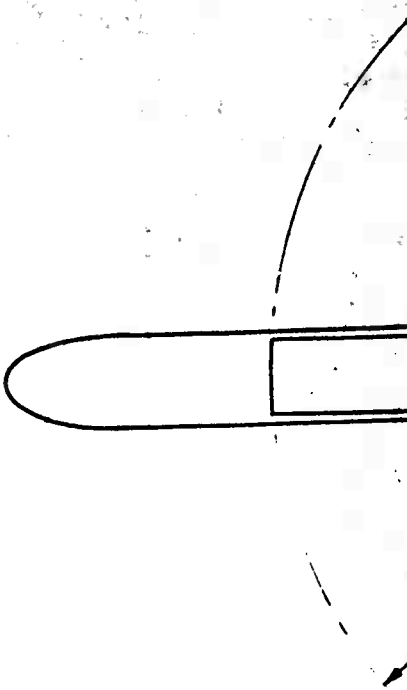

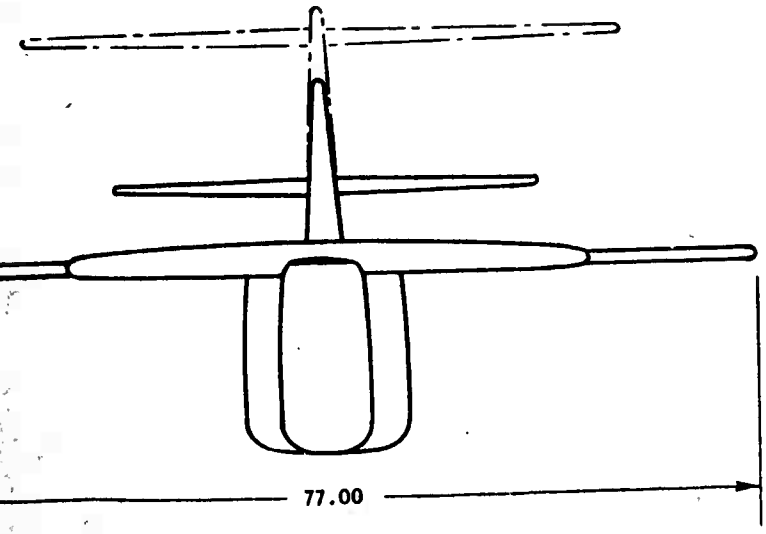

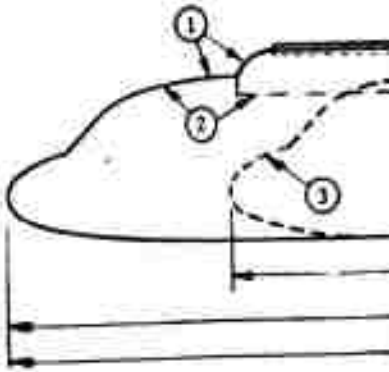

2

1

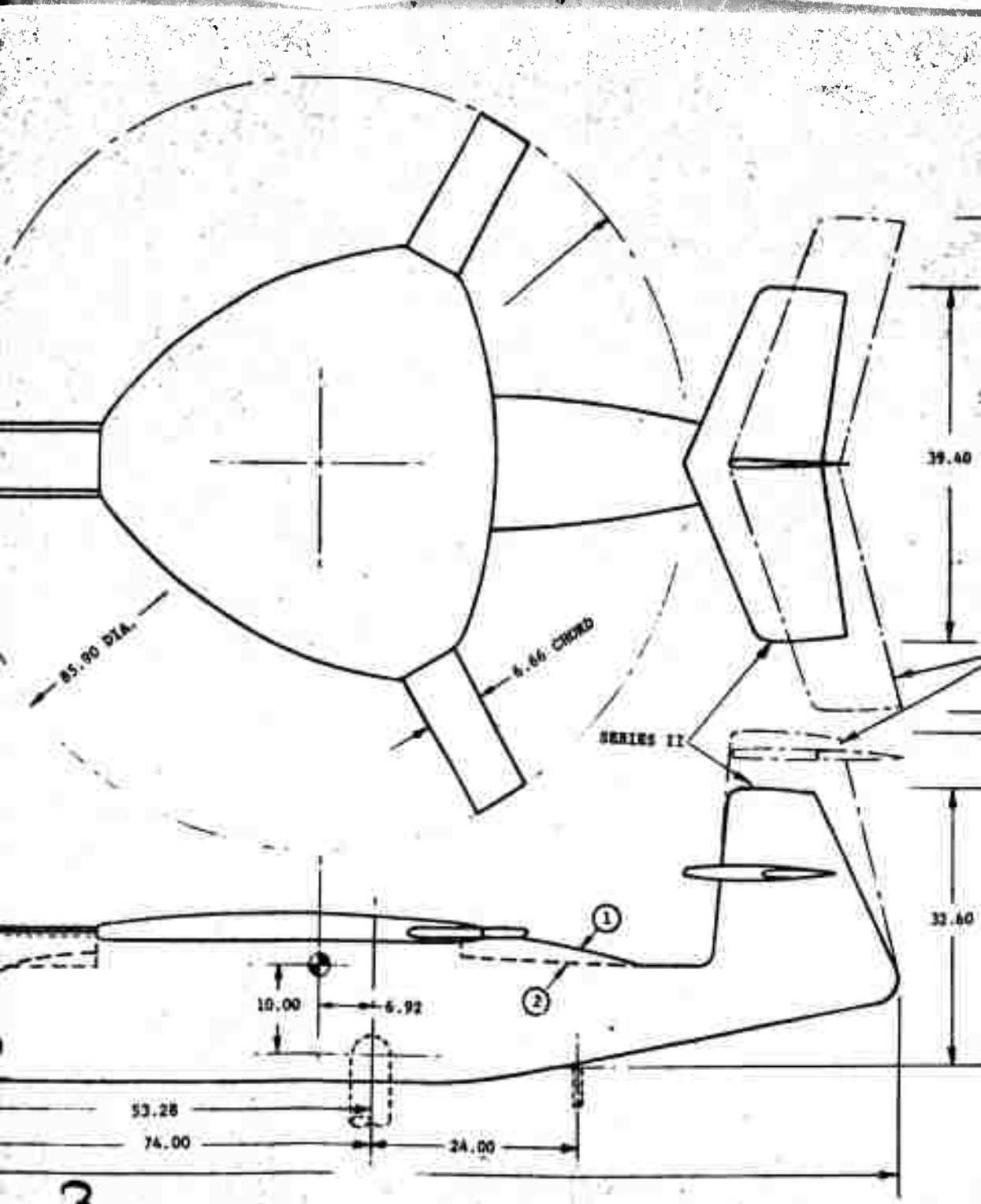

Figure 8. General Arrangement, Rotor/Wing Wind Tunnel Model

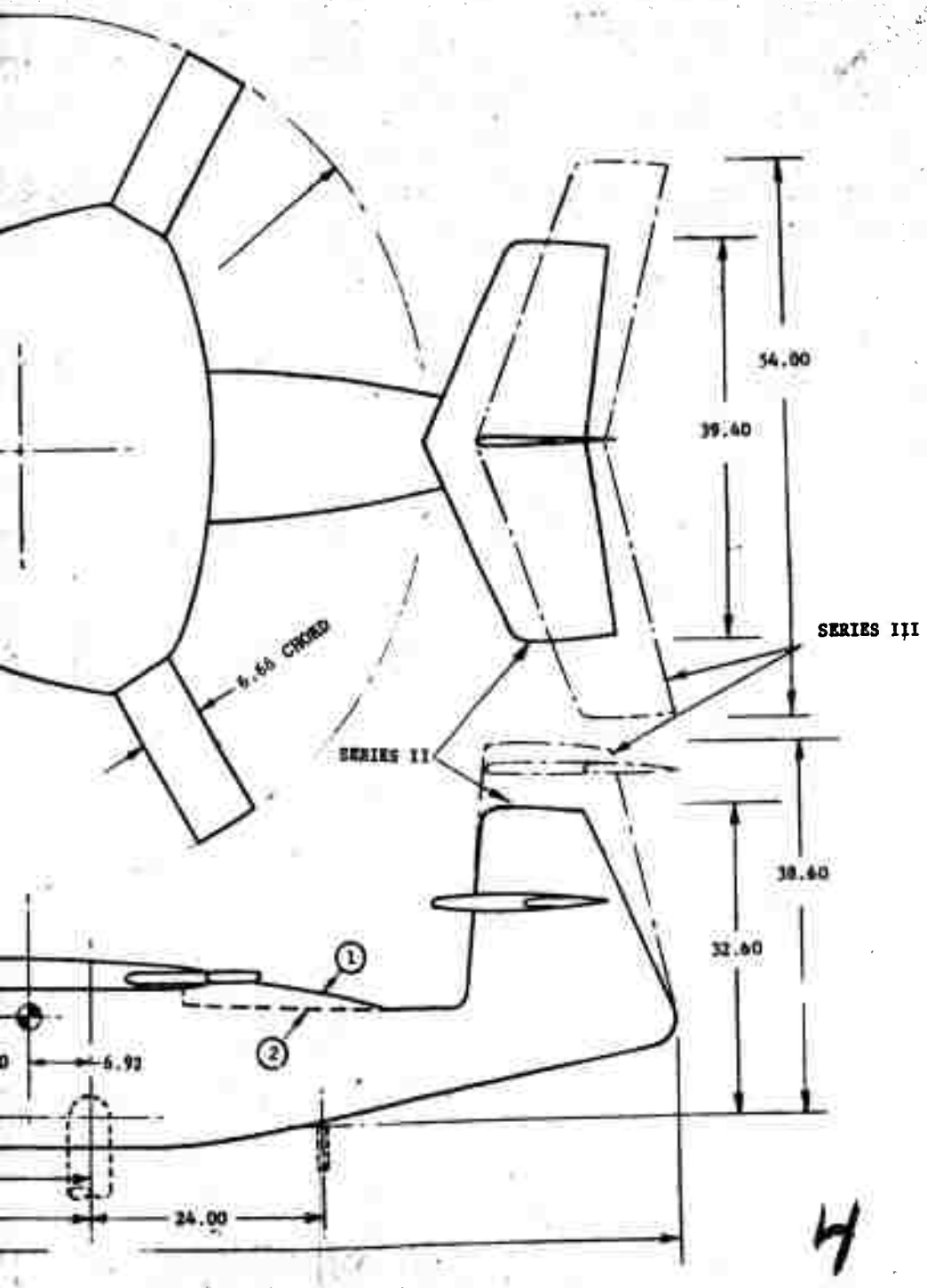

Figure 8. General Arrangement, Rotor/Wing Wind Tunnel Model

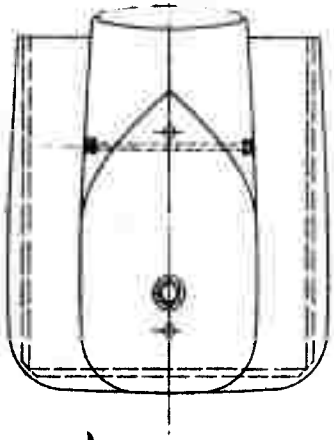

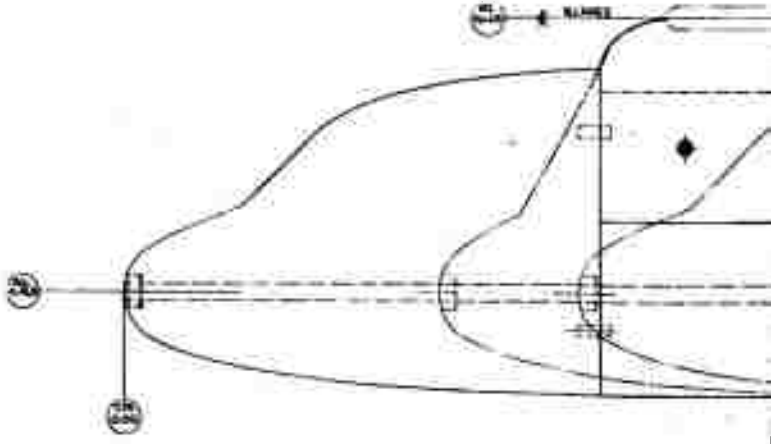

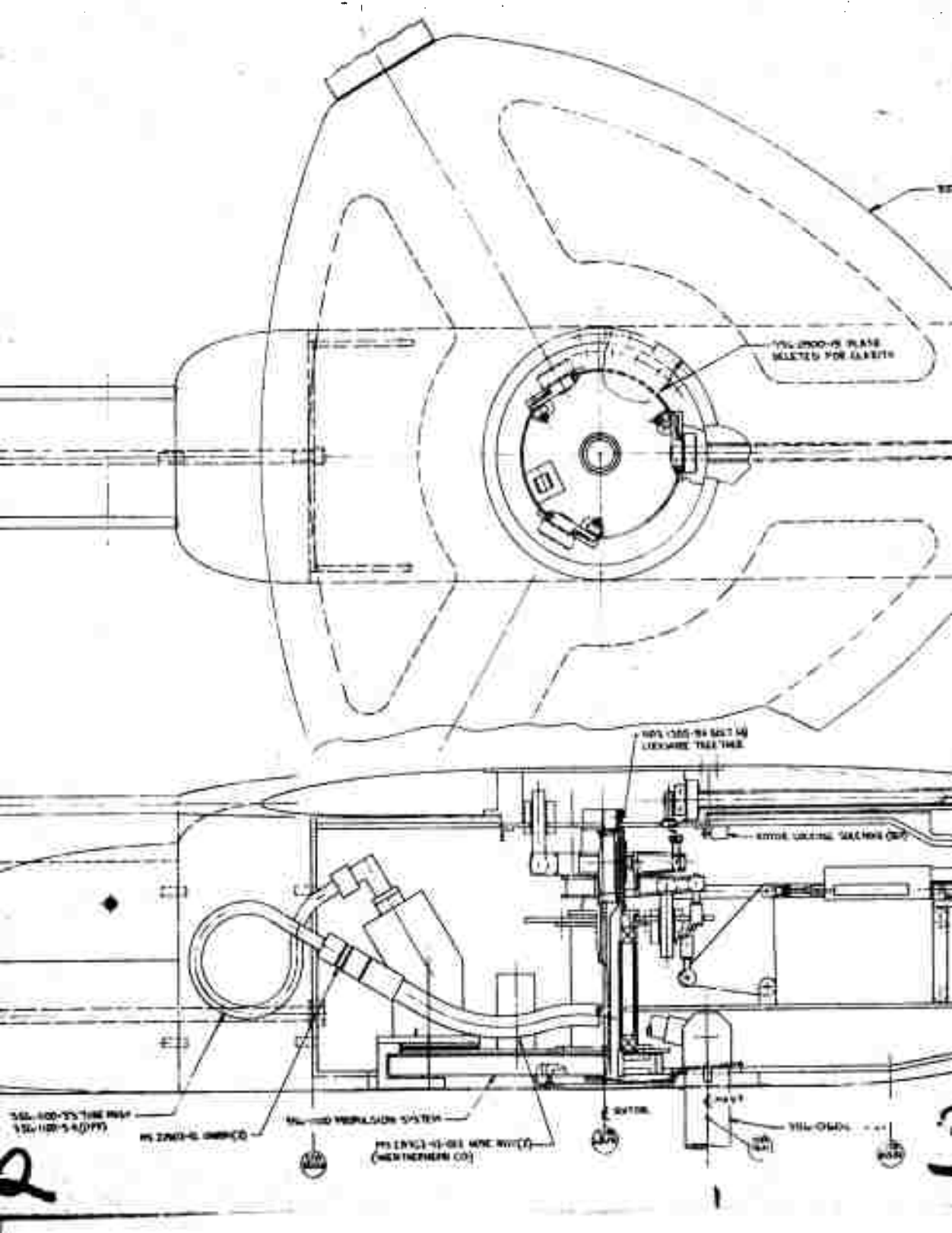

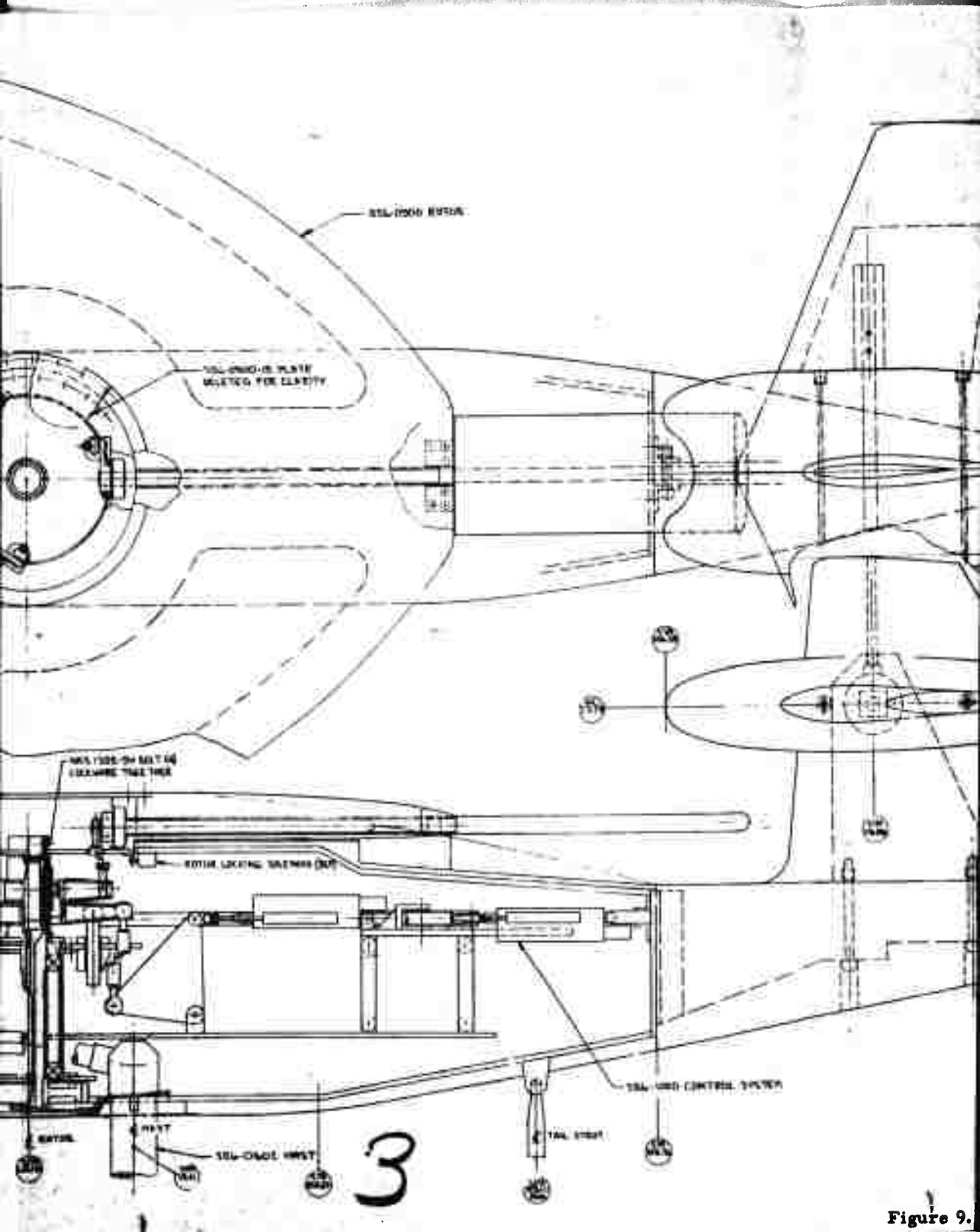

Figure 9.

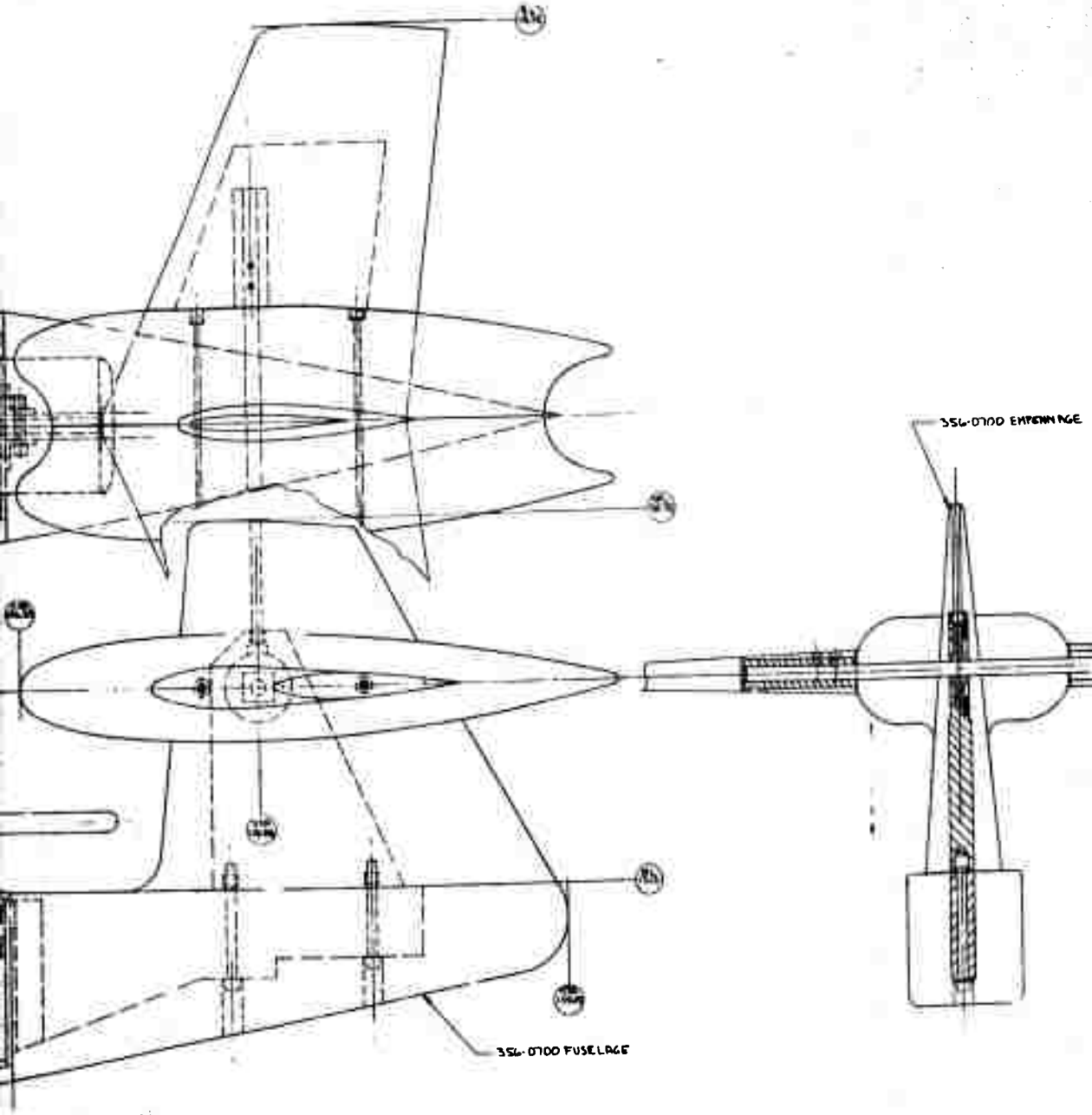

4

Figure 9. Assembly and Installation - ONR Rotor/Wing Wind Tunnel Model - I

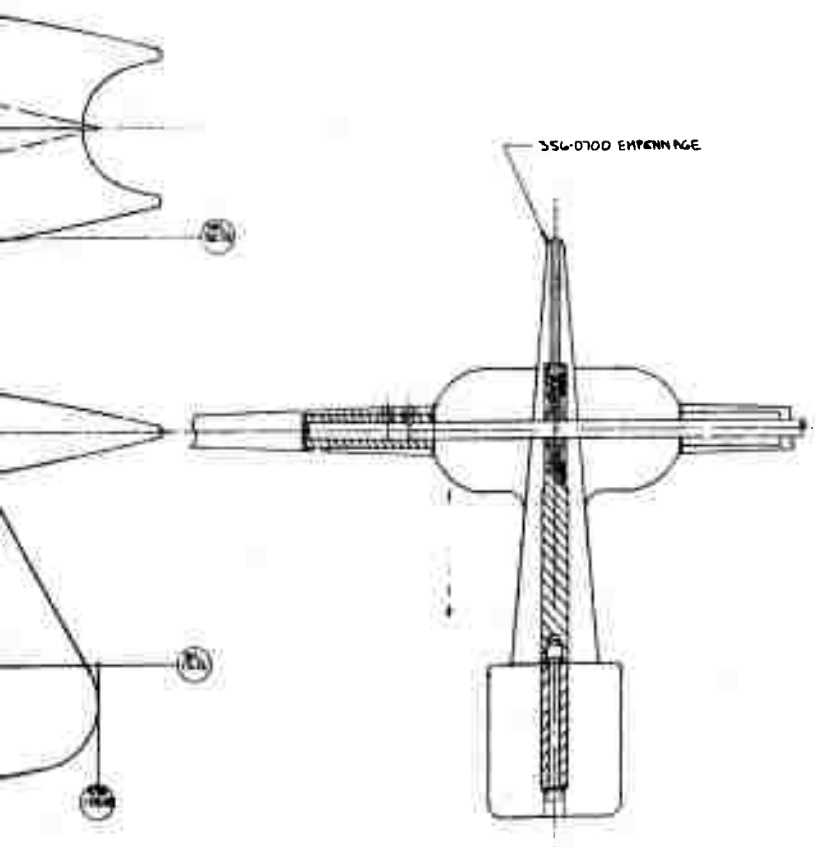

356-0600

5

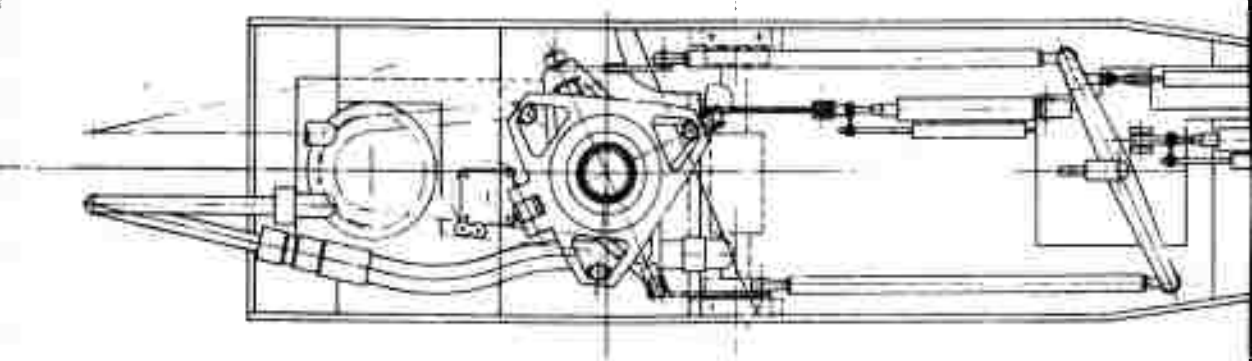

Figure 10. Assemb

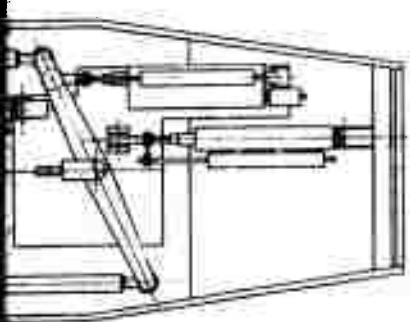

2

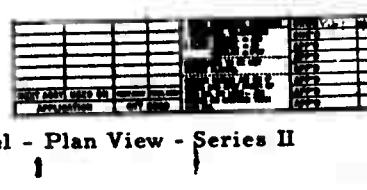

Figure 10. Assembly and Installation - ONR Rotor/Wing Wind Tunnel Model - Plan View - Series II

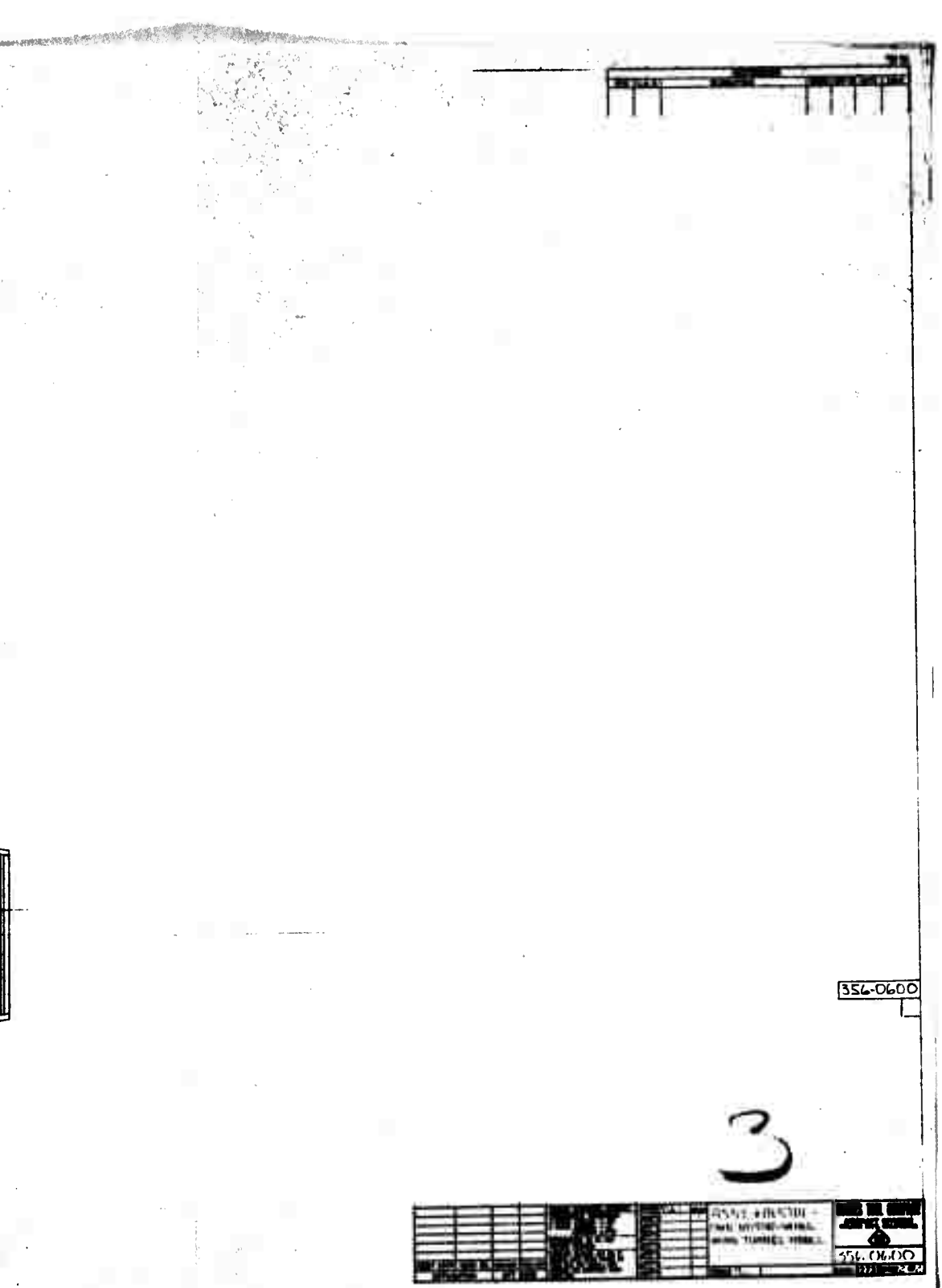

ation - ONR Rotor/Wing Wind Tunnel Model - Plan View - Series II

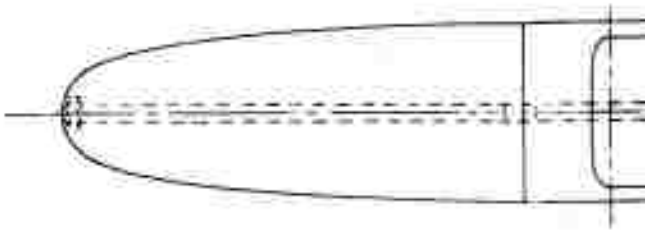

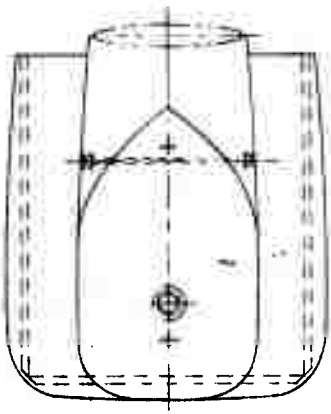

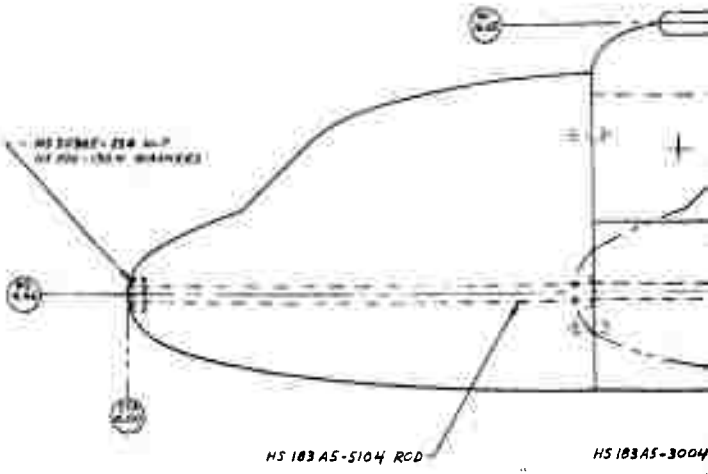
HS 183 AS-5104 RCD
HS 183 AS-3004

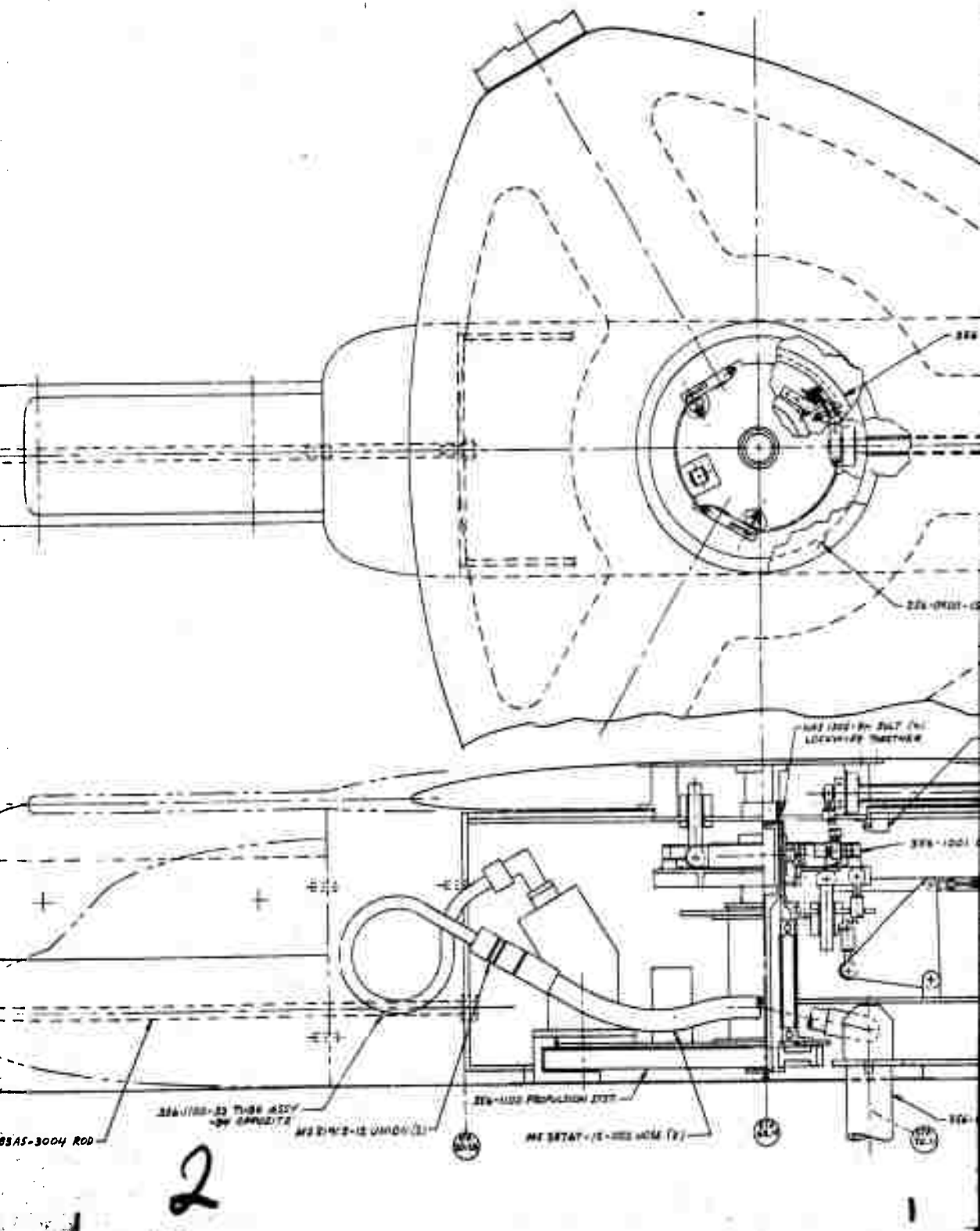
BSAS-3004 ROD
2
1

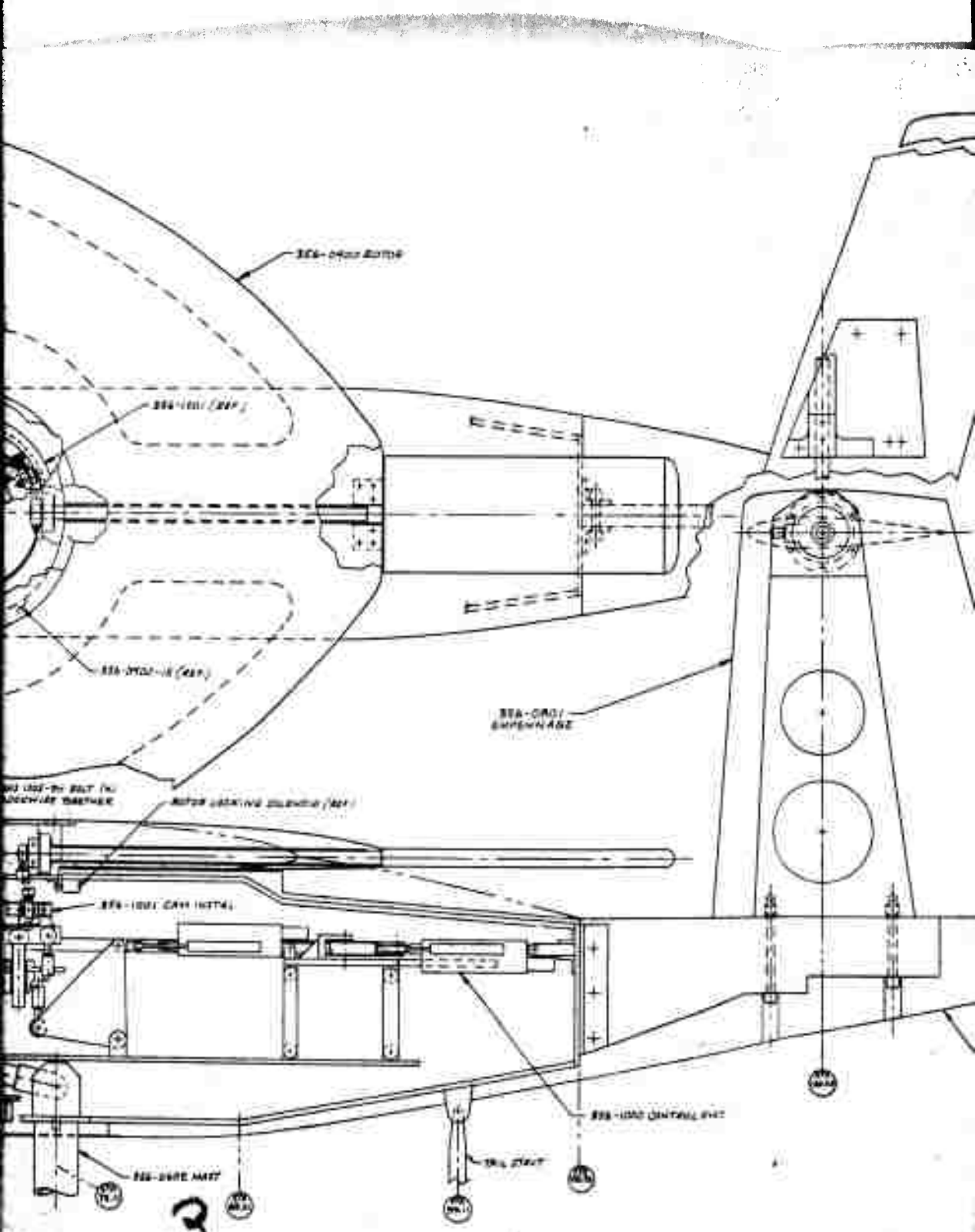

Figure 11. Revised A

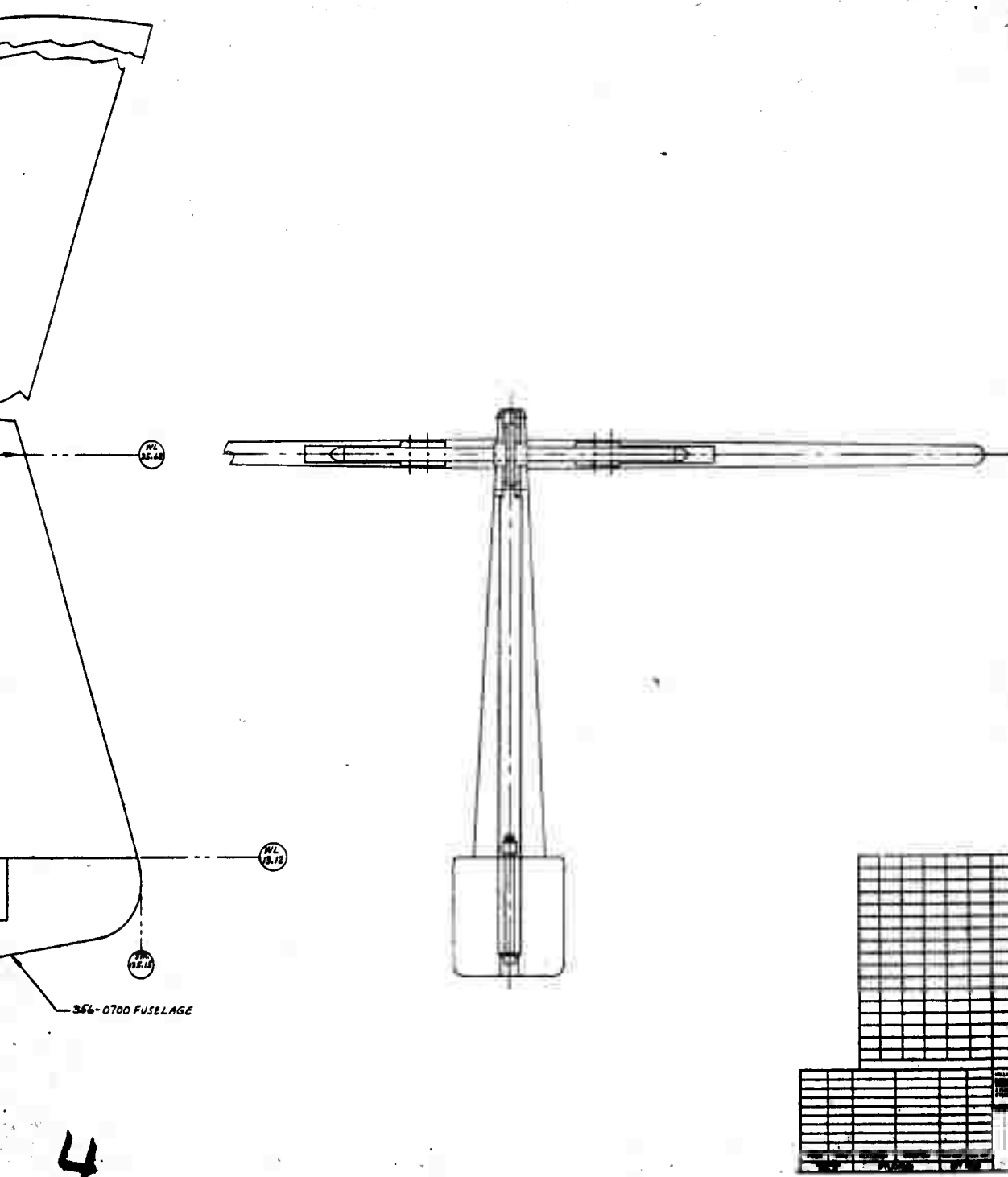

4

ed Assembly and Installation - ONR Rotor/Wing Wind Tunnel Model - Inboard Profile - Series III

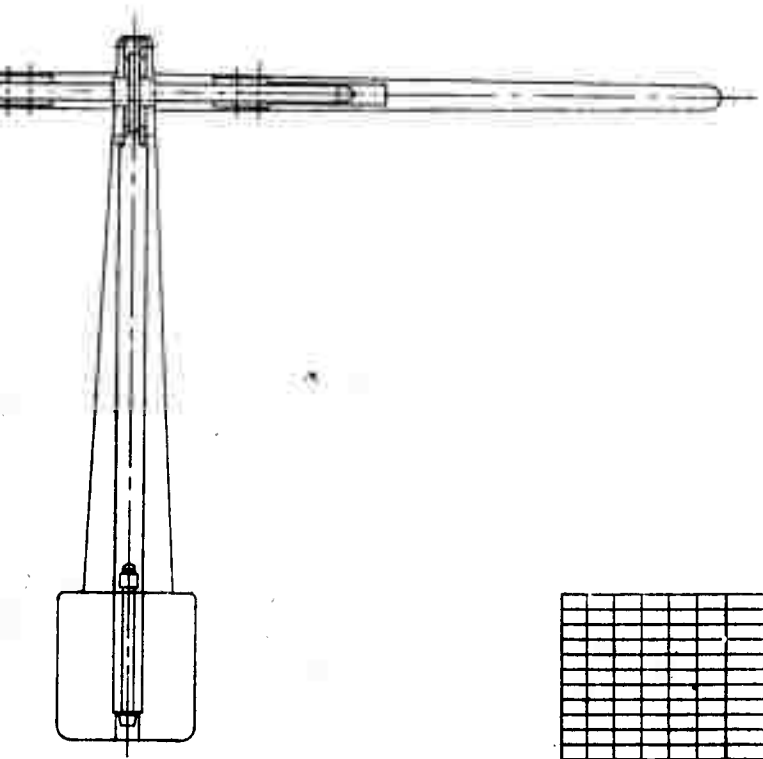

5

356-0606

REVISED ASSY & INSTAL-
ONR ROTOR/WING
WIND TUNNEL MODEL

02731 356-0606

/Wing Wind Tunnel Model - Inboard Profile - Series III

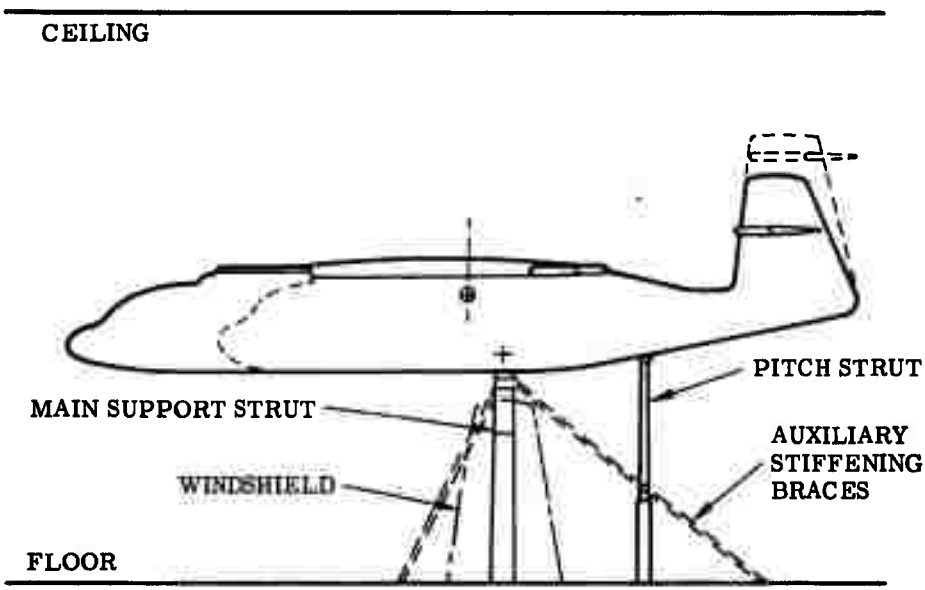

Figure 12. Rotor/Wing Model Installation in Wind Tunnel

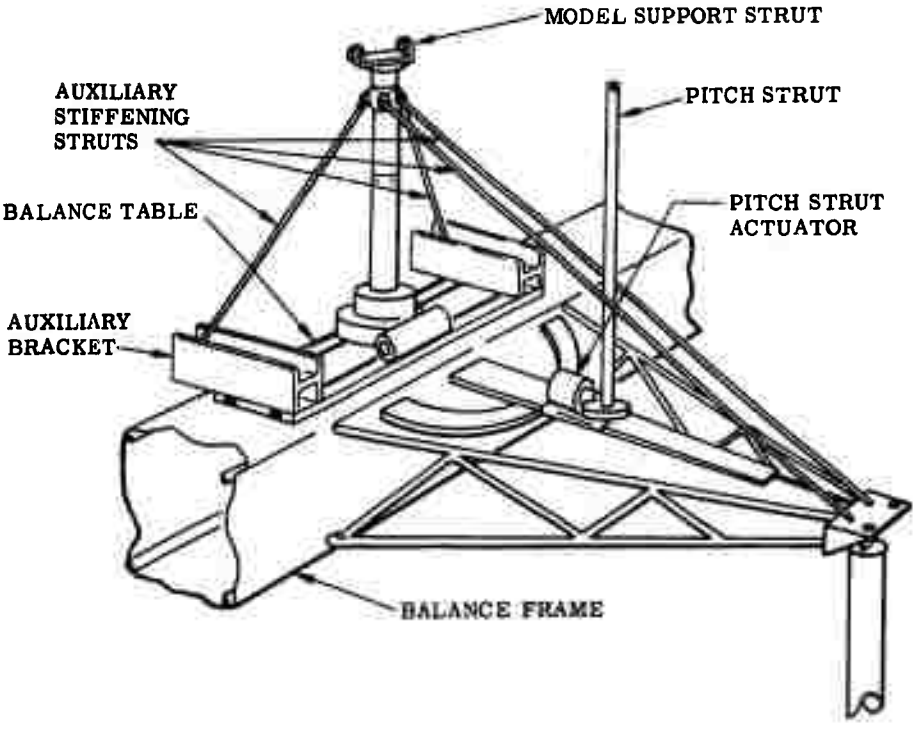

Figure 13. Schematic of Model Mounting System

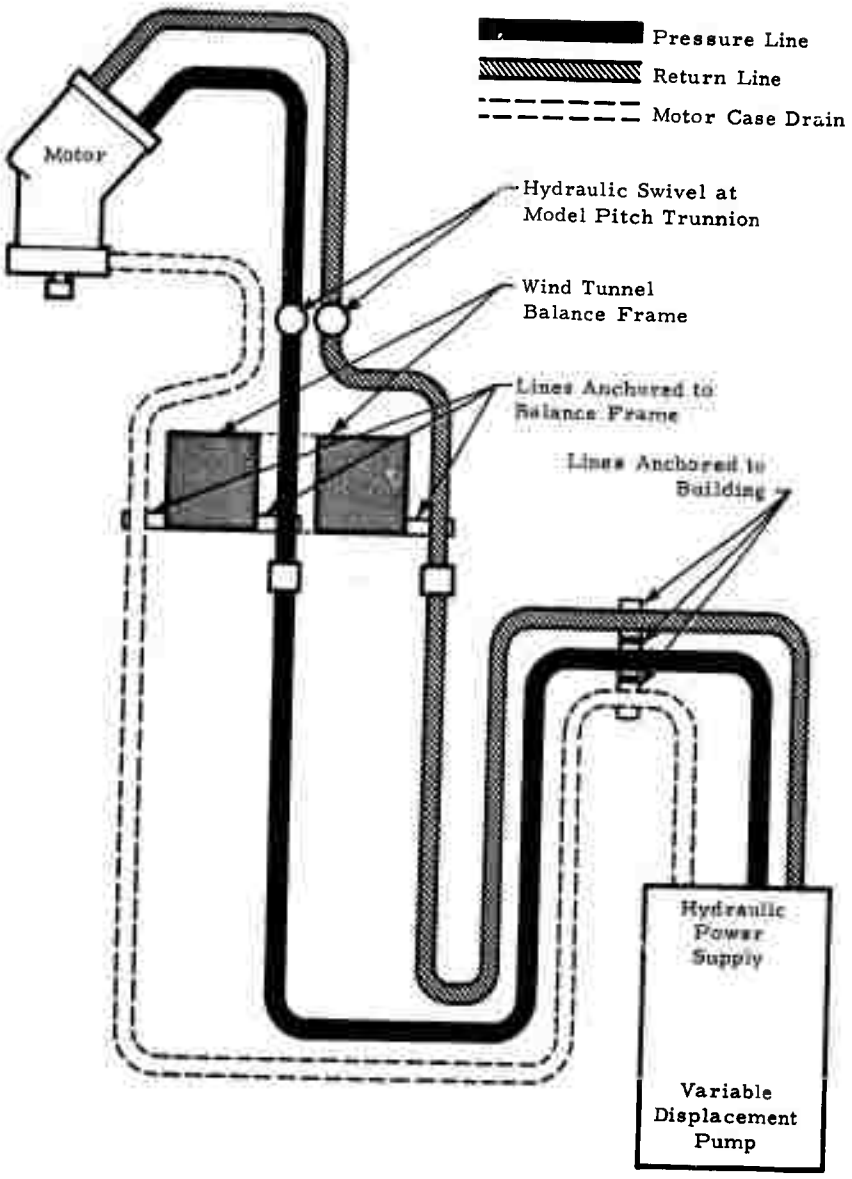

Figure 14. Schematic Hydraulic Circuit Diagram

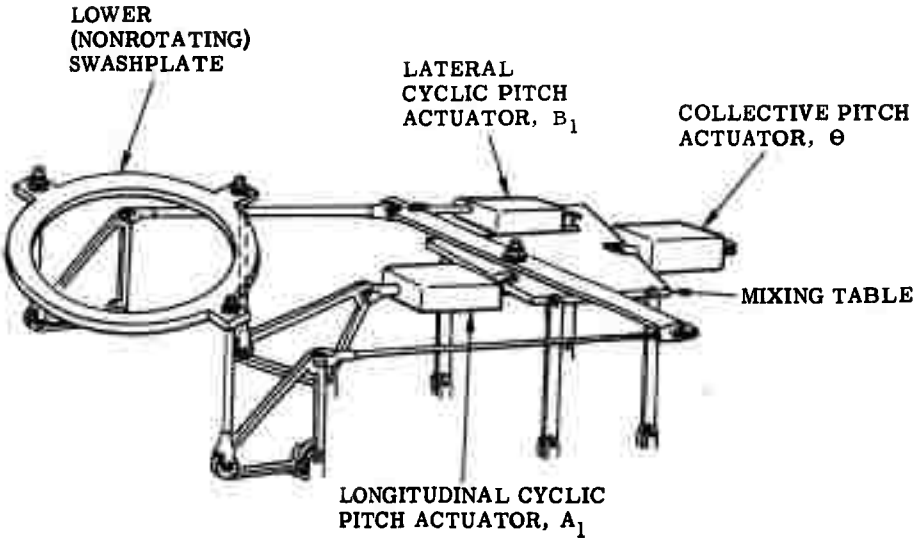

Figure 15. Control System Schematic

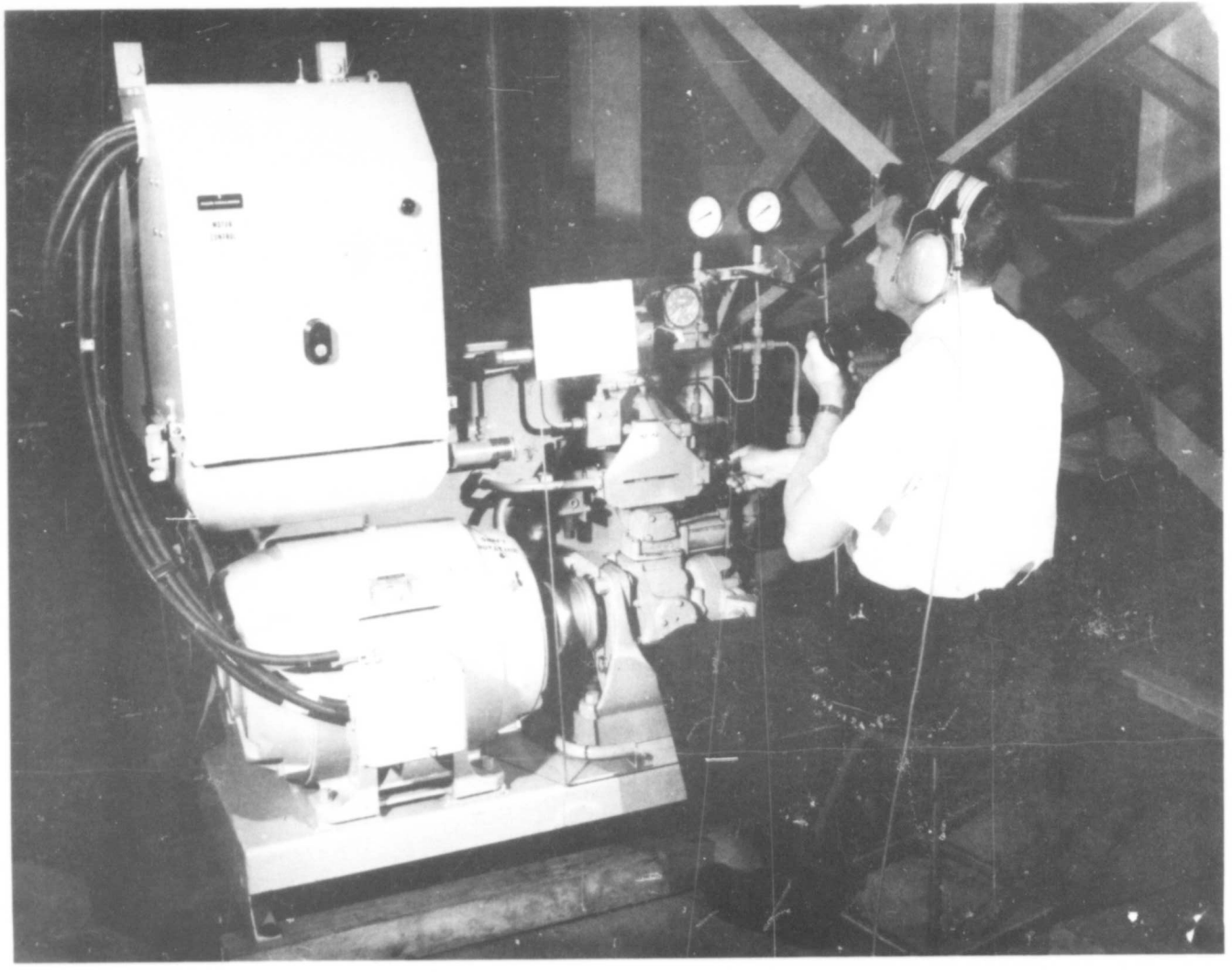

Figure 16. Hydraulic Power Supply

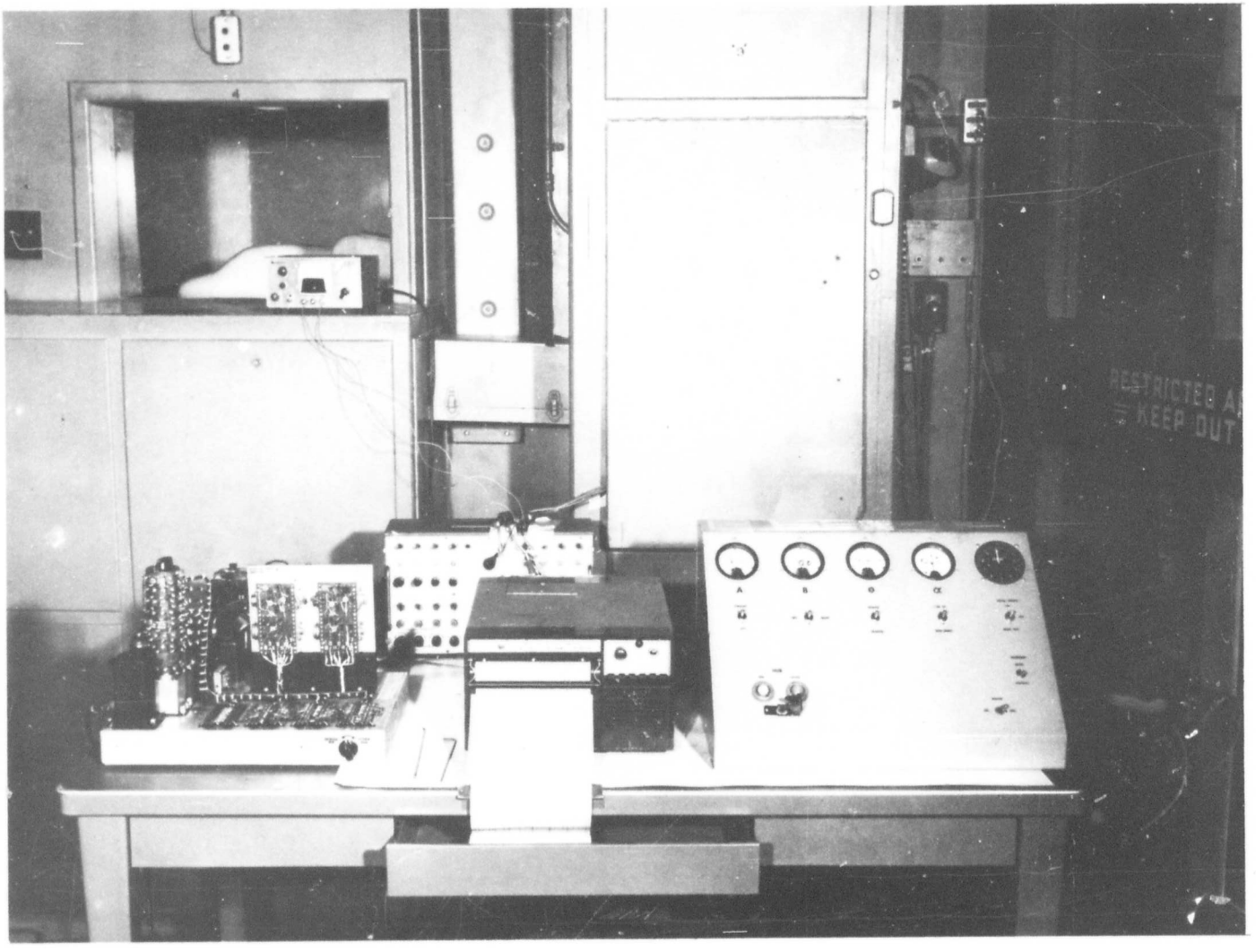

Figure 17. Model Controls and Instrumentation

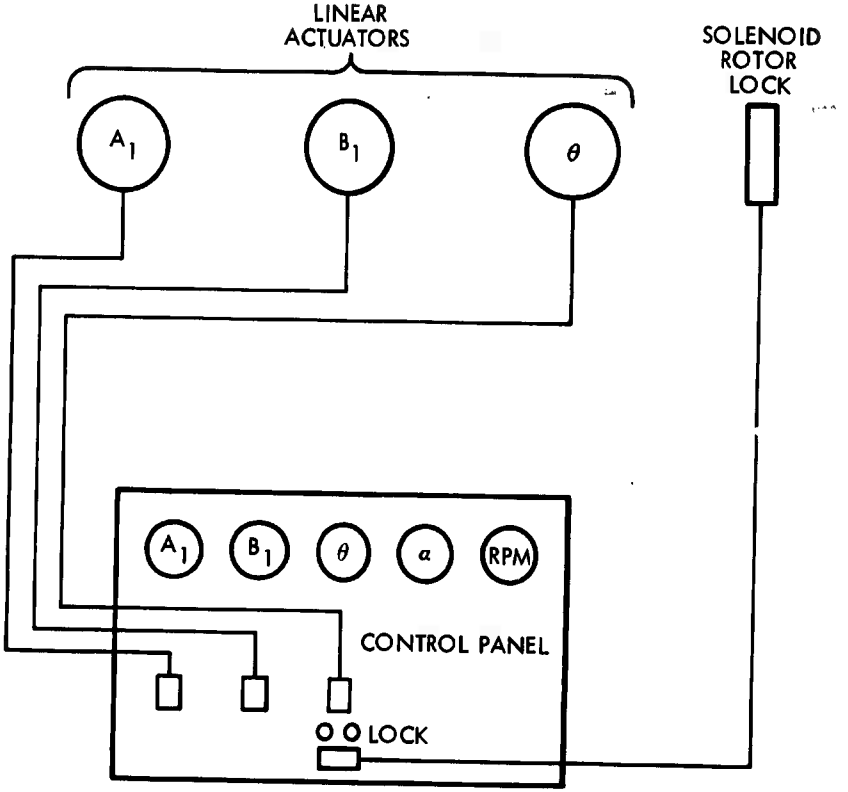

Figure 18. Control Wiring Block Diagram

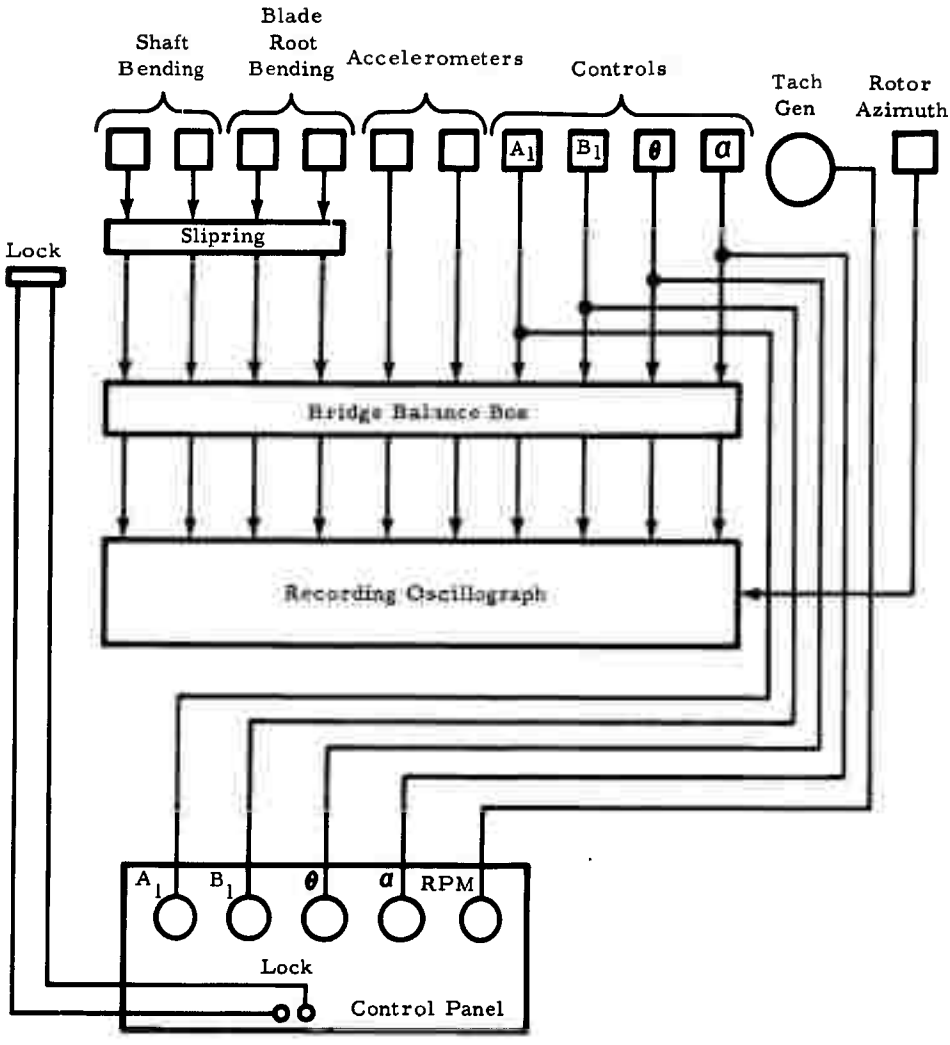

Figure 19. Instrumentation Wiring Block Diagram

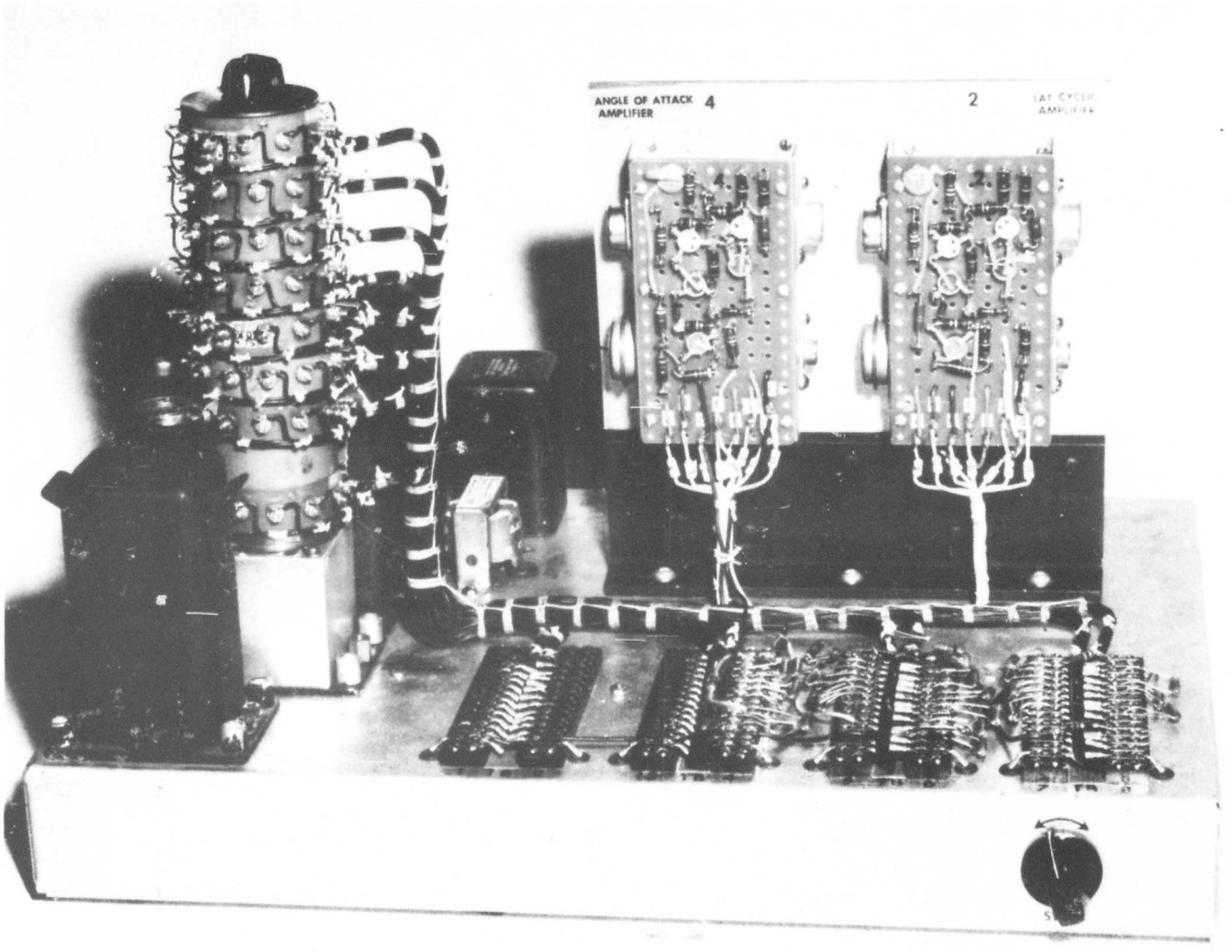

Figure 20. Conversion Control Programmer

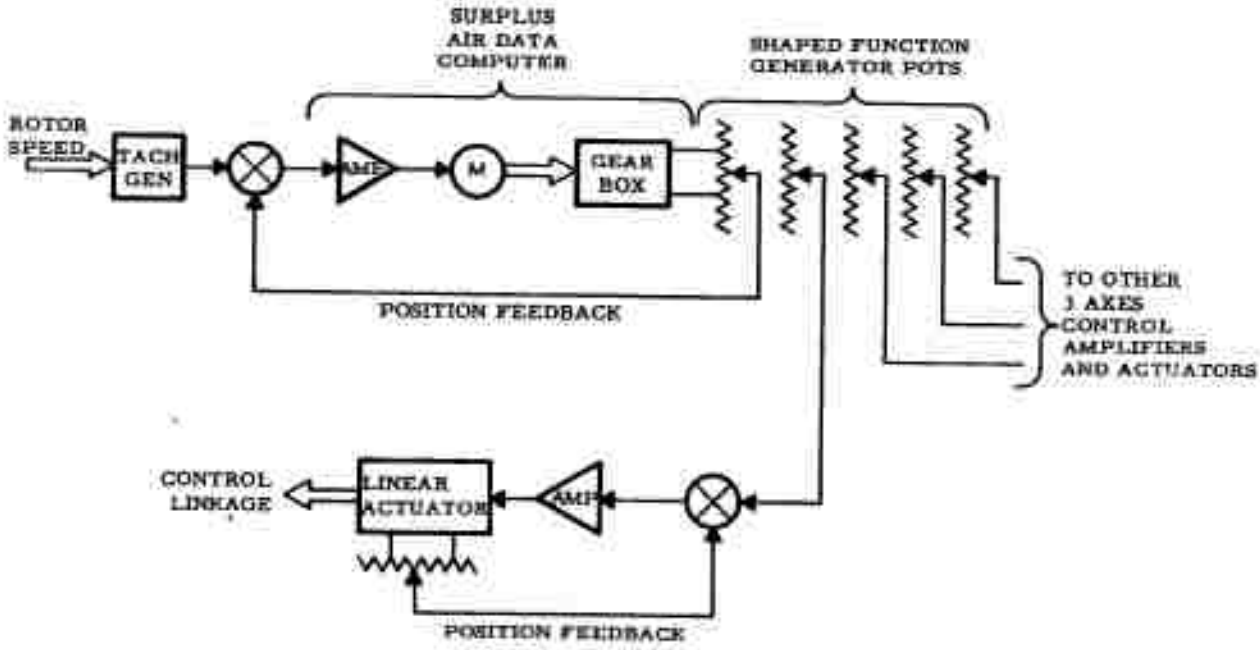

Figure 21. Conversion Control Schematic

ANALYSES OF DYNAMIC CHARACTERISTICS

The dynamic characteristics of the model were analyzed to make sure no problems would occur during the model test program. Three main dynamic considerations were investigated:

Model natural frequency on its support
Rotor/Wing flutter characteristics
Conversion procedure

NATURAL FREQUENCIES

The vibration characteristics were very significant for these particular tests, because it was desired to determine aerodynamic loads on the Rotor/Wing by measuring the bending moments they induced in the rotor shaft. For conventional rotary-wing models, this approach for measuring airloads is not feasible, because the required model flexibility and mass distributions are such that resonances, phase shifts, and so forth, completely obscure the airload data; but for this particular Rotor/Wing model, such an approach was feasible because of its high stiffness. When auxiliary stiffening braces were installed to restrain the model's main support strut, the mount and the model were extremely rigid and had quite high natural frequencies. The rotor could operate at rotational speeds high enough to have reasonable Reynolds numbers on the blades, and still be enough below the three-per-rev resonance speed that the airloads could be read in terms of rotor shaft bending moments. Figure 22 shows the calculated frequency diagram and a comparison

with the frequencies actually measured in the tunnel. The discrepancy between prediction and test is attributed to the mounting of the model on the somewhat flexible balance frame rather than on a rigid base as the calculation assumed. Details of the mathematical vibration analysis are given in Appendix A.

ROTOR FLUTTER CHARACTERISTICS

The rotor system was checked to determine that it should be free from flutter. A sufficient number of operating conditions were analyzed and found free from instabilities to assure safe operations in the wind tunnel. Conditions investigated included:

Helicopter mode
Conversion mode
Airplane mode

Details of the flutter analysis are given in Appendix B.

CONVERSION CHARACTERISTICS

An analysis was made of the conversion maneuver to determine typical programs of fuselage angle of attack and collective and cyclic pitch angles versus rotor speed, for both the rotor-starting and the rotor-stopping cases. In this analysis, the total lift of the Rotor/Wing (hub plus blades) was held constant as the rotor changed speed, steady rolling moments were made equal to zero by the proper control positioning, and an accelerating or decelerating torque was maintained; steady Rotor/Wing pitching moments were assumed to be balanced by the horizontal tail. Figure 23 shows a typical computed control program compared with one experimentally determined in the wind tunnel. Appendix C describes the conversion analysis in detail.

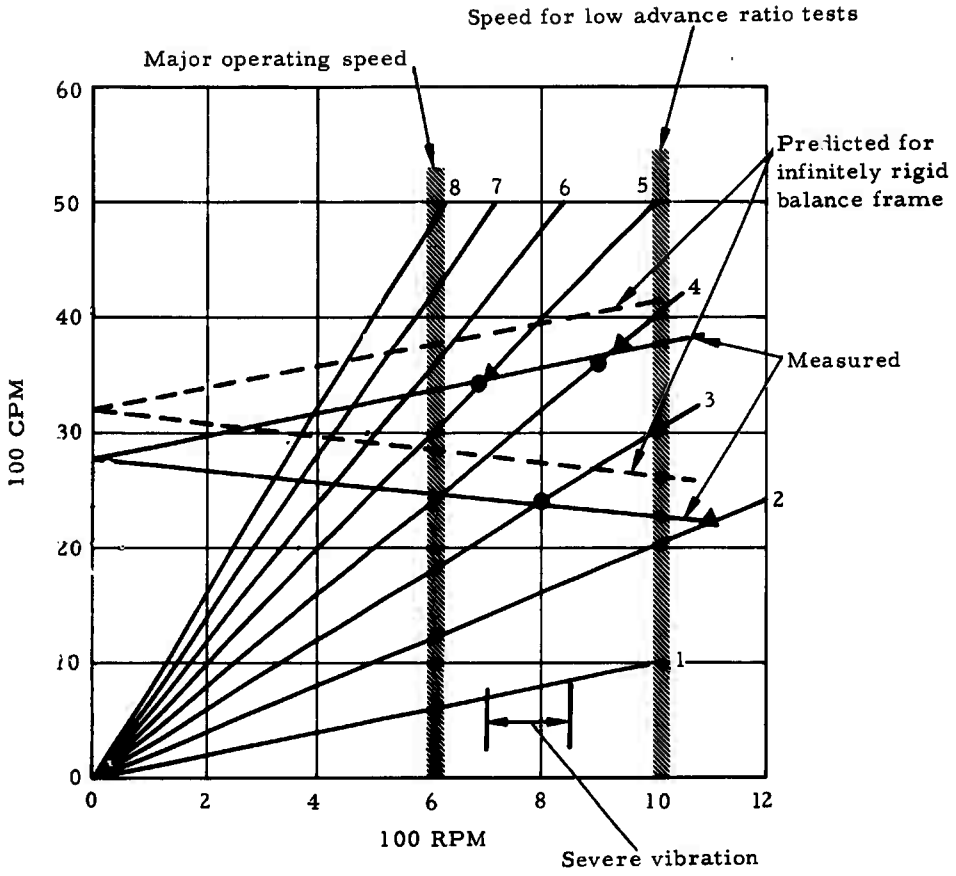

Figure 22. Rotor/Wing Model Vibration Mode

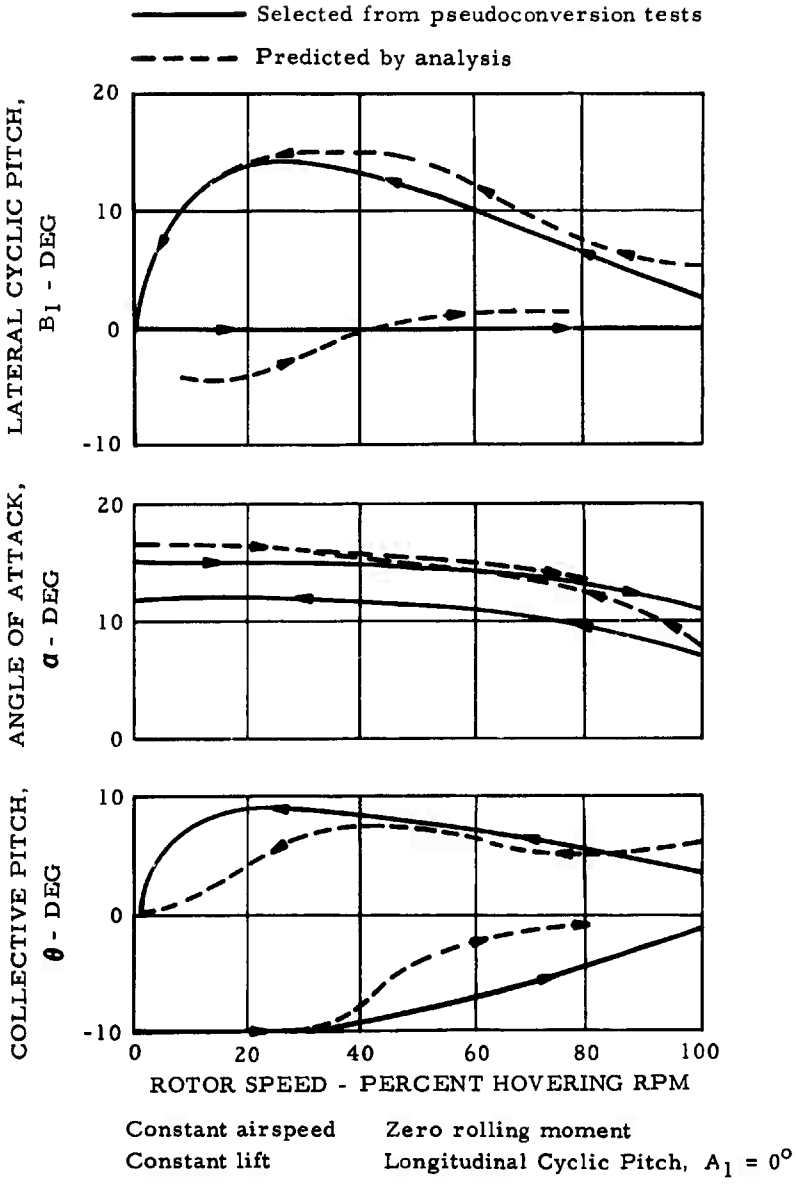

Figure 23. Conversion Control Program

WIND TUNNEL TESTS

This section summarizes the results of the wind tunnel tests of the complete Rotor/Wing model that were conducted in two four-week test series: Series II in March 1965 and Series III in June 1965. The detailed test data are given in Appendix F.*

In each series, the tests were grouped in four categories:

a. Powered rotor
b. Autorotating rotor
c. Conversion
d. Stopped rotor

The most important data from these tests are the aerodynamic characteristics: performance, stability, and control. Dynamic loads data were measured, but they are directly applicable only to this model, because no attempt was made to attain dynamic similarity with any full-scale aircraft. However, these loads data are useful for indicating trends.

The sketch below calls out the major features of the Rotor/Wing model that are discussed in this report.

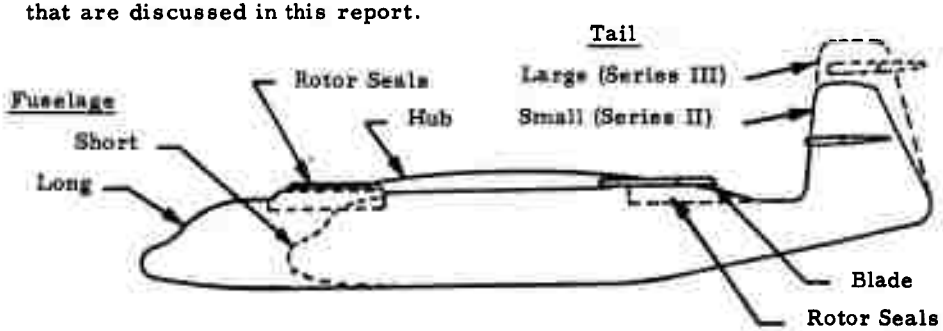

*Results of the Series I tests may be found in Appendix E.

A complete listing of the test runs made in the wind tunnel may be found in Appendix F, Table F-1, configuration and model nomenclature symbols are given in Tables F-2 and F-3, respectively; also in Table 2, page I-51.

All aerodynamic force and moment coefficients presented in this report are based on the rotor disc area and radius, and either tunnel dynamic pressure or model tip-speed, depending on the use to be made of the coefficients:

$$C_L = \left[\frac{L}{q \pi R^2} \right]$$

$$C_M = \left[\frac{M}{q \pi R^3} \right]$$

$$C_T = \left[\frac{T}{\rho \pi R^2 (\Omega R)^2} \right]$$

$$C_Q = \left[\frac{Q}{\rho \pi R^3 (\Omega R)^2} \right]$$

$$C_M^* = \left[\frac{M}{\rho \pi R^3 (\Omega R)^2} \right]$$

All moments are measured about a point on the rotor shaft, as shown in Figure 8.

Bending moments in the blade roots and rotor shaft are nondimensionalized by dividing by the Rotor/Wing lift force and the rotor radius:

$$\overline{\overline{M}} = \left[\frac{M}{LR} \right]$$

To all outward appearances, the Rotor/Wing itself used in these model tests was unchanged throughout. But in the Series III tests, a special

blade pitch control swashplate was used that permitted fixed amounts of second harmonic longitudinal cyclic pitch to be introduced according to the classical blade pitch equation:

$$\theta = A_o - A_1 \cos\psi - B_1 \sin\psi - A_2 \cos 2\psi - B_2 \sin 2\psi - \ldots$$

In a conventional helicopter rotor with flapping, the A_n terms result in rolling response and the B_n terms in pitching response. However, the Rotor/Wing with no flapping hinges has exactly the opposite reaction: A_n resulting in pitch and B_n resulting in roll.

The collective pitch, A_o; longitudinal cyclic pitch, A_1; and lateral cyclic pitch, B_1 were remotely controlled through electric actuators by the model operator. A_2 could be varied in fixed steps by changing components in the swashplate assembly. Fixed A_2 values used were 0°, 3.5°, and 5°. For simple designation, the rotor control configuration was designated $A_2 = 0^\circ$ rotor, for example.

POWERED ROTOR

HOVERING

The Rotor/Wing model was tested in the wind tunnel at zero tunnel speed to simulate hovering. However, the test only approximated hovering. because of the constraint to the airflow through the rotor caused by the tunnel walls, ceiling, and floor, and because of a certain amount of flow around the tunnel induced by the powered rotor. Figure 24 shows the thrust and torque characteristics measured in these hovering tests for two rotor configurations — the conventional helicopter-type swashplate control system ($A_2 = 0^\circ$) and the two-per-rev swashplate system ($A_2 = 5^\circ$) — and compares them with similar data measured on the whirl tower

(Appendix D) for the $A_2 = 0^\circ$ rotor. Reasons for the discrepancy between tunnel and tower tests are the aforementioned constraint in the wind tunnel and the fact that the whirl tower model was pneumatically driven by compressed air jets at the blade tips while the wind tunnel model had a shaft-drive system powered by a hydraulic motor.

HELICOPTER FLIGHT

A combination of model dynamics and wind tunnel speed limitations conspired to limit the tests to the rotor advance ratio range of 0.15 to 0.35. The rotor rpm had to be held at 600 rpm to stay safely below the three-per-rev resonance speed, as described in the section titled Analyses of Dynamic Characteristics, so that the shaft bending moments would be meaningful and the tunnel could not be operated at a dynamic pressure lower than 3 psf. This permitted tests at advance ratios of 0.25 and 0.35. The rotor could be run in a resonance-free region at 1,000 rpm, where the aerodynamic characteristics at an advance ratio of 0.15 could be measured, but this was above the three-per-rev resonance speed and the shaft bending moments were not useful.

Rotor aerodynamic characteristics were measured for a collective pitch range of 0 to 20 degrees over an angle of attack range of -15 to +15 degrees. For each point measured, the pronounced rolling moment of the rigid rotor was made zero by application of lateral cyclic pitch. Figures 25 and 26 show the aerodynamic characteristics of the $A_2 = 0^\circ$ and $A_2 = 5^\circ$ rotors.

A rotor performance method (Reference 3) based on NACA rotor theory was modified to be applicable to the Rotor/Wing, to permit comparison with more conventional helicopter rotors. This modified method should

be applicable to a wide range of Rotor/Wing configuration changes, such as rotor solidity, blade section thickness, hub/blade radius ratio, and blade twist. It also permits prediction of the performance penalties of the Rotor/Wing as compared with a conventional-rotor helicopter of similar rotor diameter and rotor solidity. The rotor solidity for the Rotor/Wing is defined by the standard NACA method

$$\sigma = \frac{bC_e}{\pi R}$$

where

$$C_e = \frac{\int_o^R Cr^2 dr}{\int_o^R r^2 dr}$$

The basic performance method outlined in Reference 3 is used to calculate the hover performance for the Rotor/Wing, with the following modifications:

a. The induced power loss is calculated using the effective rotor annulus area instead of rotor disc area. The effective annulus area is taken as the actual blade area less the tip and inboard losses. The tip and inboard losses are obtained from Reference 4, which presents the tip loss factor, B, as a function of thrust coefficient and number of blades.

b. Rotor blade profile power is increased 30 percent over that of the standard NACA 0015 airfoil section to account for surface roughness and the low Reynolds number of the model blades.

c. Hub profile power loss taken from Appendix D (Figure D-6) is included in the power loss summation.

The results of the calculated hover power required using the modified theory are shown in Figure 27 as the ratio of power required taken from the model test data to the power required as calculated by the modified theory. It can be seen that the modified theory closely predicts the whirl stand test results in the operating thrust range (C_T = 0.010 → 0.014) of the Rotor/Wing aircraft. Figure 28 shows the hover performance penalty of the Rotor/Wing configuration as compared with a conventional helicopter of the same solidity ratio and zero blade twist. The figure shows that the power penalty in hover for the Rotor/Wing is approximately 26 percent relative to that of the conventional rotor helicopter. In terms of thrust, the performance penalty is 20 percent at equal power.

The basic performance method outlined in Reference 3, in conjunction with the charts presented in Reference 5, is used to calculate the helicopter forward flight performance of the Rotor/Wing aircraft, with the following modifications:

a. Blade tip loss factor is taken from Reference 4.

b. Rotor blade profile power is increased 30 percent, as in the hover performance calculations.

c. Hub torque and drag based on the data from Appendix D are included.

d. To account for the low Reynolds number and nonoptimum section of the model blades, ($C_{L_{max}} \cong 0.8$), the calculated blade angle of attack $\alpha_{(1)(270)}$ is increased by 3 degrees before going into the table of NACA 0015 drag data for determination of drag rise due to stall.

Figure 27 shows that fairly good agreement exists between the theoretical power required and the Rotor/Wing model test data in the normal thrust range ($C_T = 0.010 \rightarrow 0.014$). At the higher thrust range, the theory becomes more conservative in predicting power required.

Figure 28 shows the forward flight power required by the Rotor/Wing as compared with a conventional-rotor helicopter. The power required by the conventional-rotor helicopter is calculated assuming a blade section with 1 degree higher stall angle than the model blade section; that is, the calculated $\alpha_{(1)(270)}$ is increased 2 degrees before going into the table of NACA 0015 drag data. Also, the fuselage parasite drag of the conventional heliocpter was assumed to be the same as that of the Rotor/Wing except that the calculated hub skin friction was subtracted out.

The power penalty in forward flight ranges from 62 percent at $C_T = 0.008$ to 20 percent at $C_T = 0.014$. This study indicates the major power penalty of the Rotor/Wing aircraft may be attributed directly to the large hub torque.

Rotor blade root and rotor shaft alternating bending moments, made nondimensional by dividing by rotor lift and radius, are compared in Figure 29 for the $A_2 = 0^\circ$ and $A_2 = 5^\circ$ rotors. The second harmonic pitch input has the effect of reducing these loads by one-fourth to one-half for these powered Rotor/Wing conditions.

The pitch and roll effectiveness were measured in hovering and at $\mu = 0.25$ for zero angle of attack. Figure 30 shows the roll control power of both the $A_2 = 0^\circ$ and $A_2 = 5^\circ$ rotors, and Figure 31 shows the pitch control power of the $A_2 = 5^\circ$ rotor. In roll, the control effectiveness is approximately 1.2 times as great at $\mu = 0.25$ as it is in hovering. In pitch, which was measured only for the $A_2 = 5^\circ$ rotor in Series III, the control effectiveness is approximately 1.6 times as great as in hovering.

Tail effectiveness was measured at the 0.25 advance ratio and for a collective pitch of 10 degrees. For both the small, middle height horizontal tail of Series II and the large, tip-mounted horizontal tail of Series III, the tail effectiveness, $\left[\frac{dC_M}{di_s}\right]$, is 0.005 per degree. See Figures F-15 through F-17, and F-23.

AUTOROTATING ROTOR

To assure true autorotation, the drive chain between the rotor shaft and the hydraulic motor was removed, thus removing all torque restraint. The rotor was made to autorotate at a fixed tunnel speed and various rotor rpm's, thus covering a range of advance ratios. The model was first tested with the tail off and at various collective pitch settings, and then tested at one collective pitch setting with the tail on and the horizontal tail incidence varied to measure tail effectiveness in the autogyro mode. For each point measured, the rolling moment was trimmed to zero by lateral cyclic pitch. Figure 32 shows the rotor aerodynamic characteristics in autorotation; the horizontal tail effectiveness in pitch, $\left[\frac{dC_M}{di_s}\right]$, as derived from Figures F-26 and F-27 is approximately 0.0050 per degree.

In this autorotation mode, the second harmonic pitch control has little effect on the blade chordwise and rotor shaft alternating bending moments.

as may be seen in Figure 33. The flapwise alternating bending moments increase when going from the $A_2 = 0^\circ$ to the $A_2 = 5^\circ$ condition. This is similar to the low collective pitch angle case when the rotor is powered, as seen in Figure 29.

CONVERSION

Conversion, the process of going from the running- to the stopped-rotor condition in flight, was investigated by two means. First, a pseudo-conversion test was made in which the rotor was powered and driven at a number of fixed rpm's while holding tunnel speed and lift constant, and zero rolling moment. For each point, the collective pitch, fuselage angle of attack, lateral cyclic pitch, and torque required to drive the rotor were noted. From these data, a map was constructed, as shown in Figure 34. Using this map and constructing a path through the appropriate torque region, a program could be defined for incorporation in the automatic programmer.

The second method of conversion test was to use the automatic programmer, letting it control the model to start or stop the rotor in the wind while maintaining constant lift and zero rolling moment. A continuous record was taken by the oscillograph to record the model's behavior, and Figures 35 and 36 show the results of such automatic conversions; these are for the $A_2 = 0^\circ$ and $A_2 = 5^\circ$ rotors, respectively. It should be mentioned that these conversions were not fully automatic, because of difficulty with the angle of attack system. First, the desired pitch actuator motor burned out and had to be replaced by a much slower motor; then, the angle of attack actuator tended to hunt continuously. No remedy could be found in the time allowed, so the angle of attack was controlled manually to approximately the schedule required.

Follow through Figure 36 to understand the gross effects that occur during the automatic conversion. Beginning with zero rpm, the collective pitch, θ, is pushed down to -10 degrees and held there until the rpm reaches approximately 100, at which time it is slowly pulled up until it reaches nearly zero at 600 rpm. Meanwhile, the lateral cyclic pitch, B_1, is held constant at zero degrees and the angle of attack is held at approximately 14 degrees. This results in almost constant lift during the acceleration, a steady pitching moment, and almost zero rolling moment. To stop the rotor, the collective pitch is first pulled up to approximately 10 degrees and held there until the rotor speed falls to approximately 150 rpm, and then is decreased to approach zero as the rotor comes to a stop. B_1 is initially moved approximately 12 degrees to the right and held until the rpm reaches 50, and then is centered as the rotor stops. The angle of attack varies from 12 degrees down to 7 degrees and back up to 10 degrees during the deceleration. Again, the lift, pitching moment, and rolling moment stay nearly constant during the deceleration maneuver.

As may be deduced from Figure 36, the results were satisfactory; that is, the rolling moment remained nearly zero and the pitching moment and lift remained almost constant throughout the conversions, both accelerating and decelerating. The lift divergence at the higher rpm's in Figure 35 is attributed to the operator's not following the angle of attack program properly.

The beginning of one automatic conversion run (acceleration) for the $A_2 = 5^\circ$ rotor was analyzed to determine the behavior of the Rotor/Wing at very low rotor speeds. Figure 37 shows the pitching and rolling moments that occurred during the first three revolutions of the rotor. These moments are in the nonrotating fuselage coordinate system, having been converted from the rotor shaft bending moments measured in the rotating rotor system.

There was a small trim change during the first revolution, but the second and third revolutions appear to have reached a steady state. At the end of this third revolution, the rotor was up to 60 rpm, one-tenth of the design helicopter speed. Compensation for this trim change is well within the capability of the horizontal tail, both in pitch and in roll. Superimposed on the trim change is a three-per-rev moment, the alternating magnitude of which is approximately on the order of the alternating shaft bending moments measured in the other flight regimes for this $A_2 = 5^\circ$ rotor. Unfortunately, the model was not instrumented to measure a time history of the lift force.

A portion of the three-per-rev moment trend was apparent from the Series I data. Figures 38 and 39 are plots of the lift and pitching and rolling moment coefficients measured for the triangular and circular hub models, and the three-per-rev trend is apparent; this also indicates the presence of a three-per-rev vertical force oscillation. However, the blade incidence was fixed at zero degrees and there was no rotational velocity. When the rotor first starts to turn, the rotation and the -10 degree collective pitch combine to wipe out the three-per-rev character of the moments during the first half of the revolution, as may be seen by comparing the left end of the curve in Figure 37 with that of Figure 39.

The alternating blade root and shaft bending moments plotted in Figure 40 indicate little preference between the two control swashplate configurations: $A_2 = 0^\circ$ and $A_2 = 5^\circ$. However, these are the peak-to-peak values of the bending moments. A study of the actual oscillograph records (Figures 41 through 44) indicates that the shaft bending moments have a higher proportion of one-per-rev and lower proportions of the higher harmonics when the two-per-rev control is used. Since the

one-per-rev bending moment in the rotating shaft is caused by a stationary force vector in the nonrotating system, this means that the vibrations felt in the fuselage will be lower when the two-per-rev swashplate is used. Harmonic analyses of the shaft bending moment traces were made, and the results are given in the table below; here, the moments are made nondimensional by dividing by the lift and rotor radius.

Table 1. Shaft Bending Moment Harmonic Analysis

	First Harmonic		Second Harmonic		Third Harmonic	
RPM	$A_2 = 0^\circ$	$A_2 = 5^\circ$	$A_2 = 0^\circ$	$A_2 = 5^\circ$	$A_2 = 0^\circ$	$A_2 = 5^\circ$
50	0.167	0.184	0.053	0.052	0.006	0.013
150	0.165	0.200	0.081	0.055	0.006	0.011
300	0.188	0.189	0.072	0.060	0.011	0.012
450	0.187	0.230	0.188	0.132	0.032	0.005
600	0.164	0.200	0.285	0.148	0.024	0.041

Conversion tests were made with a rotor having $A_2 = 3.5^\circ$, but the test results have considerable scatter and it is not conclusive whether there is any benefit for this condition.

STOPPED-ROTOR

Tests were made to evaluate the airplane-type cruise performance, stability, and control of the Rotor/Wing concept with the rotor locked and sealed to the fuselage. The Series I tests had shown that the Rotor/Wing was much more stable in pitch when one blade pointed forward and the other two swept back, (see Figure E-4), so this was the only orientation used in the complete model tests of Series II and III.

Of prime interest is the maximum lift/drag ratio attained by the complete model. The Series I tests (Appendix E) indicated the Rotor/Wing alone could have a maximum L/D in the range of 12 to 13; the Series II and III tests measured the lift/drag characteristics, as well as the other conventional aerodynamic parameters, for a number of Rotor/Wing aircraft configurations. Figure 45 compares the maximum lift/drag ratios determined for a number of aircraft configurations. Hiding the forward blade from the airstream, either by fairing it into the top of the fuselage or removing it, results in the highest L/D ratio. Retracting the forward blade into the hub to remove it from the airstream does not appear practical from a mechanical standpoint, so fairing it into the top of the long fuselage is recommended. Reducing the incidence of the two aft blades has little effect on the maximum L/D; the main effect is to delay the airflow separation on the blades and move the peak of the L/D curve to higher lift coefficients; this also minimizes dynamic pressure losses at the horizontal tail when the tail passes through the wake of the blades.

Extending the blade length while holding the hub size constant, which means reducing the hub/disc area ratio, is beneficial for increasing the maximum L/D ratio. For example, increasing the blade length by 15 percent increases the trimmed $(L/D)_{max}$ by 12 percent, and increasing the blade length by 30 percent increases $(L/D)_{max}$ by 20 percent.

In the hovering case, these blade extensions would reduce the disc loading by 10 and by 20 percent, respectively, with respect to the basic design. Thus, there could be a double benefit in increased maximum L/D and increased hovering efficiency, but a thorough analysis of the effect of increased weight of the longer blades to maintain the required stiffness and the longer fuselage to accommodate the larger rotor would have to be included to assess the overall benefits.

One configuration tested to try to find a suitable way to use the short-nosed fuselage without the L/D penalty of the forward blade extending over the cockpit was with the forward blade turned up to a 90-degree incidence. This resulted in a trimmed maximum L/D of 8.5, only four percent lower than the long-nosed configuration with normal-length blades.

The wing span efficiency, calculated from the lift and drag coefficient data below the angle of attack for $(L/D)_{max}$, is listed in Figure 46 for the various Rotor/Wing configurations. Based on these data, and in the light of the Reynolds number corrections such as those recommended by Reference 6 for correcting to full-scale, it seems reasonable to expect a 75-percent wing span efficiency.

The slope of the Rotor/Wing lift curve is approximately 0.013* per degree for all Rotor/Wing configurations tested. This is in general agreement with published data for highly tapered wings in this aspect ratio category.

*All the aerodynamic coefficients in this report are based on rotor disc area (and rotor radius, for moments); based on wing area, this lift coefficient equals 0.038.

Stall patterns on the Rotor/Wing were studied by observing tufts taped to the upper surface. Figures 47 through 53 show the results of these tuft studies. A major problem area shows clearly in the way the two aft blades stall at fairly low angles of attack. This effect can be ameliorated by pitching the blades nose-down, as seen by comparing Figures 49, 50 and 53, where there are two 5-degree nose-down changes in incidence and a resulting improvement of approximately 0.6 degree in the limiting stall angle of attack per degree of nose-down blade incidence. This does not appear to have much effect on the maximum L/D that can be attained. Wing fences help somewhat, as shown in Figure 52, but installation of fences on a flying machine is questionable. Figures 48 and 53 show how the exposed forward blade disrupts the flow over the top of the wing, even when it is turned up to 90-degree incidence.

The model is unstable in pitch with the tail off, $\left(dC_M/dC_L\right)$ equalling approximately +0.85 for the short-nosed fuselage and +1.23 for the long-nosed. The original horizontal tail tested in Series II provided longitudinal stability up to the angle of attack at which the two aft blades stalled; at higher angles, the tail suffered a loss of effectiveness from a combination of increased downwash when the low aspect ratio hub did all the lifting, and a dynamic pressure loss in the wake of the stalled blades. Figure 54 shows the result. The larger tip-mounted tail of Series III provided stability to higher angles of attack, but it, too, entered the wake of the stalled blades at the higher angles of attack and lost its stabilizing effect, resulting in a mild pitch-up condition (see Figure 55). This indicates a strong need to minimize the blade stall influence.

As in pitch, the model with tail off is unstable in yaw. Through some misadventure, the vertical tail in Series II was not large enough and did not result in a positively stable model (Figure 56). The larger tail of Series III did provide a desired level of stability (Figure 57).

The model exhibited positive dihedral effect, being equivalent to approximately four degrees of dihedral (see Figures 56 and 57).

The downwash at the horizontal tail and sidewash at the vertical tail were calculated from the tail effectiveness. For the Series II horizontal tail location, the downwash factor ($1-d\epsilon/d\alpha$) equalled 0.51; for the Series III tail location, it equalled 0.76. The results of sidewash tests in Series III indicated that the sidewash factor ($1-d\sigma/d\psi$) is very nearly unity. A flow survey at the tail region was made using a pressure rake. Figures 58 and 59 show, respectively, the dynamic pressure field and the downwash angles. These verify the downwash factors determined from the tail effectiveness measurements. It may also be seen from these two figures, especially the latter, that the preferable horizontal tail location is high on the vertical tail. Here, the horizontal tail tends to avoid very large downwash angles that would be encountered for lower position through the angle of attack range tested. Of course, this says nothing about deep stall effects at very high angles of attack; investigation of these effects should be the subject of future testing.

For roll control in the stopped-rotor mode, two methods are available: using the two aft rotor blades as ailerons, or using the two halves of the horizontal tail differentially for roll as well as in unison for pitch. Both methods were investigated, and the results are shown in Figure 60. The two rotor blades are very effective at low angles of attack, but rapidly lose effectiveness as angle of attack increases, because of the blade

stall problem. The horizontal tail used differentially as the roll control appears to be the preferable method, because adequate moment can be developed and this is not so strongly dependent on angle of attack.

Table 2. Symbols and Nomenclature

General

A_1	Longitudinal cyclic pitch control angle, degrees
A_2	2 per revolution longitudinal cyclic pitch angle, degrees
AR	Wing aspect ratio, locked mode
B_1	Lateral cyclic pitch control angle, degrees
D	Drag force, pounds
i_H	Horizontal tail incidence, degrees
Δi_H	Difference in horizontal tail incidence: mean incidence, $i_H = 0^o$
L	Lift force, pounds
$\mathcal{L}$	Rolling moment, foot-pounds
M	Pitching moment, foot-pounds
M_H	Blade root bending moment in the chordwise direction, inch-pounds
M_V	Blade root bending moment in the flapwise direction, inch-pounds
$M_{S_\parallel}$ $M_{S_\perp}$	Rotor shaft bending moment in two mutually perpendicular directions, inch-pounds
N	Yawing moment, foot-pounds
N_R	Rotor speed, rpm

Q	Torque, foot-pounds
q	Tunnel dynamic pressure, pounds/foot^2
R	Rotor radius, feet
S_W	Effective wing area (Rotor/Wing locked), square feet
V	Tunnel airspeed, feet/second
Y	Side force, pounds
α	Fuselage angle of attack, degrees
β	Fuselage side-slip angle, degrees
θ	Rotor collective pitch angle, degrees
θ_1	Blade twist angle, degrees
μ	Rotor advance ratio, $\frac{60V}{2\pi N_R R}$
ξ	Ratio of blade root radius to blade tip radius
ψ	Azimuth angle of reference rotor blade, degrees

Configuration

B	Rotor blades
C	Aft hub fairing
F	Fuselage
H	Trisector rotor hub with helicopter-type swashplate, $A_2 = 0^\circ$, Series II
H_1	Trisector rotor hub with cam-type swashplate, $A_2 = 3.5^\circ$ (Series III)
H_2	Trisector rotor hub with cam-type swashplate, $A_2 = 5^\circ$ (Series III)
H_3	Trisector rotor hub with cam-type swashplate, $A_2 = 0^\circ$ (Series III)

I	Image strut system
(inv)	Model inverted
L	Hub locked and sealed to fuselage
N_1	Long faired nose - complete fairing
N_2	N_1 with rotor clearance blocks removed
N_3	Short unfaired nose
P	Powered rotor
S	Horizontal tail (small, Series II)
S_1	Horizontal tail (large, Series III)
V	Vertical tail (small, Series II)
V_1	Vertical tail (large, Series III)
Y	Wing fences
Z	Strut-stiffening braces

Series I — Wind tunnel tests of Rotor/Wing-alone models (June 1964); results are described in Appendix E.

Series II — Wind tunnel tests of complete model (March 1965); included powered-rotor, autorotating-rotor, pseudo-conversion, and stopped-rotor tests.

Series III — Wind tunnel tests of complete model (June 1965); included powered-rotor, autorotating-rotor, pseudo-conversion, automatic conversion, manual conversion, and stopped-rotor tests.

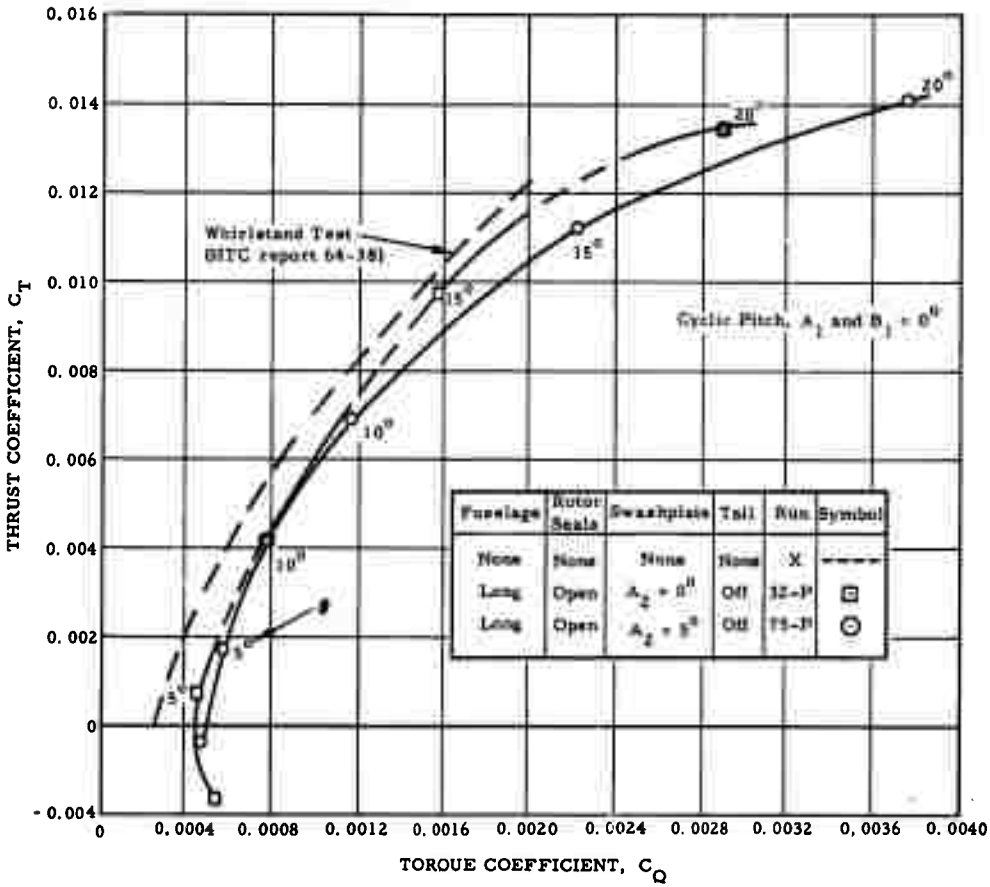

Figure 24. Rotor/Wing Wind Tunnel Tests - David Taylor Model Basin Aerodynamics Laboratory - Hovering Thrust and Torque Coefficients

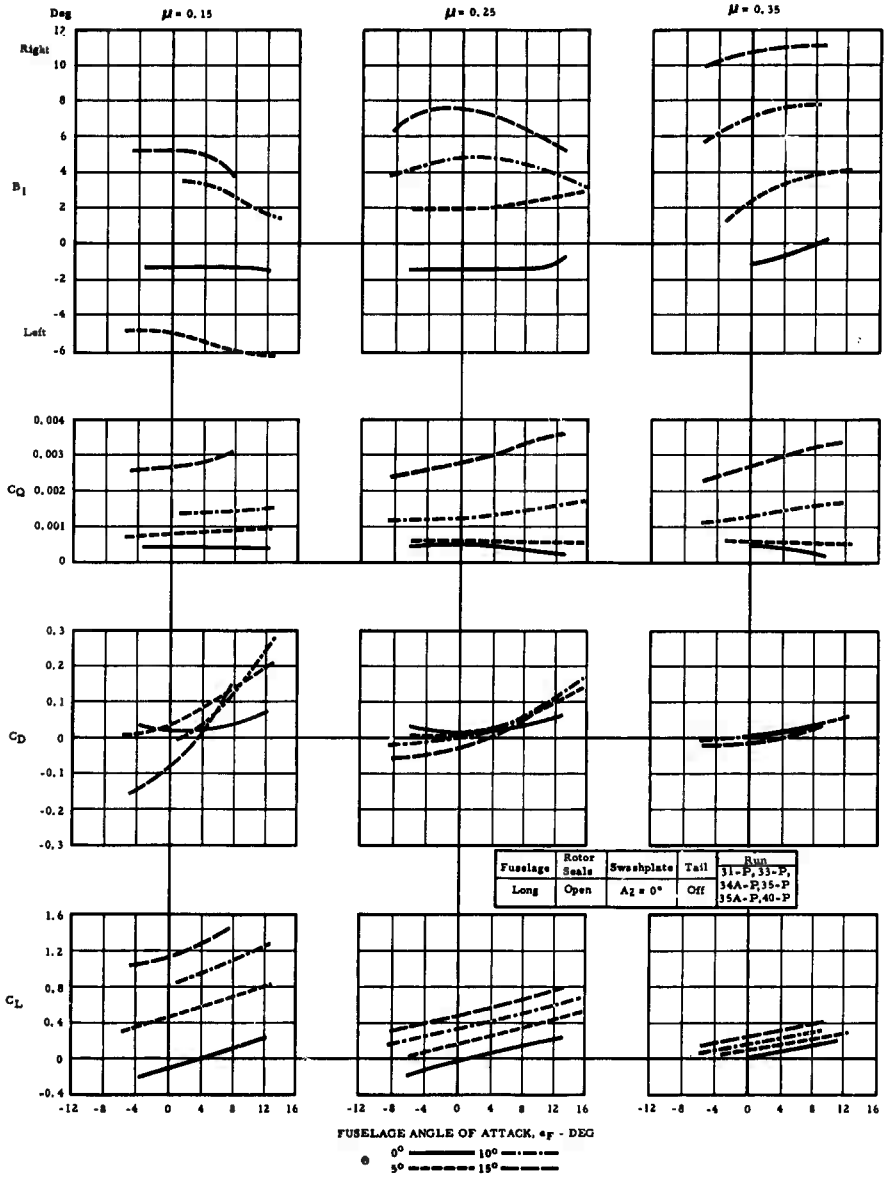

Figure 25. Powered Rotor Aerodynamic Characteristics, $A_2 = 0^\circ$

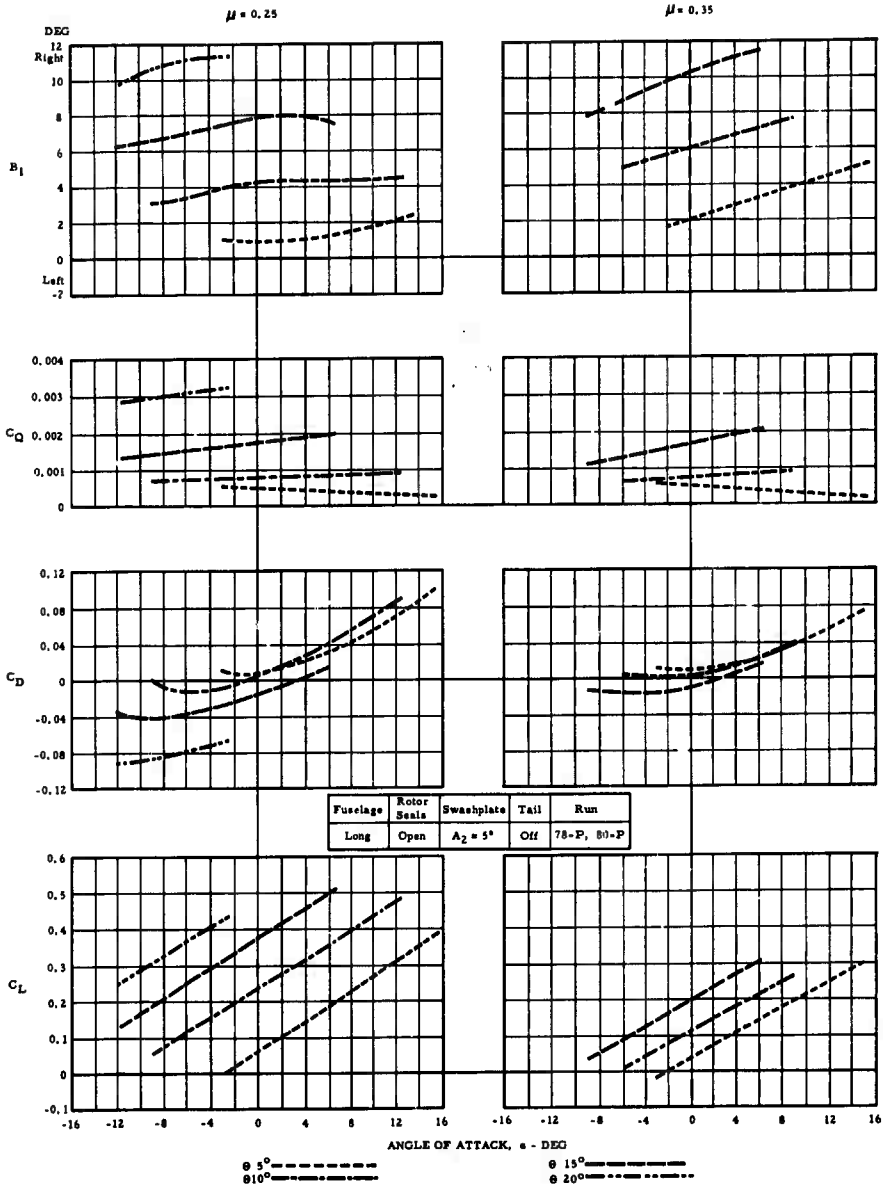

Figure 26. Powered Rotor Aerodynamic Characteristics, $A_2 = 5^\circ$

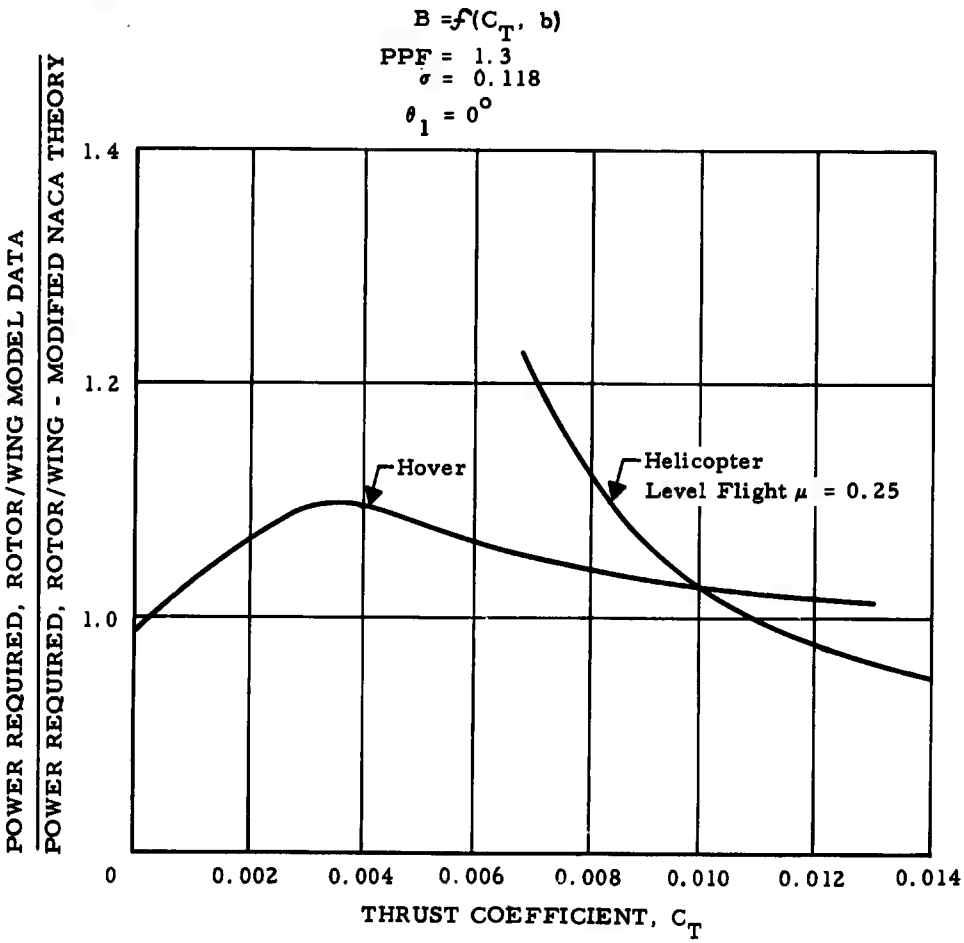

Figure 27. Ratio of Power Required by Rotor/Wing Model to Power Required by NACA Theory

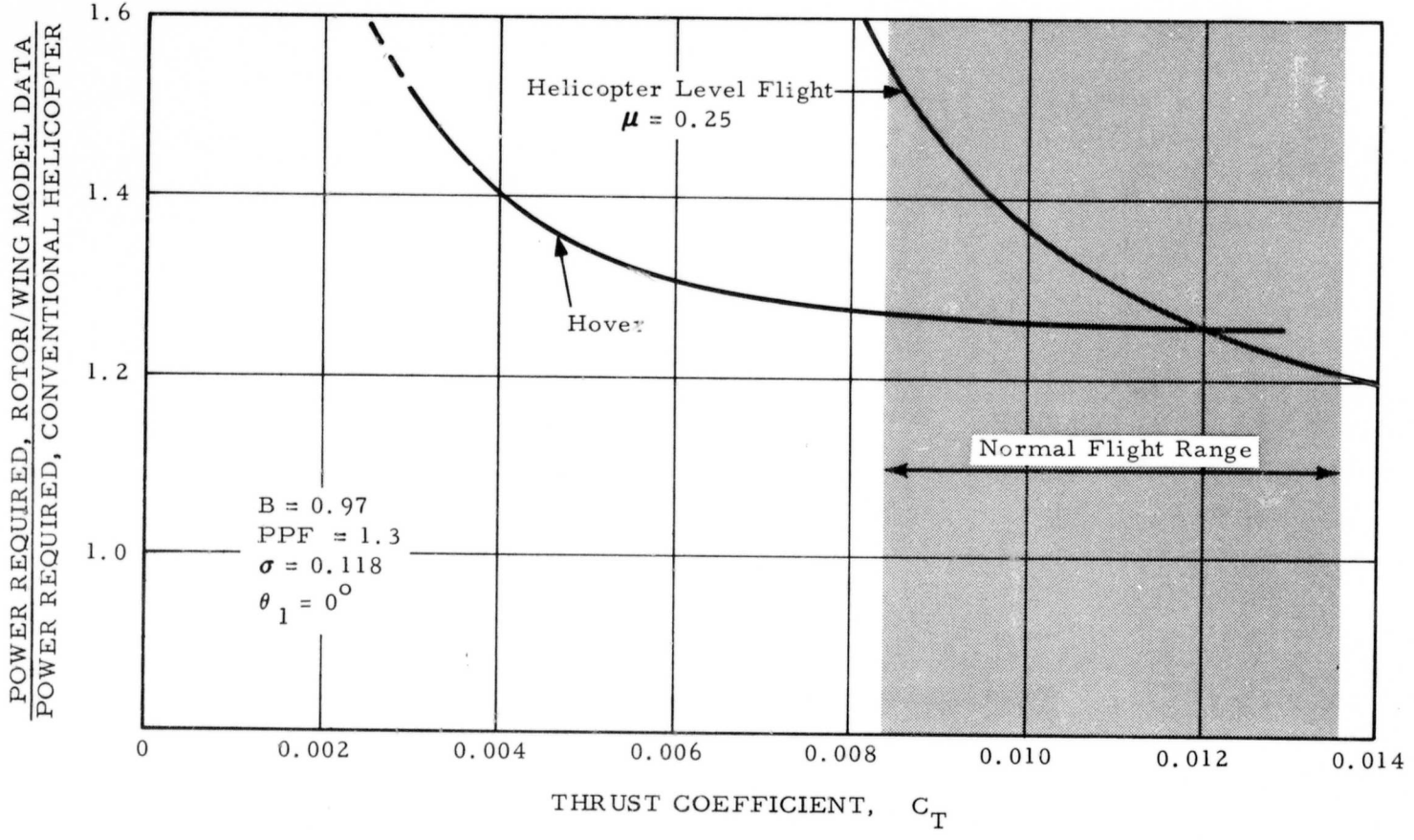

Figure 28. Ratio of Power Required by Rotor/Wing Model to Power Required by Conventional Helicopter

Fuselage	Rotor Seals	Swashplate	Tail	Advance Ratio	Run	Symbol
Long	Open	$A_2 = 0^\circ$	Off	.25	31-P	Solid
Long	Open	$A_2 = 0^\circ$	Off	.35	35A-P	Solid
Long	Open	$A_2 = 5^\circ$	Off	.25	78-P	Open
Long	Open	$A_2 = 5^\circ$	Off	.35	80-P	Open

△ $\theta = 5^\circ$ ◇ $\theta = 10^\circ$ □ $\theta = 15^\circ$ ○ $\theta = 20^\circ$

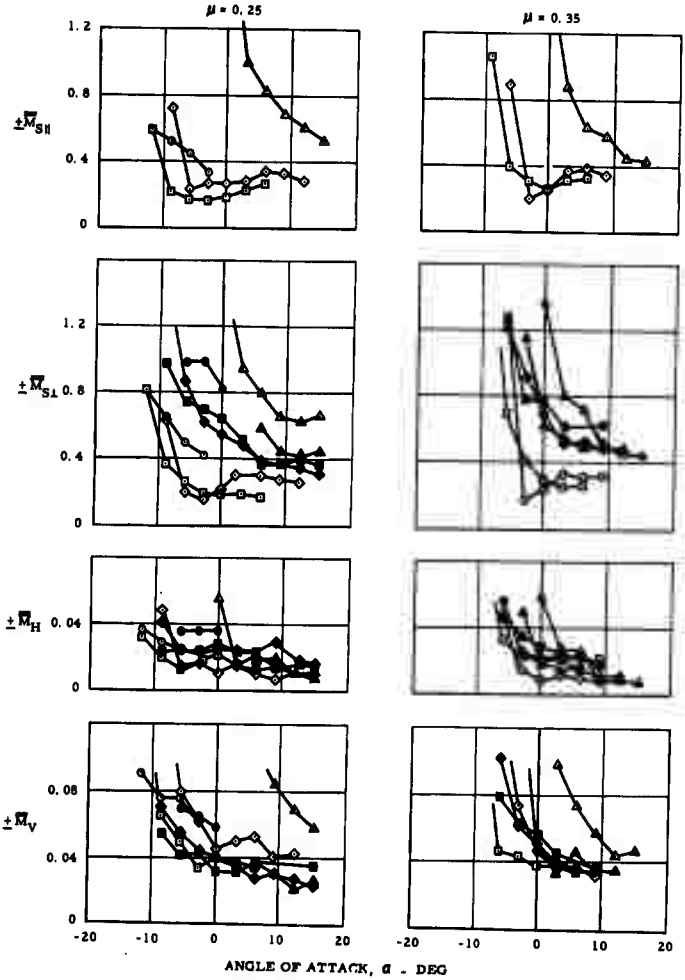

Figure 29. Blade Root and Shaft Alternating Bending Moments

Fuselage	Rotor Seals	Swashplate	Tail	Advance Ratio	Run	Symbol
Long	Open	$A_2 = 0^\circ$	Off	0	32-P	●
Long	Open	$A_2 = 5^\circ$	Off	0	76-P, 77-P	▲
Long	Open	$A_2 = 0^\circ$	Off	.25	40-P	o
Long	Open	$A_2 = 5^\circ$	Off	.25	79-P	△

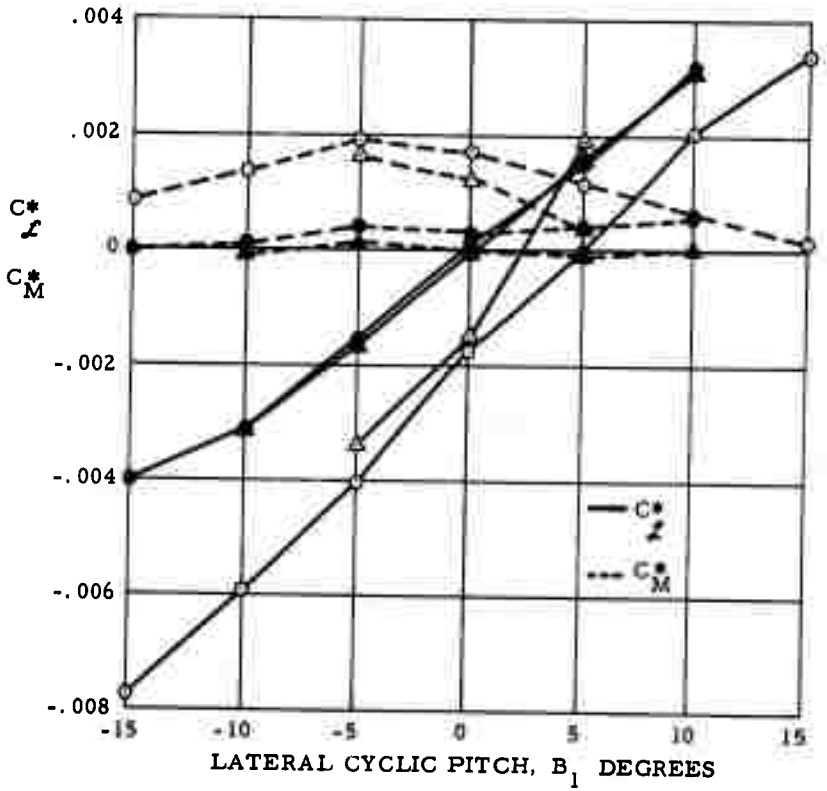

Figure 30. Roll Control in Helicopter Flight

Fuselage	Rotor Seals	Swashplate	Tail	Advance Ratio	Run	Symbol
Long	Open	$A_2 = 5^\circ$	Off	0	76-P, 77-P	▲
Long	Open	$A_2 = 5^\circ$	Off	0.25	79-P	△

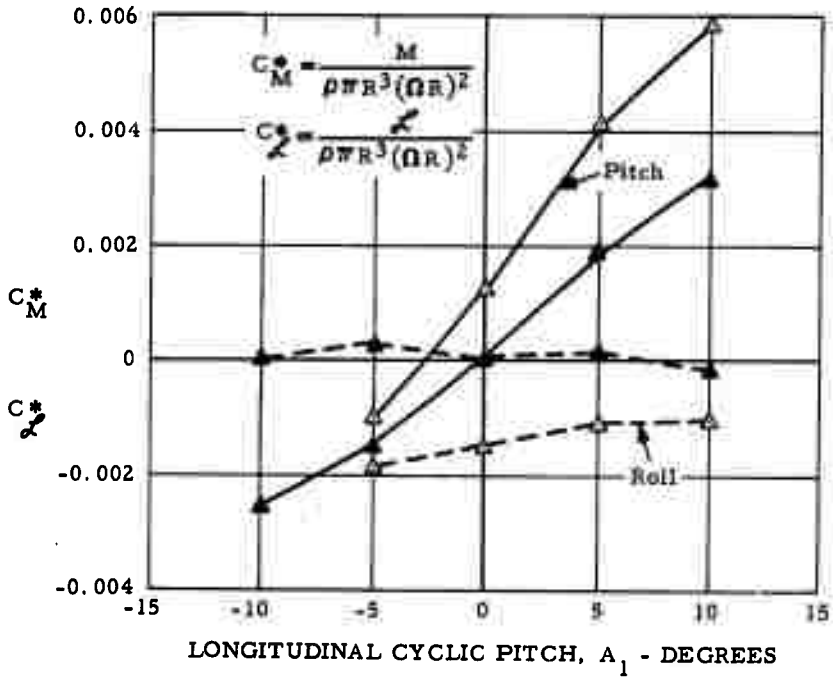

Figure 31. Pitch Control in Helicopter Flight

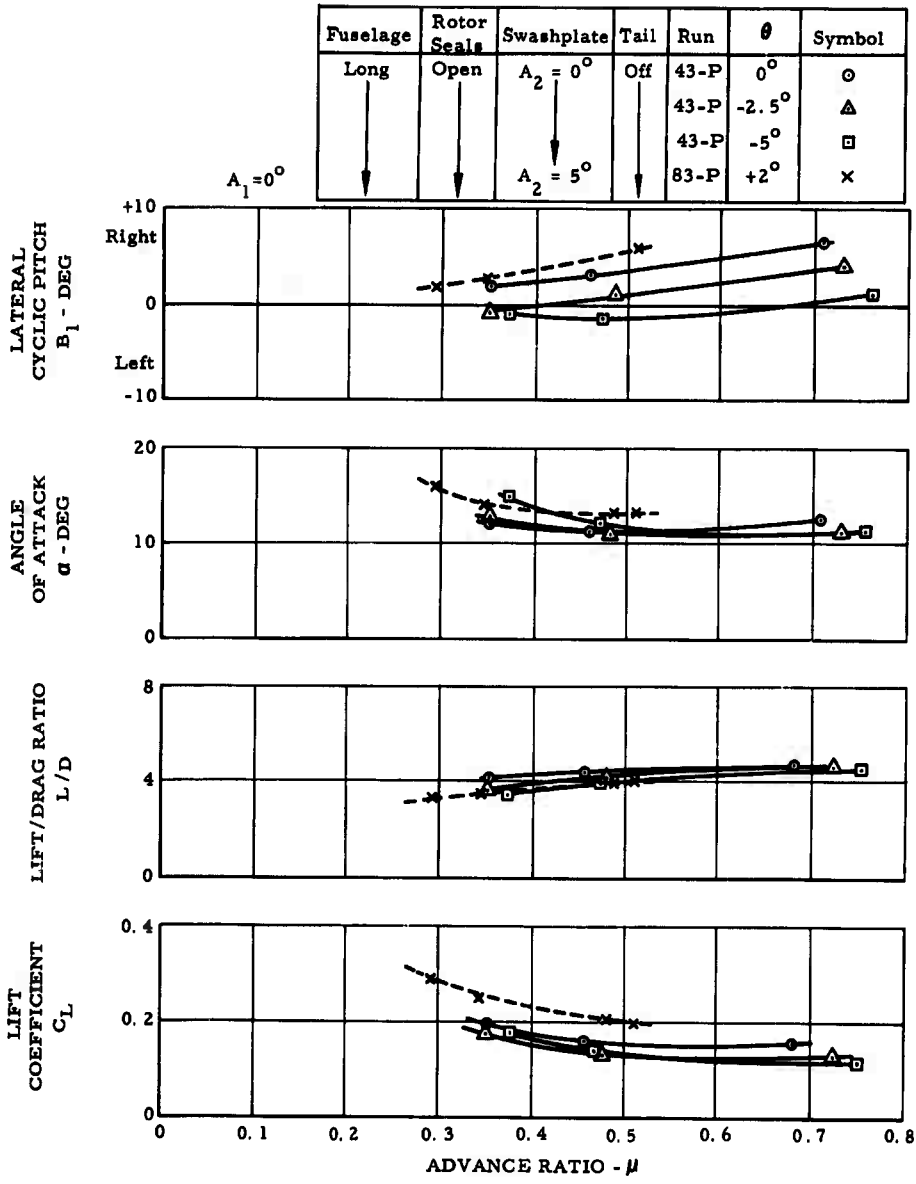

Figure 32. Autorotating Rotor Characteristics

Fuselage	Rotor Seals	Swashplate	Tail	Run	θ	Symbol
Long	Open	$A_2 = 0°$	Off	43-P	0°	⊙
Long	Open	$A_2 = 0°$	Off	43-P	-2.5°	△
Long	Open	$A_2 = 0°$	Off	43-P	-5°	⊡
Long	Open	$A_2 = 5°$	Off	83-P	+2°	×

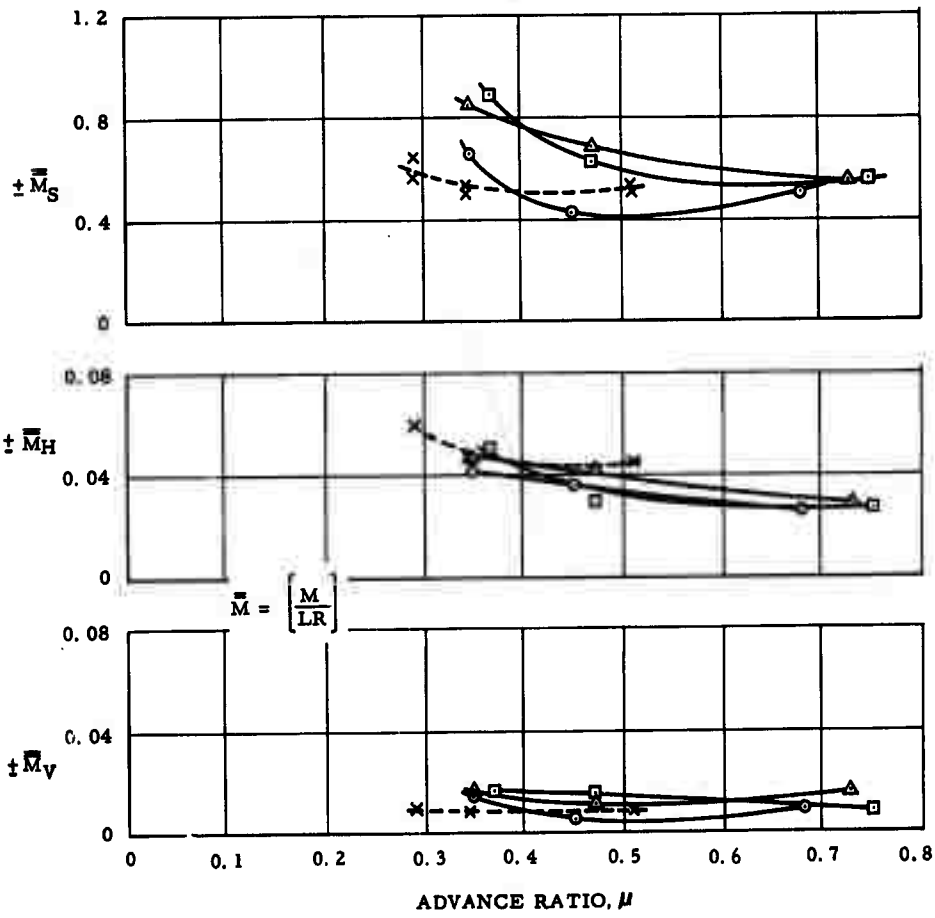

Figure 33. Blade Root and Shaft Alternating Bending Moments in Autorotation

Fuselage	Rotor Seals	Swashplate	Tail	Run
Long	Open	$A_2 = 0^\circ$	Off	41-P

Lift ≈ 50 lb
Rolling moment = 0 ft-lb
Longitudinal cyclic pitch = 0 deg
Dynamic pressure = 7.3 lb/ft^2

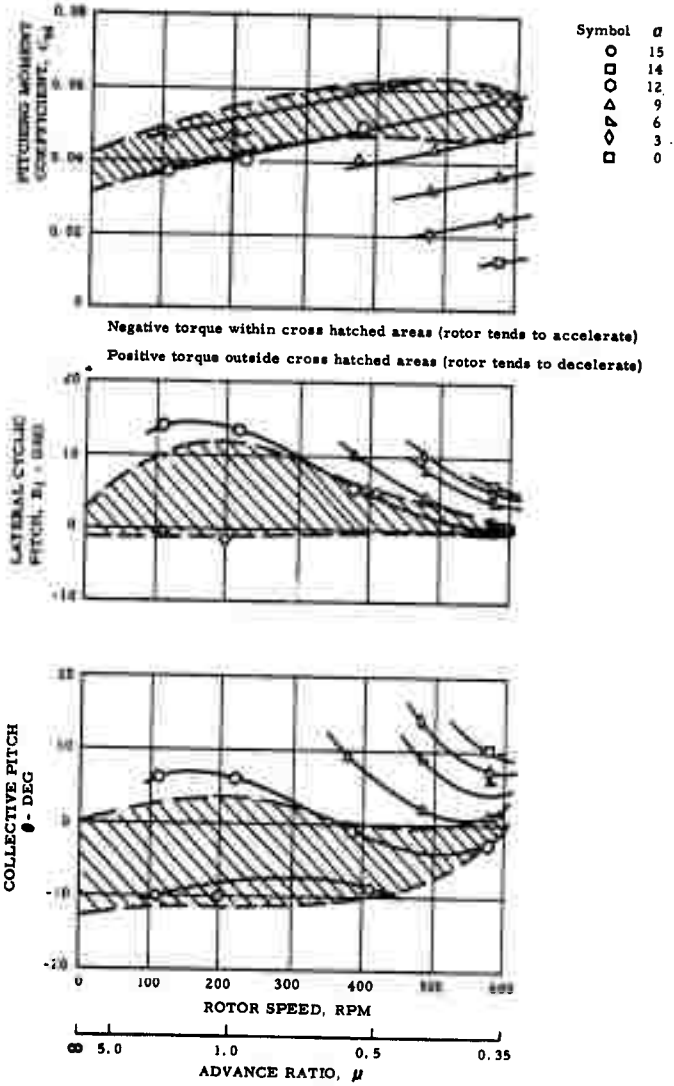

Figure 34. Control Characteristics During Pseudoconversion Test

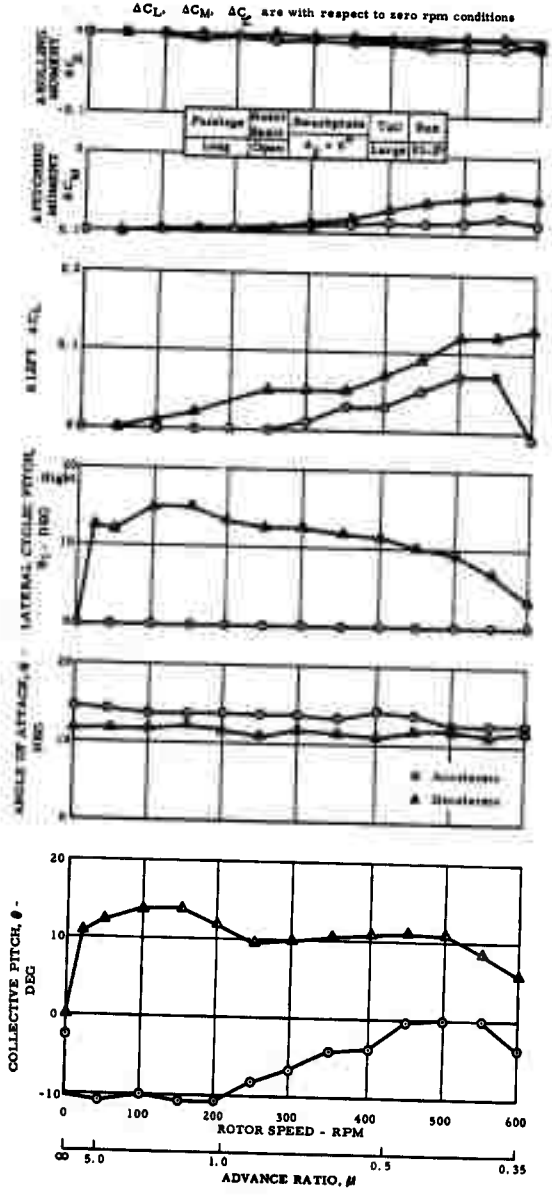

Figure 35. Control Characteristics and Lift and Moment Variations During Automatic Conversion - Run 82-P

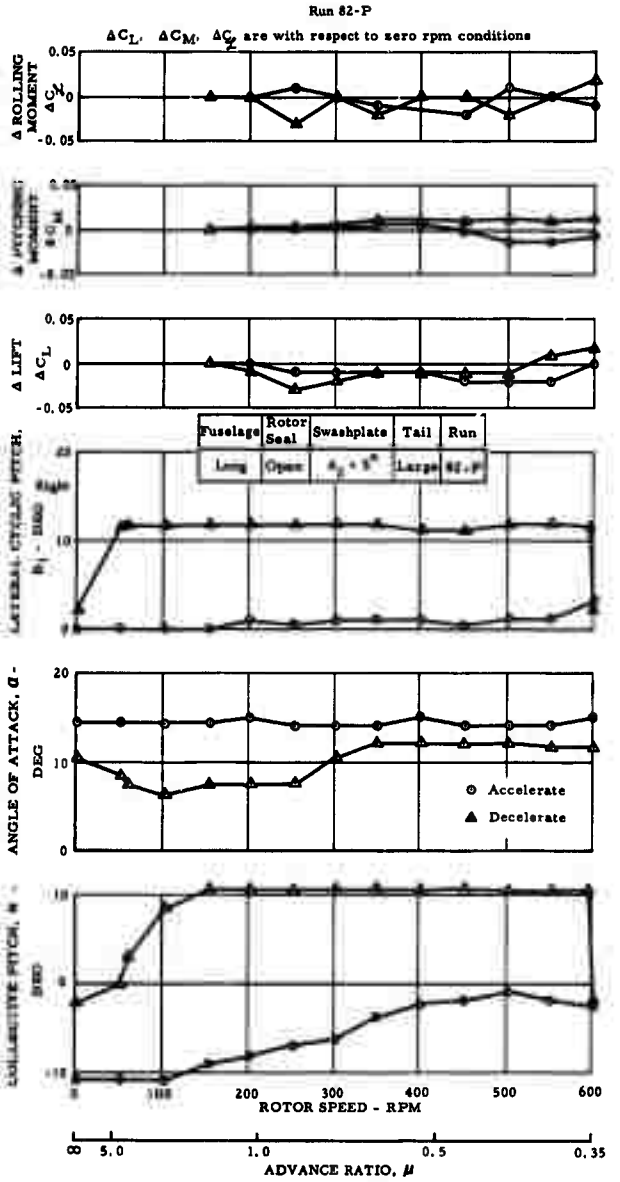

Figure 36. Control Characteristics and Lift and Moment Variations During Automatic Conversion - Run 93-P

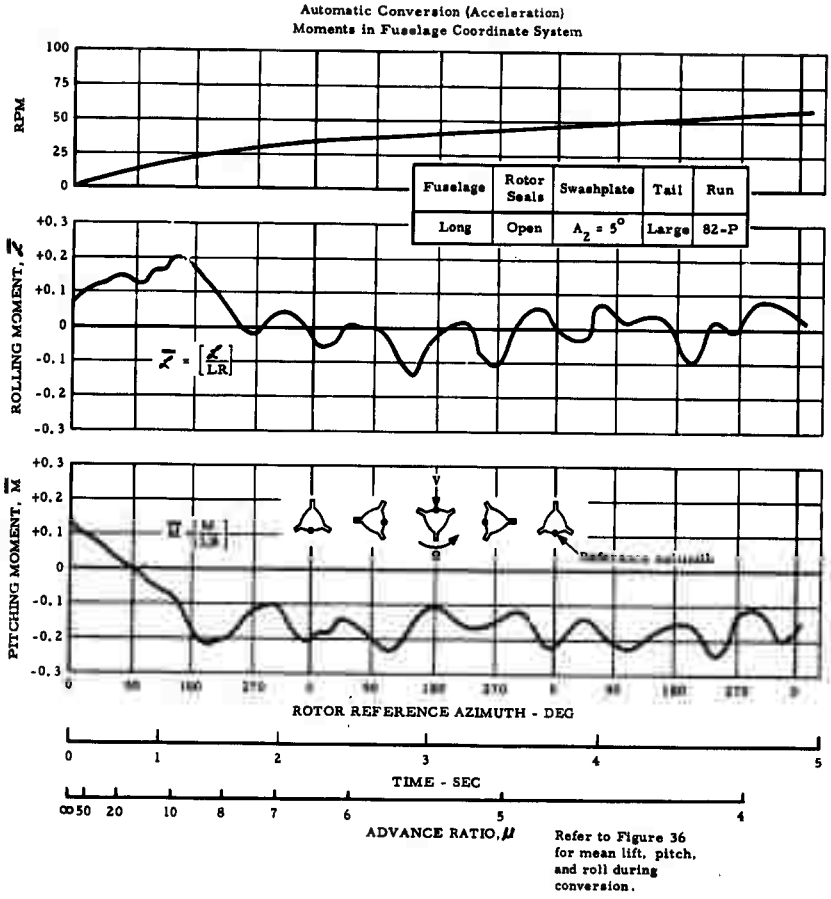

Figure 37. Rotor/Wing Rolling and Pitching Moments During Acceleration From RPM = 0

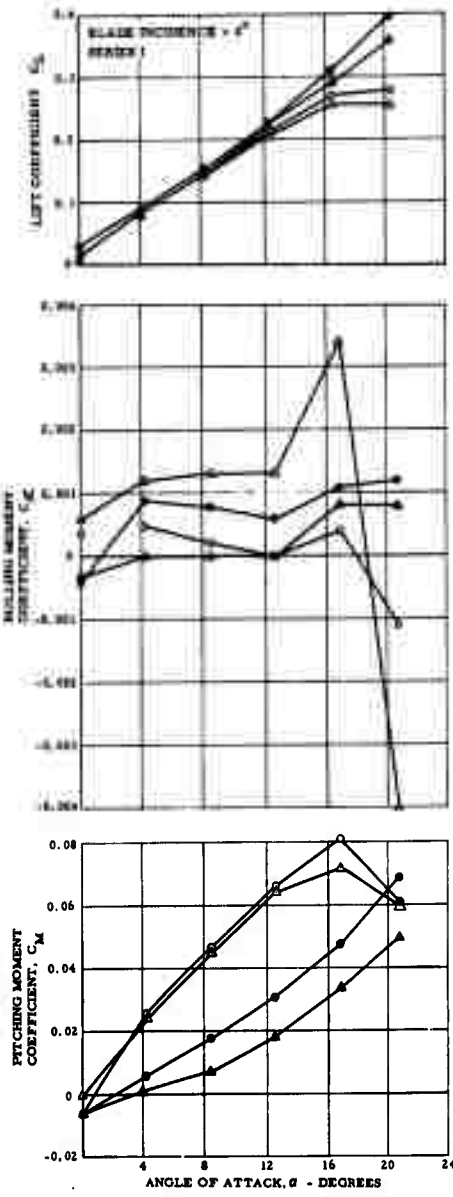

Fuselage	Rotor Seals	Swashplate	Tail	Run	Symbol	Reference Azimuth*
None	None	None	None	6	○	180°
↓	↓	↓	↓	1	●	0°
None	None	None	None	24	△	180°
				19	▲	0°

*Note: These reference azimuths are according to the Series II and III designation. They are 180° out of phase with the designation of Series I.

Figure 38. Lift, Rolling, and Pitching Moments Versus Azimuth Angle - Series I

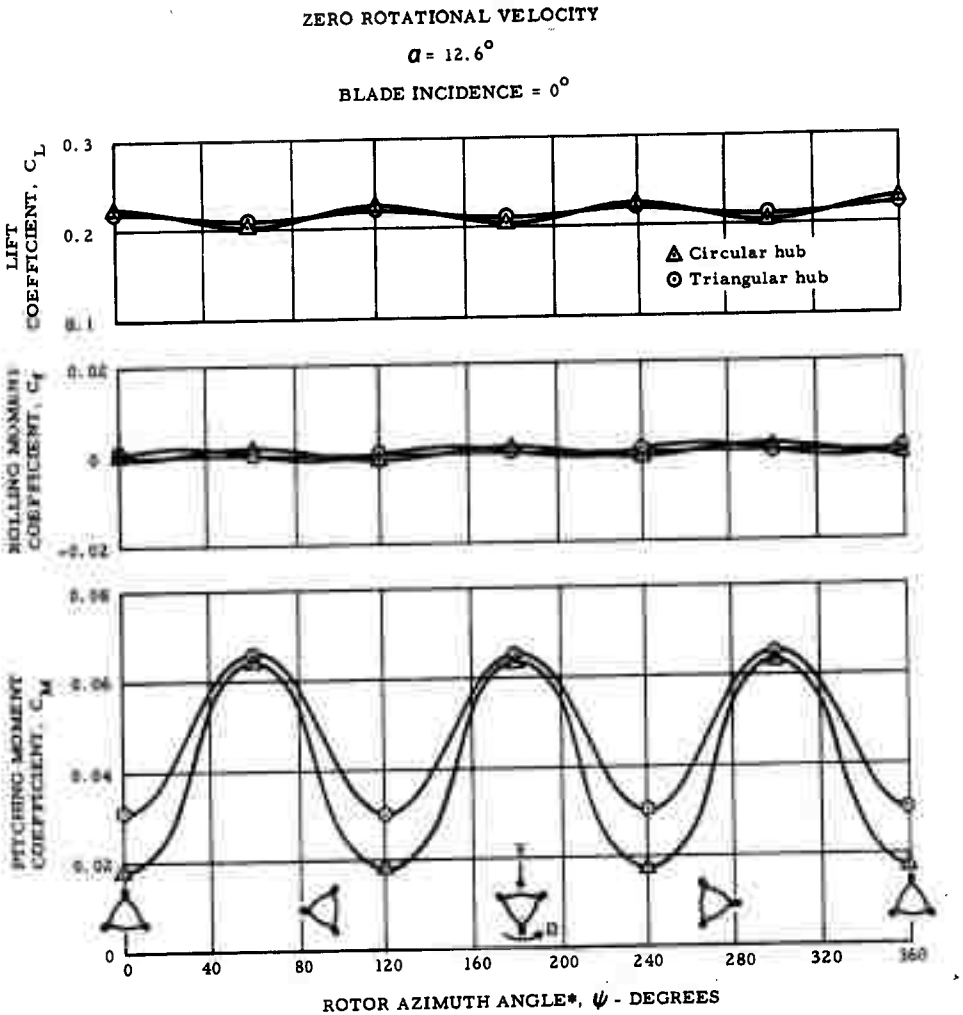

*Series III Nomenclature

Figure 39. Rotor/Wing Rolling and Pitching Moments - Zero Rotational Velocity - Series I

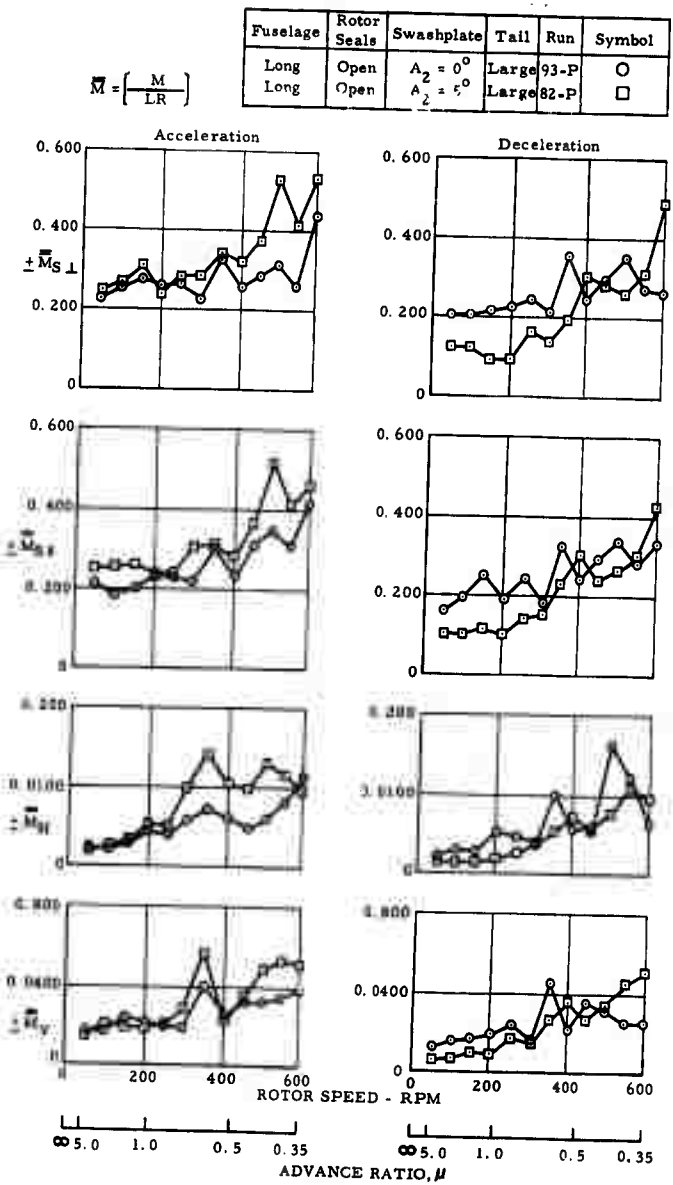

Figure 40. Blade Root and Shaft Alternating Bending Moments During Automatic Conversion

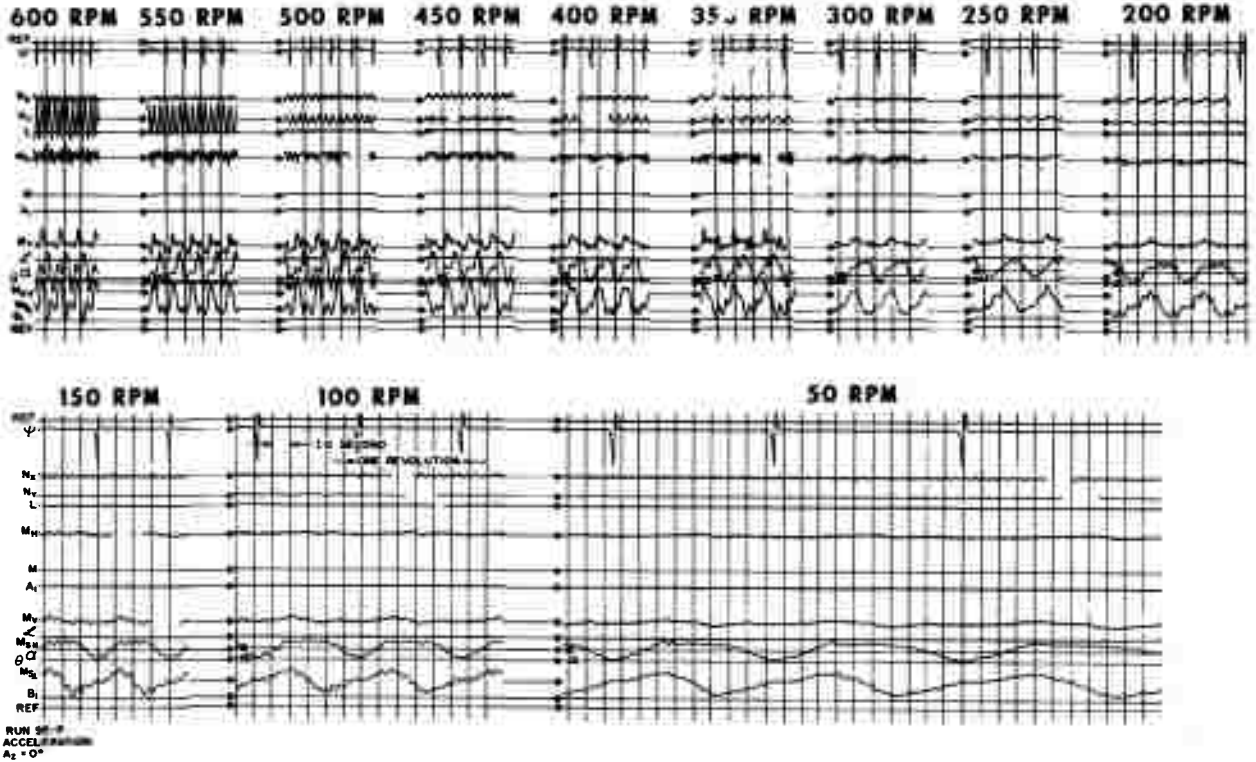

Figure 41. Oscillograph Records - Automatic Conversion, Acceleration, $A_2 = 0°$

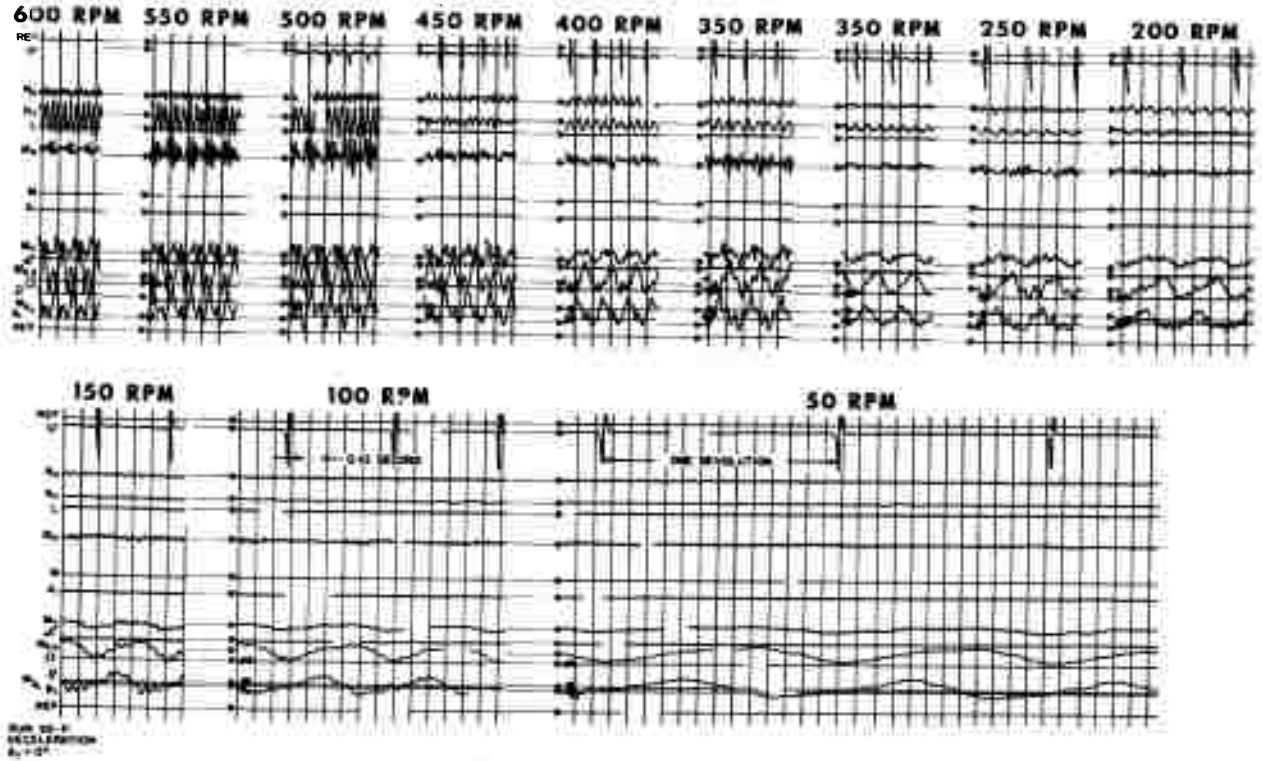

Figure 42. Oscillograph Records - Automatic Conversion, Deceleration, $A_2 = 0°$

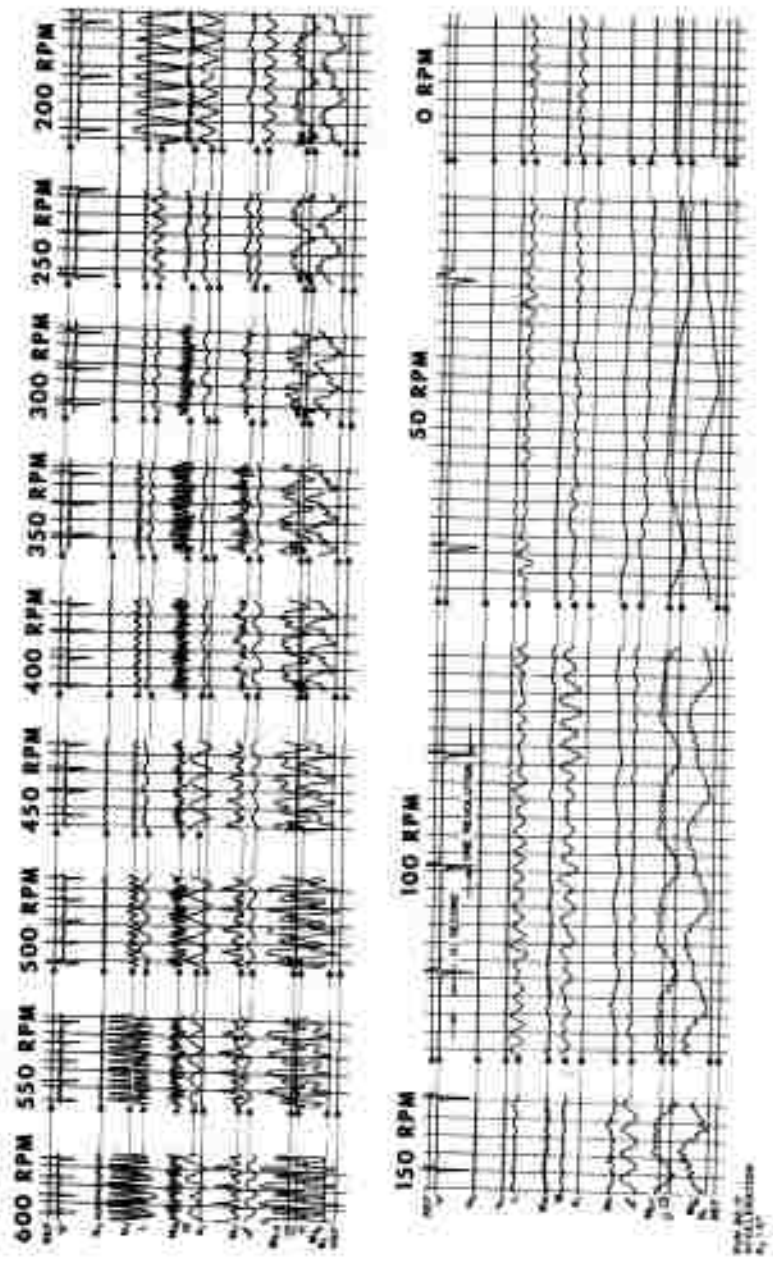

Figure 43. Oscillograph Records - Automatic Conversion, Acceleration, $A_2 = 5°$

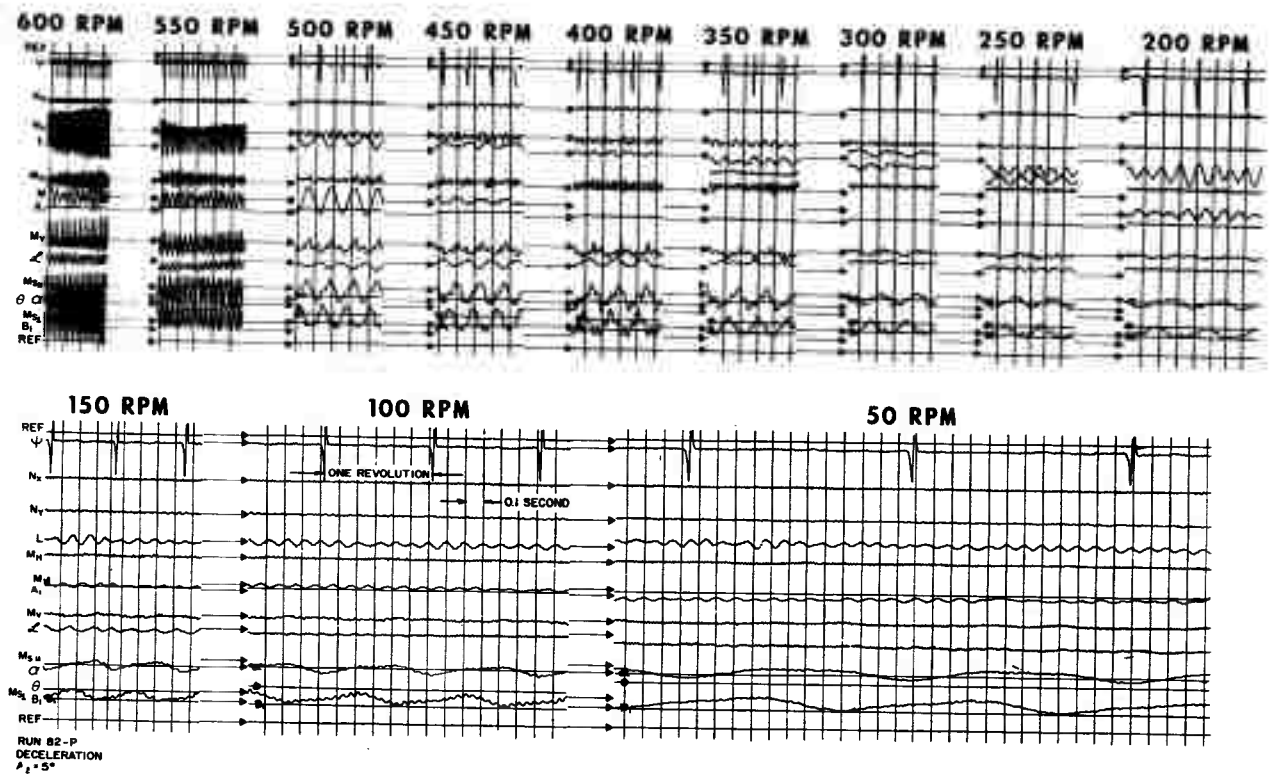

Figure 44. Oscillograph Records - Automatic Conversion, Deceleration, $A_2 = 5°$

Run Number	Fuselage	Tail	Rotor	Blades		Blade Incidence		Fence	Maximum Model (L/D)	
				Forward	Aft	Forward	Aft		Tail-Off	Trimmed
1-P	Long	Off	Sealed	On	On	0°	0°	Off	9.9	-
8-P	Long	Small	Sealed	On	On	0°	0°	Off	-	8.6
28-P	Long	Small	Unsealed	On	On	0°	0°	Off	-	6.9
60-P	Long	Large	Sealed	On	On	0°	0°	Off	-	8.8
98-P	Long	Large	Sealed	On	On	0°	-10°	Off	-	8.6
97-P	Long	Off	Sealed	On	On	0°	0°	On	8.5	-
106-P	Long	Off	Sealed	On	*2.5-in. Ext.	0°	0°	Off	10.4	-
105-P	Long	Large	Sealed	On	*2.5-in. Ext.	0°	0°	Off	-	9.7
107-P	Long	Off	Sealed	On	** 5-in. Ext.	0°	0°	Off	10.8	-
108-P	Long	Large	Sealed	On	** 5-in. Ext.	0°	0°	Off	-	10.3
25-P	Short	Off	Sealed	On	On	0°	0°	Off	7.9	-
19-P	Short	Small	Sealed	On	On	0°	0°	Off	-	7.1
48-P	Short	Off	Sealed	Off	On	-	0°	Off	11.4	-
47-P	Short	Small	Sealed	Off	On	-	0°	Off	-	9.5
49-P	Short	Off	Sealed	Off	On	-	-5°	Off	10.9	-
50-P	Short	Small	Sealed	Off	On	-	-5°	Off	-	10.0
52-P	Short	Off	Sealed	Off	Off	-	-	Off	7.7	-
51-P	Short	Small	Sealed	Off	Off	-	-	Off	-	6.4
99-P	Short	Off	Sealed	On	On	90°	-10°	Off	8.5	-
102-P	Short	Large	Sealed	On	On	90°	-10°	Off	-	8.5

*15 percent blade span extension
**30 percent blade span extension

Figure 45. Stopped-Rotor Maximum Lift/Drag Ratio

Number	Fuselage	Blades		Blade Incidence		Wing Fence	$\frac{dC_L^2}{dC_D}$	AR	$\frac{\pi R^2}{S_W}$	Span Efficiency
		Forward	Aft	Forward	Aft					
1-P	Long	On	On	0°	0°	Off	2.60	2.98	2.91	0.81
97-P	Long	On	On	0°	0°	On	2.40	2.98	2.91	0.75
106-P	Long	On	*2.5-in. Ext.	0°	0°	Off	2.60	3.27	2.86	0.72
107-P	Long	On	** 5-in. Ext.	0°	0°	Off	2.85	3.56	2.81	0.72
25-P	Short	On	On	0°	0°	Off	2.10	2.82	2.75	0.65
48-P	Short	Off	On	-	0°	Off	2.25	2.98	2.91	0.70
49-P	Short	Off	On	-	-5°	Off	2.60	2.98	2.91	0.81
52-P	Short	Off	Off	-	-	Off	1.65	1.40	3.38	1.27
99-P	Short	On	On	90°	-10°	Off	2.70	2.98	2.91	0.84

$$e = \frac{dC_L^2/dC_D}{\pi AR} \quad \frac{\pi R^2}{S_W}$$

*15 percent blade span extension
**30 percent blade span extension

Figure 46. Wing Span Efficiency Factor - Tail Off, Rotor Sealed to Fuselage

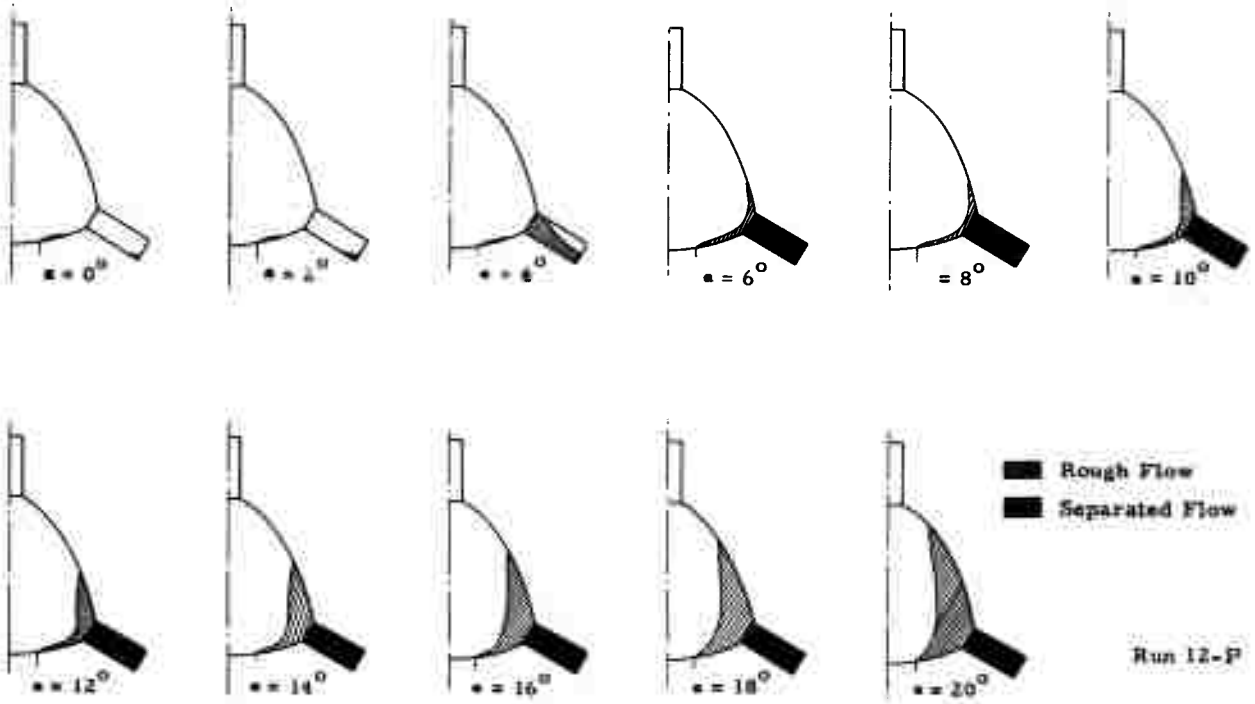

Figure 47. Rotor/Wing Stopped-Rotor Stall Pattern - Long-Nosed Fuselage

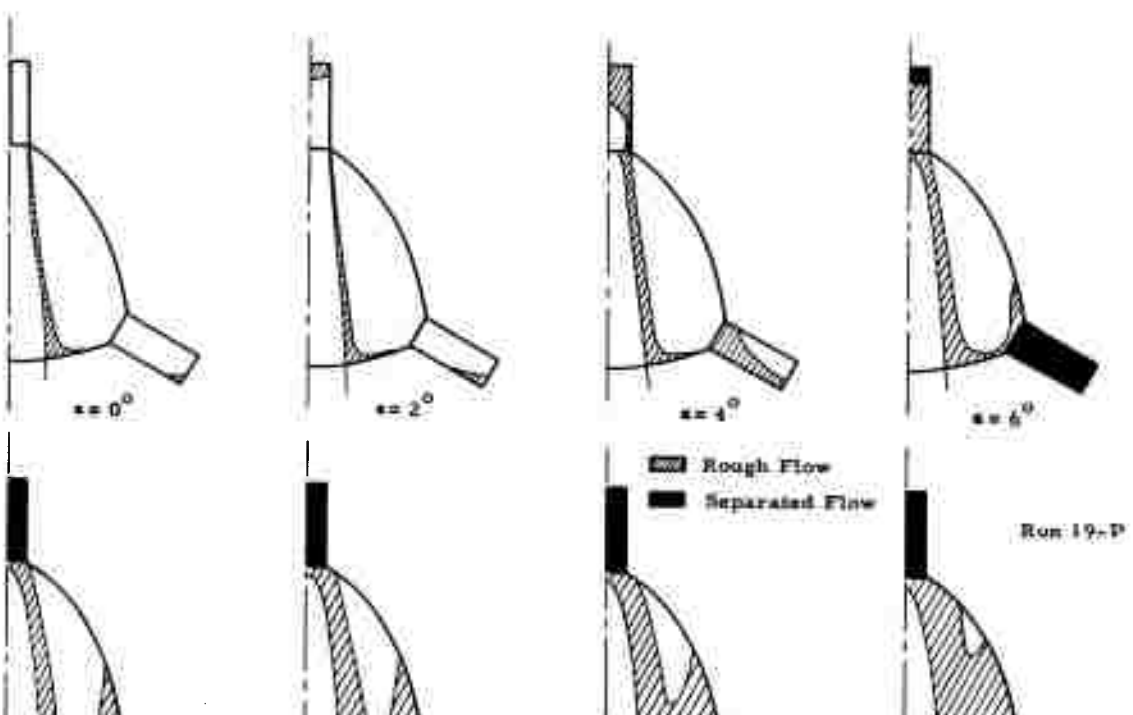

α = 16°, 18°, 20° same as 14° except stall covers entire leading edge of hub

Figure 48. Rotor/Wing Stopped-Rotor Stall Pattern - Short-Nosed Fuselage

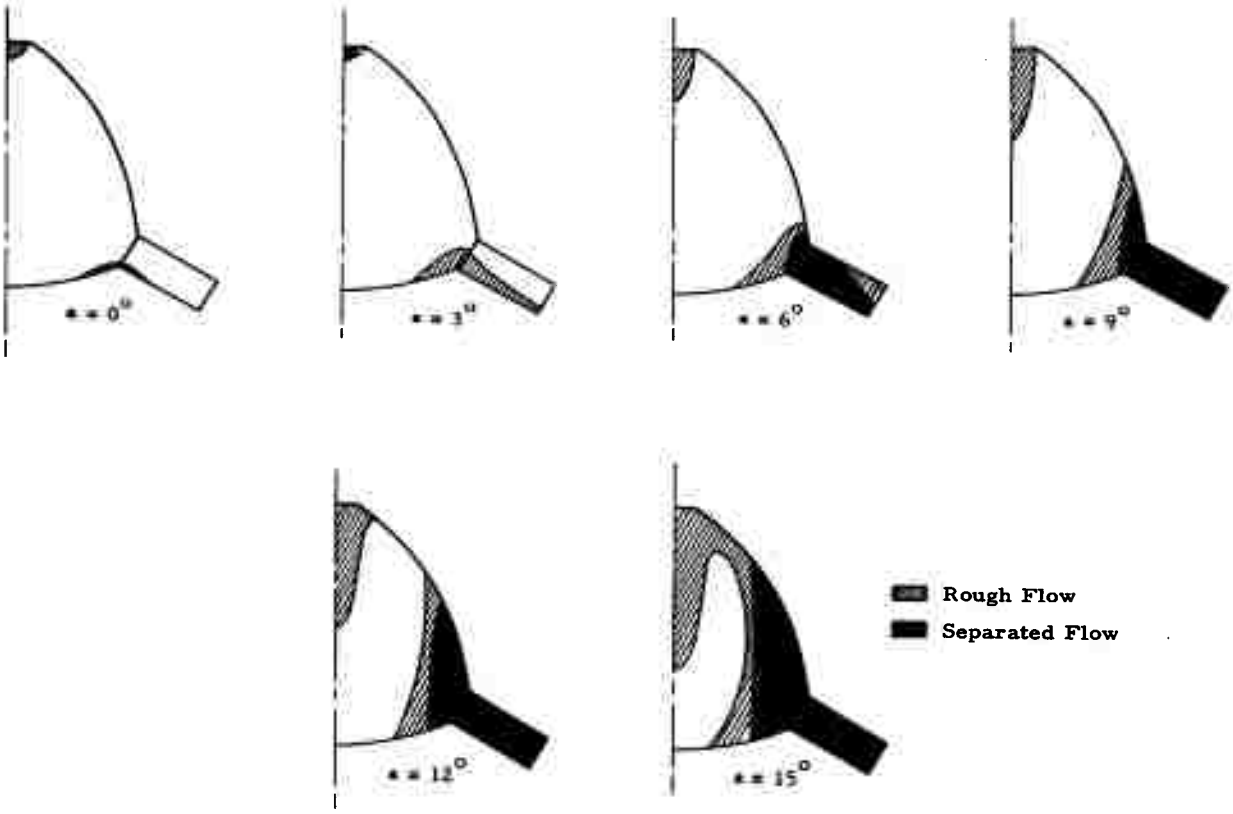

Figure 49. Rotor/Wing Stopped-Rotor Stall Pattern - Short-Nosed Fuselage - Forward Blade Off - Aft Blade Incidence = 0^{o}

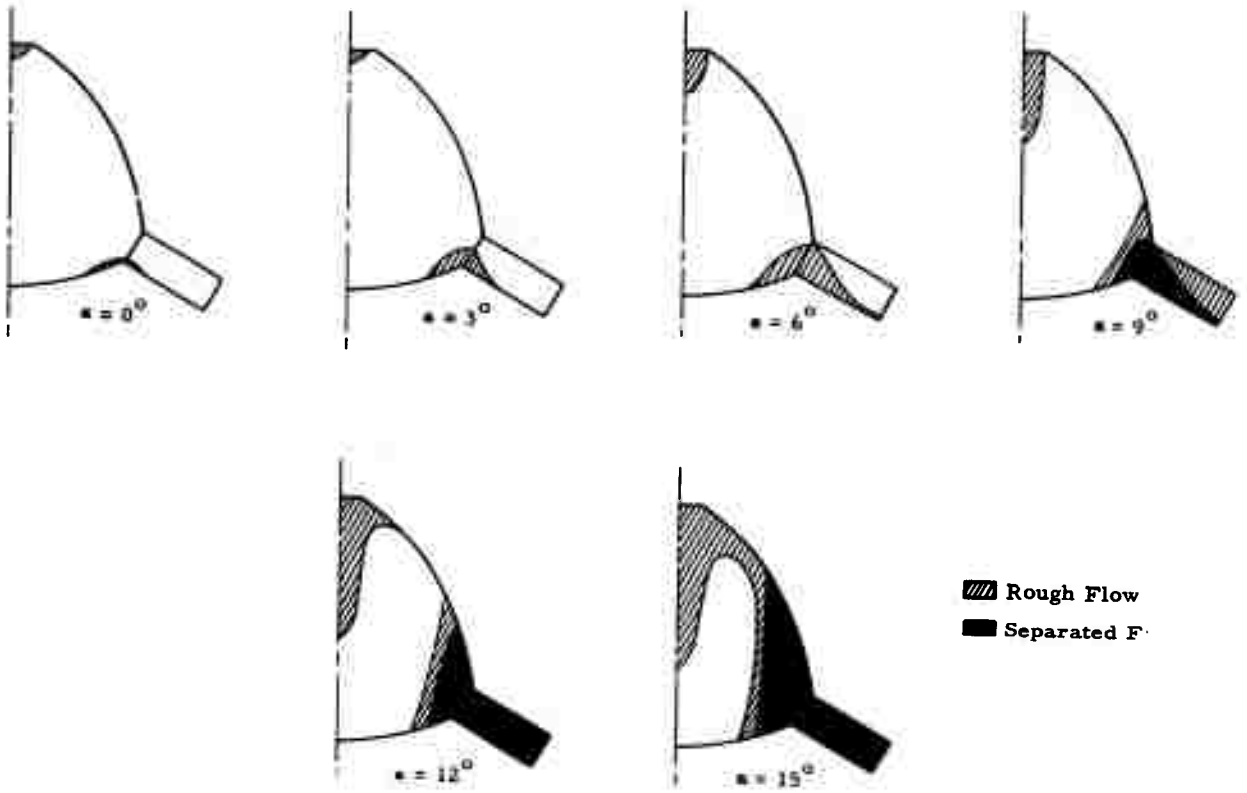

Run 50-P

Figure 50. Rotor/Wing Stopped-Rotor Stall Pattern - Short-Nosed Fuselage - Forward Blade Off - Aft Blade Incidence = 5°

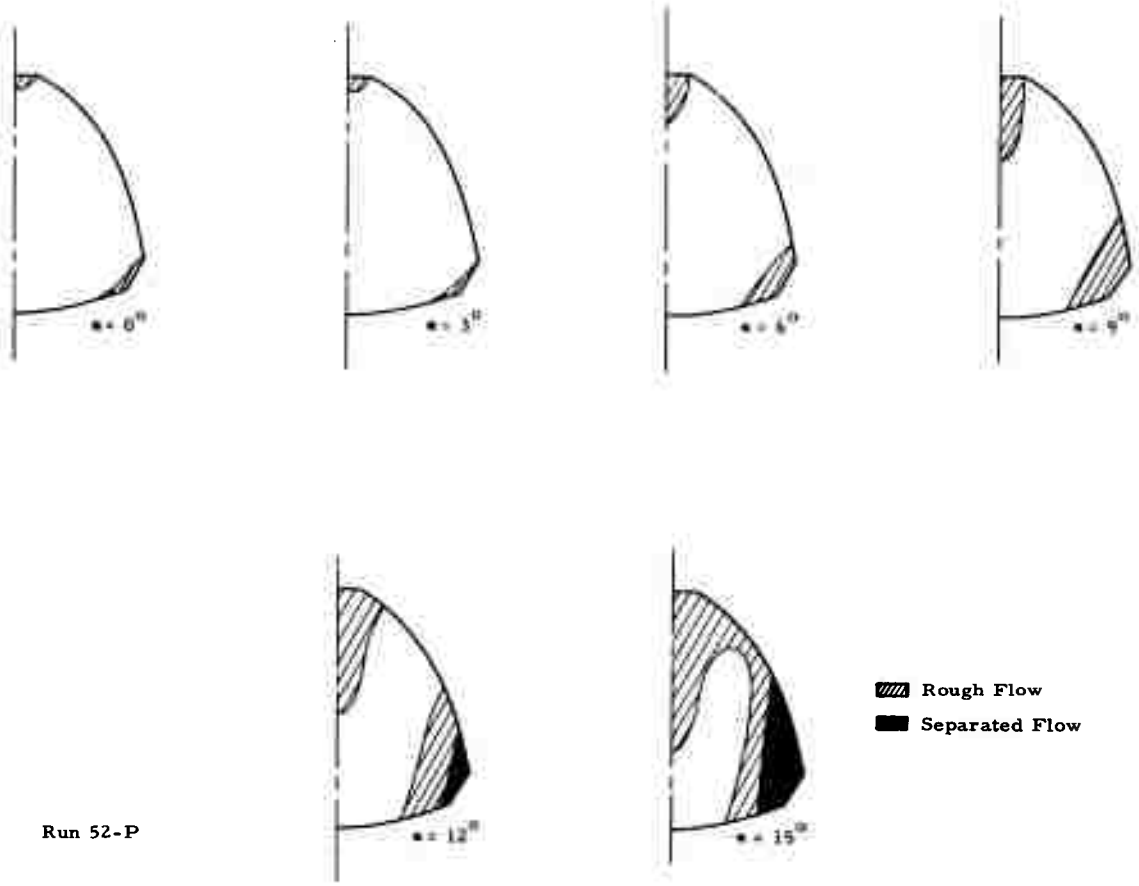

Figure 51. Rotor/Wing Stopped-Rotor Stall Pattern - Short-Nosed Fuselage - All Blades Off

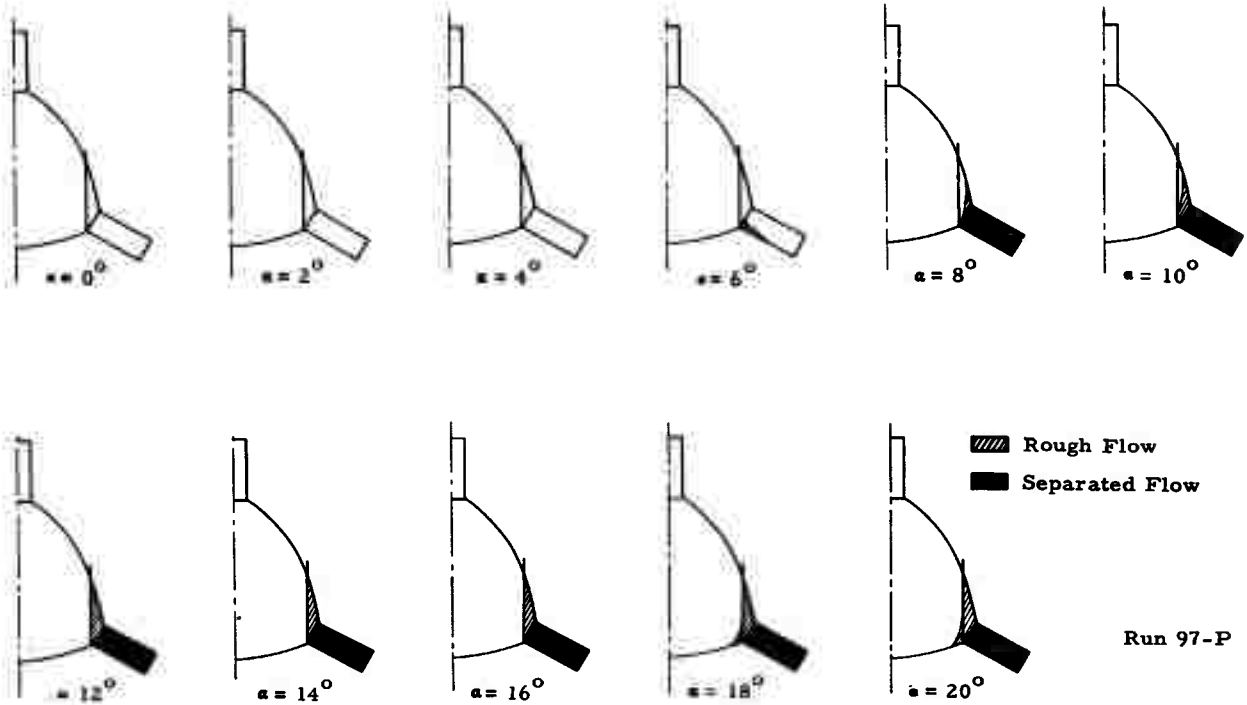

Figure 52. Rotor/Wing Stopped-Rotor Stall Pattern - Long-Nosed Fuselage - Wing Fences

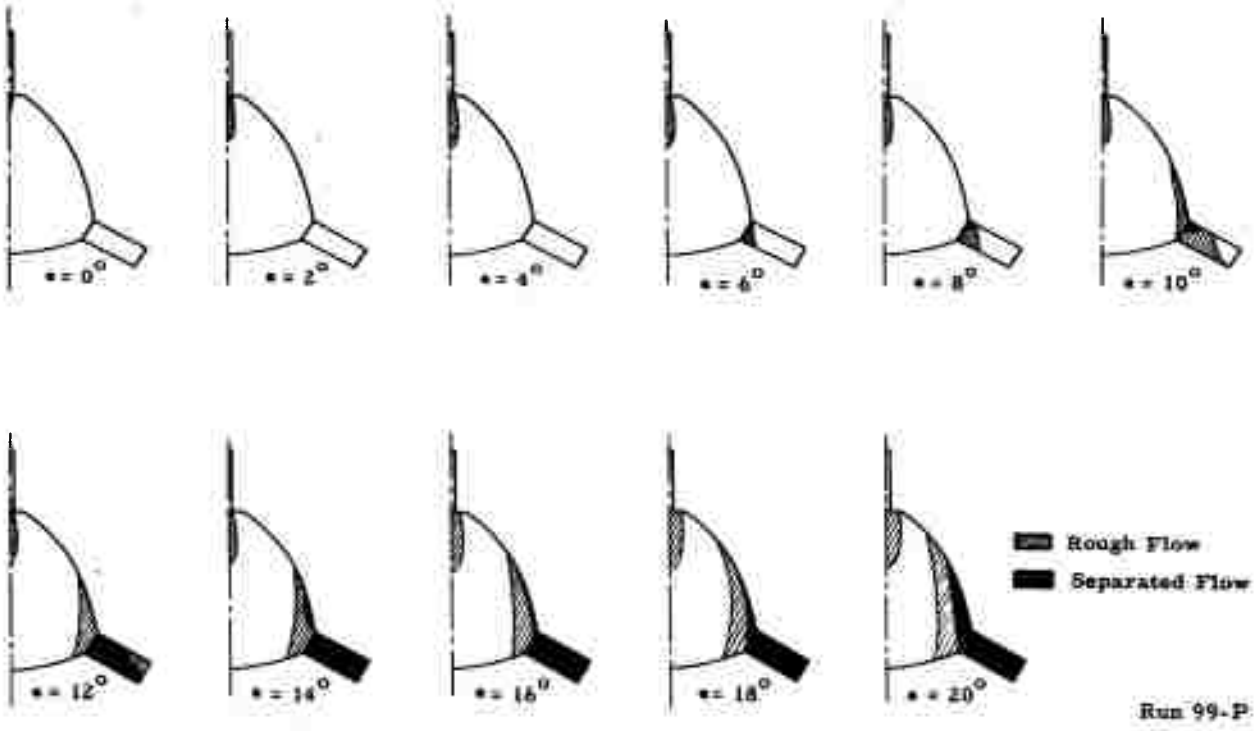

Figure 53. Rotor/Wing Stopped-Rotor Stall Pattern - Short-Nosed Fuselage - Forward Blade Incidence = 90° - Aft Blade Incidence = -10°

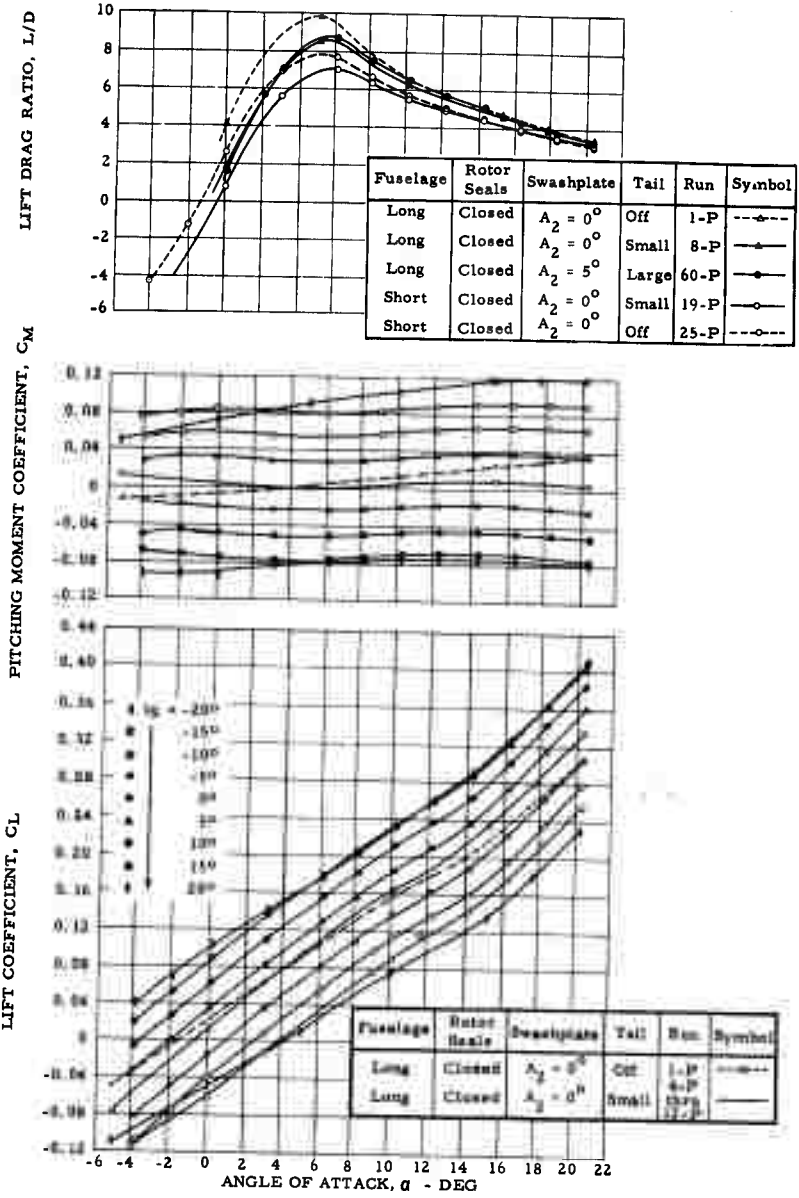

Figure 54. Stopped-Rotor Aerodynamic Characteristics

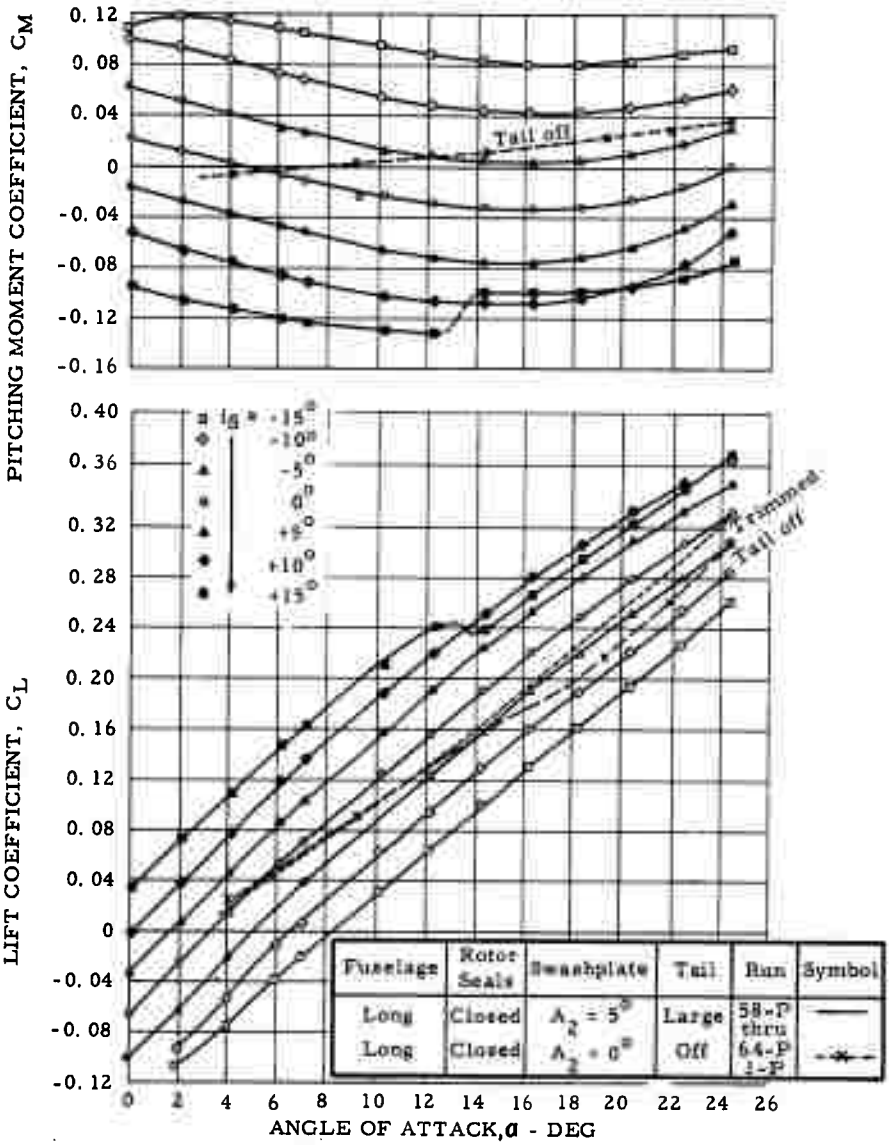

Figure 55. Lift and Pitching Moment Characteristics

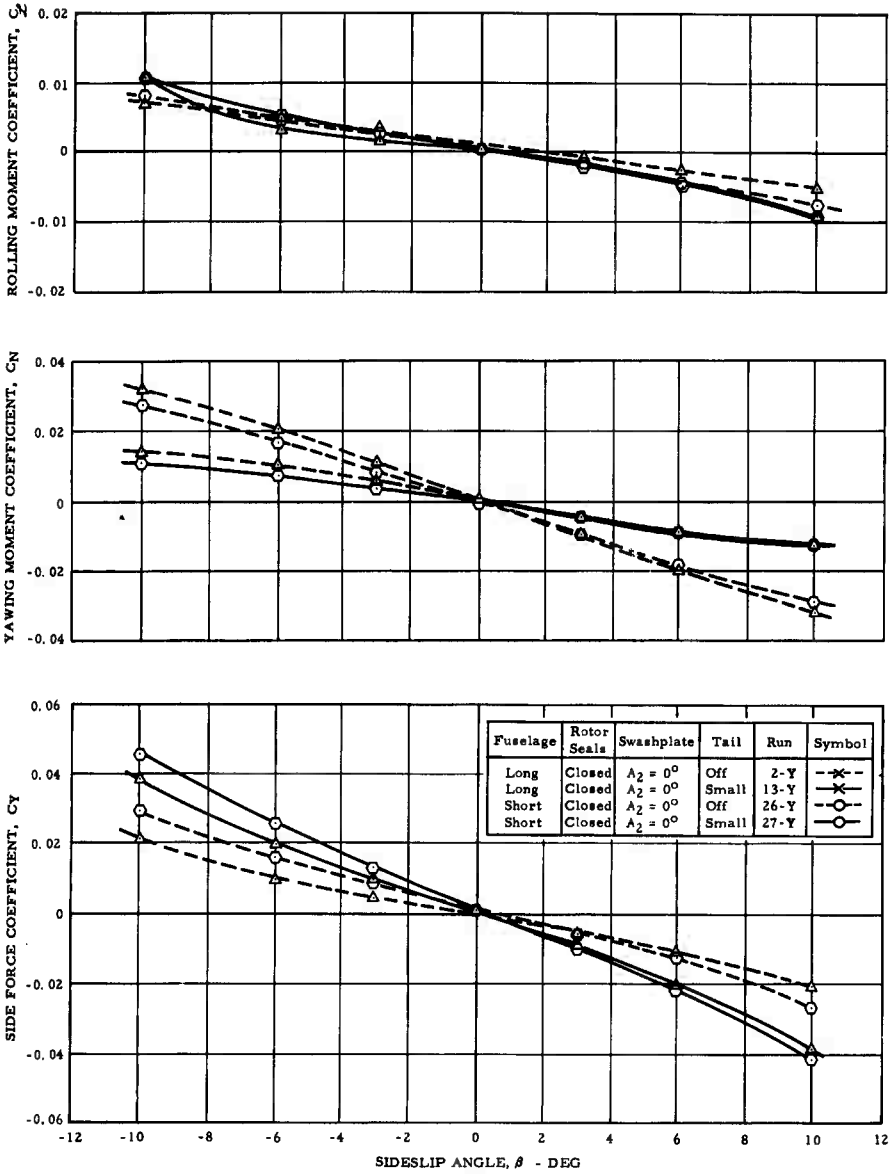

Figure 56. Lateral-Directional Stability Characteristics

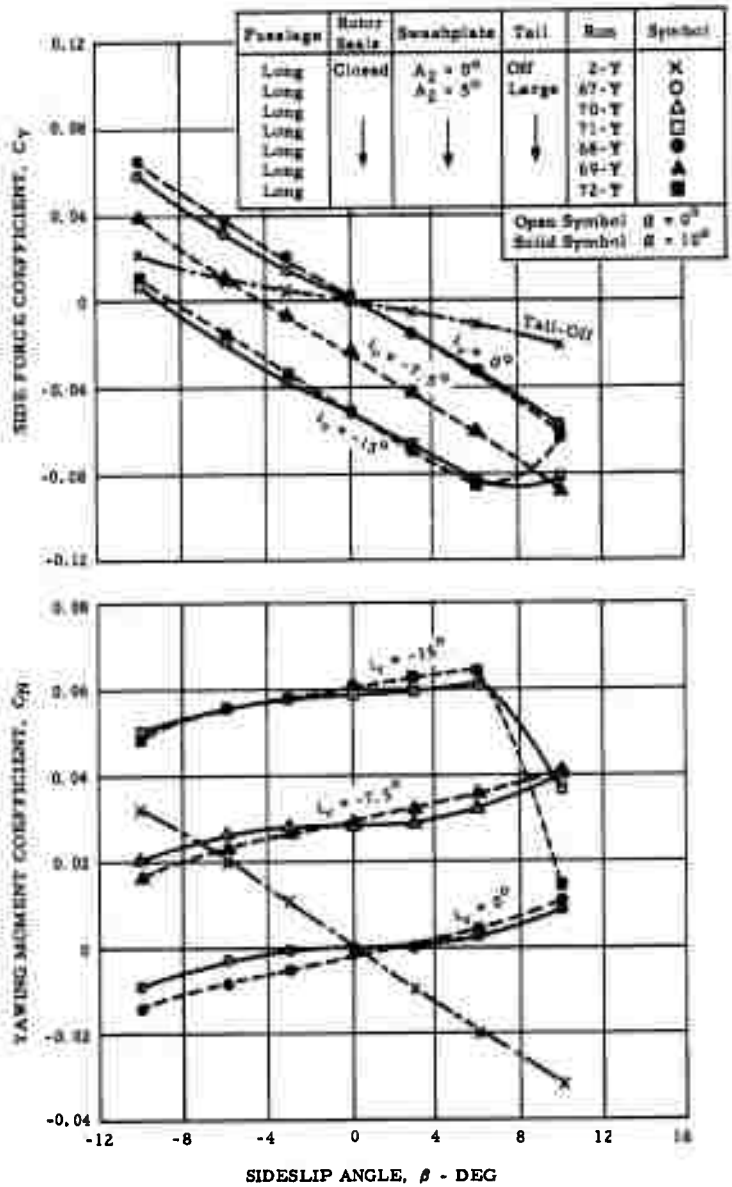

Figure 57. Vertical Tail Sidewash Study

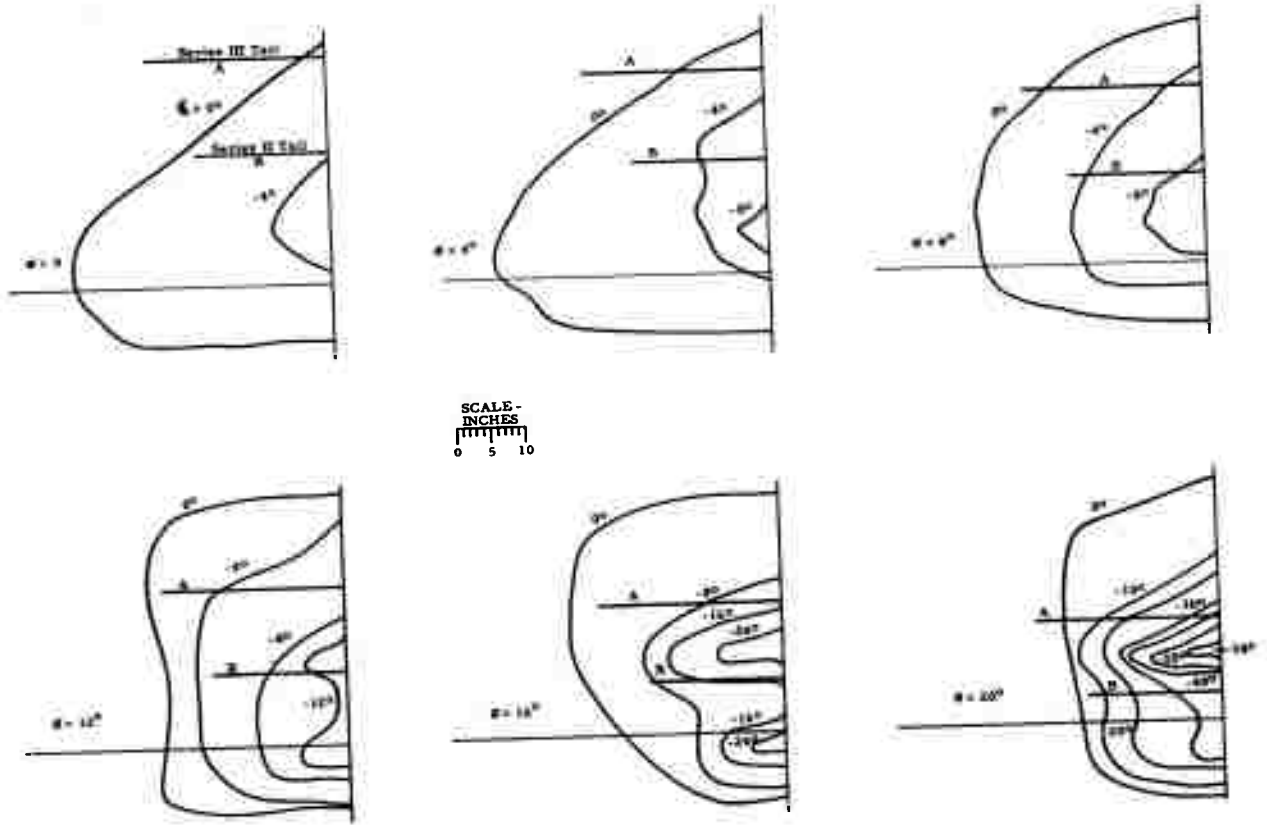

Figure 58. Dynamic Pressure Ratio at Tail

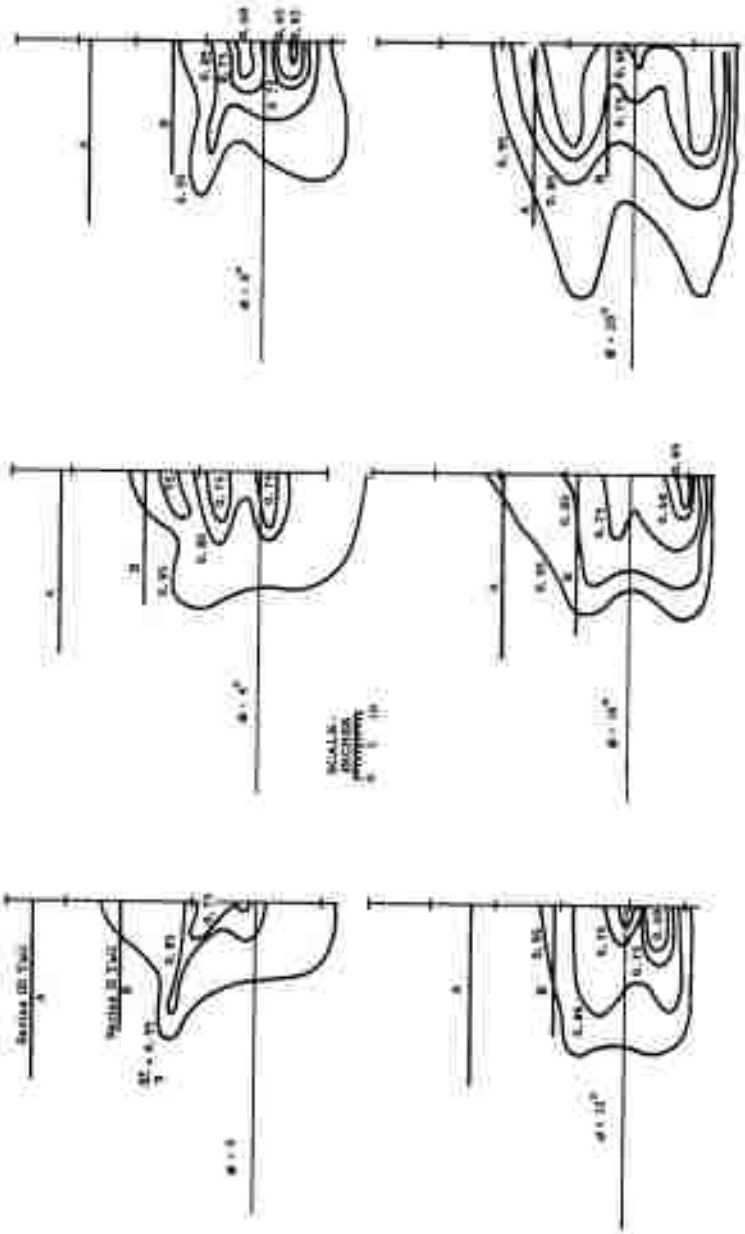

Figure 59. Downwash Angle at Tail

Fuselage	Rotor Seals	Swashplate	Tail	Run	Symbol	θ	$\Delta\delta$ Tail
Long	Open	$A_2 = 0^\circ$	Off	15-P	⊙	10°	—
Long	↓	$A_2 = 0^\circ$	Off	16-P	●	19°	—
Long	↓	$A_2 = 0^\circ$	Small	17-P	⊡	0°	12°
Long	↓	$A_2 = 0^\circ$	Small	17-P	■	0°	22°
Long	↓	$A_2 = 5^\circ$	Large	65-P	△	0°	10°
Long	Open	$A_2 = 5^\circ$	Large	66-P	▲	0°	20°

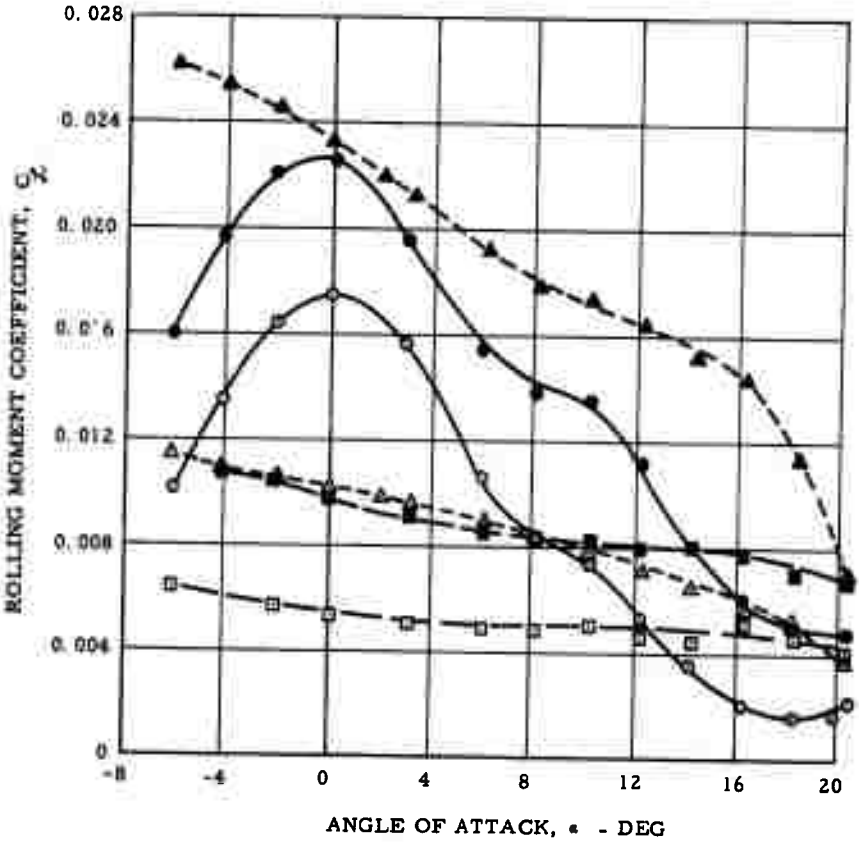

Figure 60. Roll Control Effectiveness

APPLICATIONS TO FULL-SCALE ROTOR/WING AIRCRAFT

The wind tunnel model was designed to be approximately one-sixth scale for a hypothetical ASW aircraft, Figure 61, that has a 43-foot diameter Rotor/Wing and a design gross weight of 20,000 pounds. This section of the report is devoted to describing the performance and flying qualities of such a full-scale aircraft, based on the model data.

The wind tunnel model was an outgrowth of the original whirlstand Rotor/Wing model. It was built to have extremely high stiffness, in order that no aeroelastic flutter problems could occur to delay the test program. When the Rotor/Wing was adapted to the wind tunnel model, its mass and inertia were reduced somewhat, but its level of stiffness remained. This permitted the rotating Rotor/Wing to run at speeds well below the three-per-rev resonance, so that airload moments on the hub could be read out as rotor shaft bending moments without the confusion of phase shifts, resonance, and so forth, that prevents the use of this kind of readout in more conventional rotors.

The model was instrumented to read blade loads, vibrations, and so forth, but these are not directly applicable to full-scale because of the lack of dynamic similarity between model and full-scale. To show the disparity in dynamic characteristics between this model and a hypothetical full-scale Rotor/Wing whose linear dimensions are six times those of the wind tunnel model, the characteristics of the wind tunnel

model and one Rotor/Wing preliminary design are compared in Table 3. To facilitate comparison, the characteristics are nondimensionalized by dividing by the following factors:

Length, L	Radius, R
Force, F	$\rho g \pi R^3$
Mass moment of inertia, I	$\rho \pi R^5$
Stiffness, EI or GJ	$\rho \pi \Omega^2 R^6$

Where ΩR model = 225 fps (600 rpm), ΩR full-scale = 700 fps, and $\rho = 0.00238$ slug/ft^3.

Table 3. Model/Full-Scale Dynamic Comparison

Item	Model	Full-Scale
Hub weight, $\overline{W}_H$	5.70	1.04
Blade weight per unit length, $\overline{w}_{bl}$	0.211	0.117
Rotor polar moment of inertia, $\overline{I}_z$	0.656	0.321
Blade root torsional stiffness, $\overline{GJ}$	0.0328	0.0302
Blade root flapwise stiffness, $\overline{EI}_{xx}$	0.0408	0.0378
Blade root chordwise stiffness, $\overline{EI}_{yy}$	0.0408	0.0378
Blade flapwise stiffness, $\overline{EI}_{xx}$	0.0408	0.0082
Blade chordwise stiffness, $\overline{EI}_{yy}$	0.0408	0.1995
Hub center flapwise stiffness, $\overline{EI}_{xx}$	0.4980	0.2250
Hub edge flapwise stiffness, $\overline{EI}_{xx}$	0.4020	0.1000

For good dynamic similarity, the two columns of numbers should be almost identical; since they are not, the blade loads, natural frequencies, and so forth, measured in the Rotor/Wing model cannot be directly applied to full-scale. Since the dynamic characteristics are so different, only trends are indicated by the model tests.

Predicted performance for the full-scale Rotor/Wing aircraft over its entire speed range at standard sea level is given in Figure 62 for the hypothetical ASW VTOL aircraft. Three curves for each flight regime are shown:

a. Model enlarged to full-scale

b. Full-scale aircraft with low-drag fuselage and improved blade profile power factor

c. Full-scale aircraft with low-drag fuselage, improved blade profile power factor, and blade length increased to 45 percent radius (model had 40 percent)

One major difference between the Rotor/Wing aircraft and other high-speed VTOL vehicles may be shown by Figure 62. High disc-loading VTOL's require a great amount of power for vertical flight – approximately the same as for high-speed cruise, because of the hovering inefficiency of the powerplant. The Rotor/Wing, on the other hand, hovers at a relatively low power level. Thus, landing, takeoff, and maneuvering at low speeds can be readily accomplished without the huge fuel expenditure of the high disc-loading machines.

The model test data upon which this performance is based was taken at very low Mach numbers. The relatively thick hub and blades in the model configuration can be expected to have a critical drag-rise Mach number of approximately 0.7. Investigations of critical Mach number effects and means to delay them should be the subject of further research.

Figure 63 shows that model test data in the helicopter mode agree well with NACA rotor theory (Reference 3 and 4), modified to account for the special conditions of the Rotor/Wing when a profile power factor of 1.3 is assumed.

A reduction in rotor blade profile power factor to 1.15 for the full-scale aircraft appears reasonable in light of Hughes studies of model and full-scale helicopter rotor blades.

Figure 64 presents the results of model tests in the stopped-rotor mode with lengthened blades relative to the hub size, and also shows the expected gains when going to full-scale with a low-drag fuselage. These data are the basis for the curve for the lowest airplane mode power required, in Figure 62. The model test data (Figure 54) indicates that the trimmed lift coefficient for $(L/D)_{max}$ is 0.095 for the reference aircraft. This corresponds to an indicated airspeed of 205 knots (205 knots TAS at sea level to 370 knots TAS at 35,000 feet).

Going to lengthened blades can have another beneficial effect in addition to the improved L/D ratio in airplane flight; that is, increased figure of merit in hovering. Figure 65 shows this increase in efficiency for the model; the upper chart compares model figure of merit with the improved figure of merit when going to full-scale. This scale effect is based on Hughes rotor aerodynamics studies and Reference 3. Detailed design studies would be needed to assess these benefits in relation to the weight, balance, and overall length of the aircraft required as a result of lengthening the blades.

Conversion of the full-scale aircraft between the running- and stopped-rotor modes should be a relatively simple maneuver. It is envisioned to take place as follows:

Helicopter-to-Airplane

1. Fly up to approximately 100 knots in the helicopter mode
2. Shift power from the rotor to the propulsion jets; maintain level flight and reduce collective pitch to maintain rotor speed. Increase airspeed to 150 knots.

3. Pull up collective pitch to stop the rotor. Maintain level flight with the cyclic pitch. (Quick rotor stops may be made by diverting a portion of the engine exhaust gas to reverse-thrust nozzles on blade tips.)

4. When rotor is nearly stopped, engage positioning motor to drive rotor into desired orientation. Lock the rotor. (If exhaust gas braking is used, gas must be diverted to propulsion jets before engaging positioning motor.)

5. Close rotor seals and fly as a fixed-wing jet airplane.

Airplane-to-Helicopter

1. Slow down to 150 knots in airplane flight. Open rotor seals.

2. Unlock rotor and immediately depress collective pitch lever to approximately the minus ten degree position to make rotor accelerate. (All the engine exhaust gas may be diverted to the rotor to aid in acceleration.) Maintain level flight with the cyclic stick.

3. As soon as rotor reaches governed rotor speed, fly as a helicopter.

No tests were made to determine the aircraft stability in pitch during conversion. The closest estimation that can be made must be taken from the stability in the autogyro and helicopter modes. Figures F-23 and F-26 indicate that the model was neutrally stable in pitch for both modes, with the center of gravity located on the rotor shaft. Hence, certain refinements of a final design would be necessary, to assure positive stability.

When the rotor is accelerating or decelerating through the conversion, it is sure to run through a number of resonances. The most objectionable, from the pilot's point of view, will probably occur at the very low rotor speeds, especially where the rolling response of the entire aircraft could couple with the rolling moment inputs from the Rotor/Wing. The low-rpm

rolling moment data of Figure 37 were converted to angular motion for the full-scale aircraft and are presented in Figure 66. These amplitudes were computed assuming no damping; even so, they are small enough that they should not cause the flight crew any great discomfort, because even the largest angles occur for only a very short time, especially if engine power is used to start and stop the rotor.

All the pitching moments discussed in this report were measured about a point on the rotor shaft. For hovering, this would be the ideal position for the center of gravity, but it is aft of the Rotor/Wing aerodynamic center when the rotor is locked. As a compromise, the center of gravity should be located approximately halfway between the rotor center and the aerodynamic center. There is adequate control power in hover to accommodate this offset cg, and a smaller tail would be required to balance the aircraft in stopped-rotor flight.

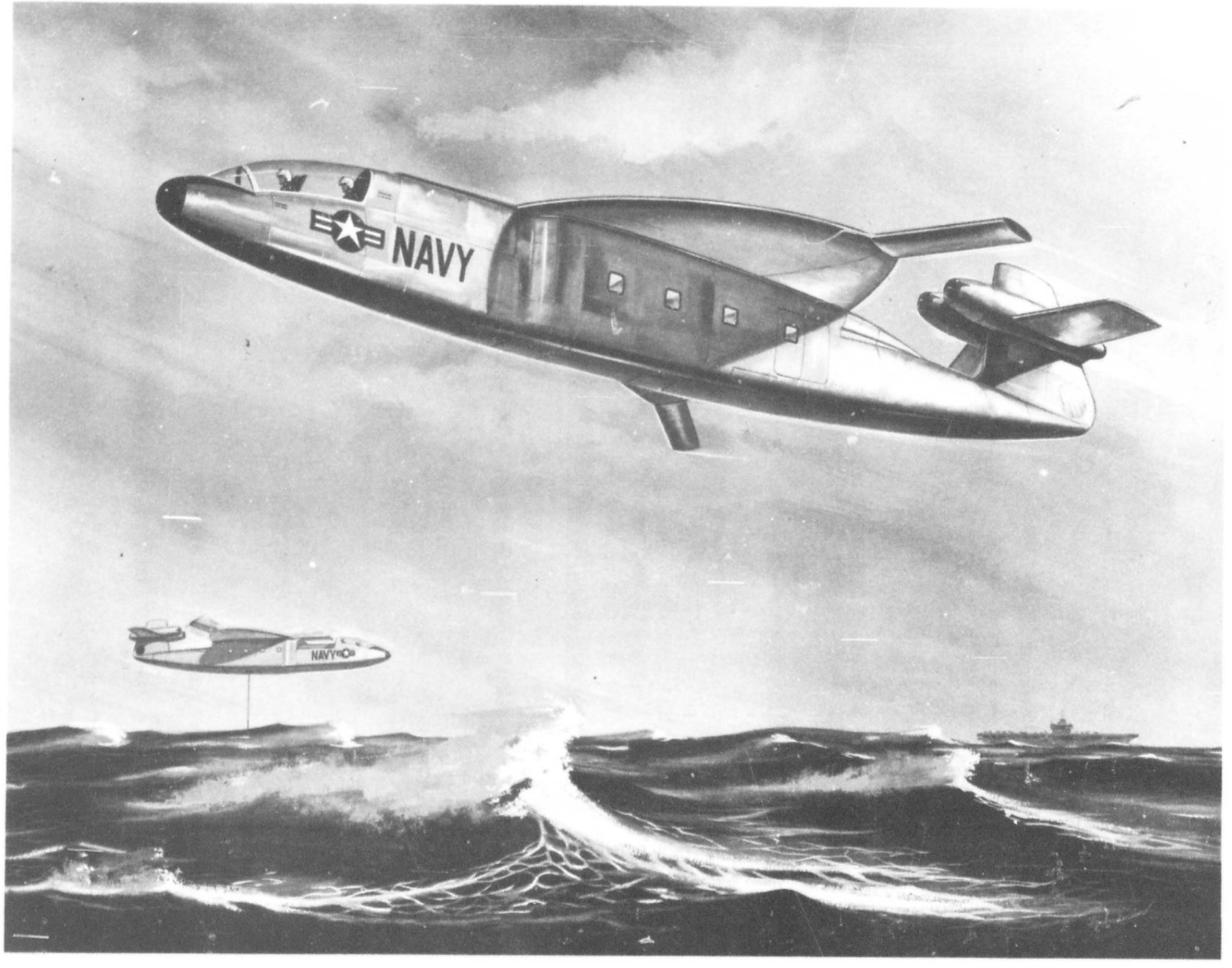

Figure 61. Hot Cycle Rotor/Wing VTOL ASW Aircraft

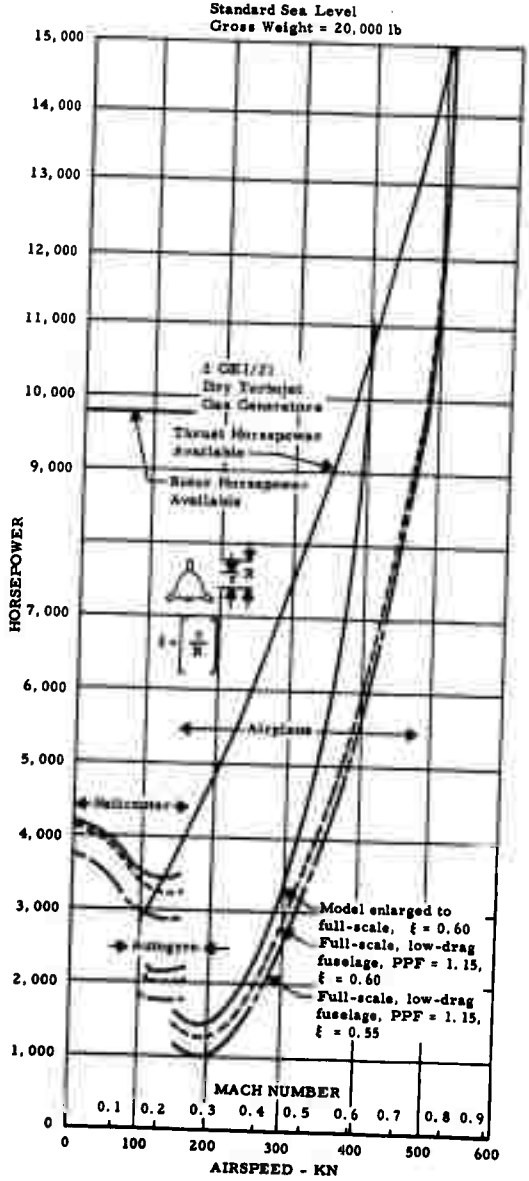

Figure 62. Full-Scale Rotor/Wing Performance

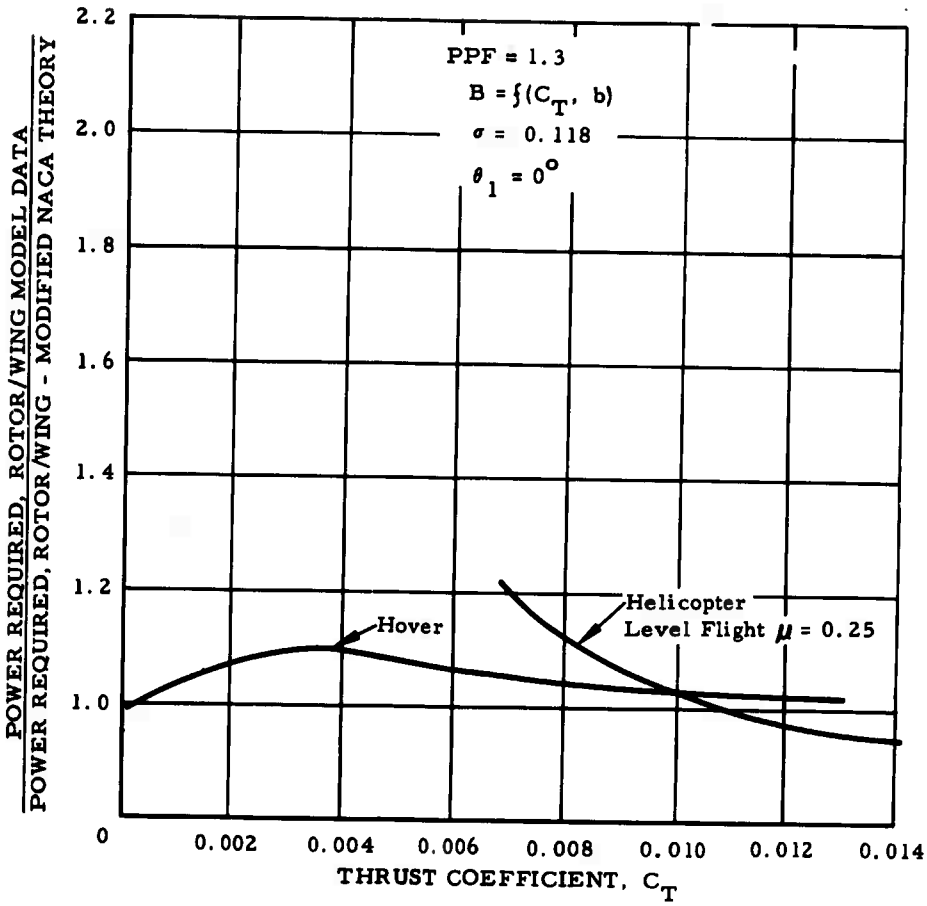

Figure 63. Ratio of Power Required by Rotor/Wing Model to Power Required by Modified NACA Theory

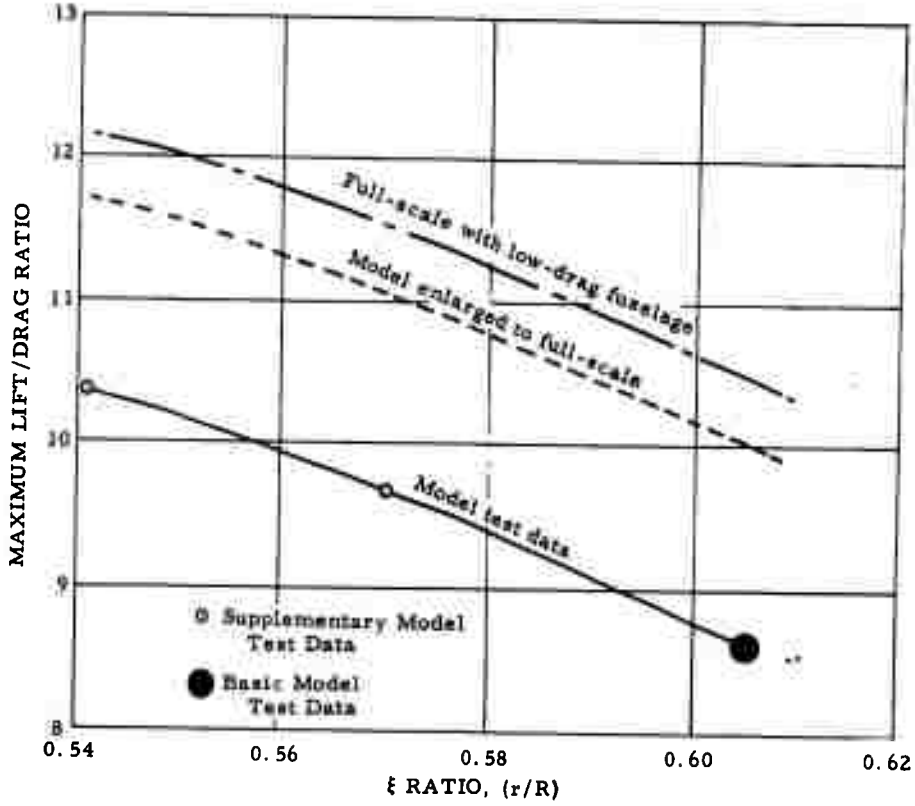

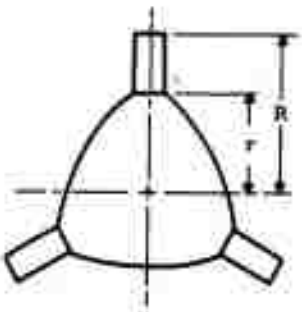

$\xi = r/R$

Figure 64. Estimated Maximum Trimmed Lift/Drag Ratio

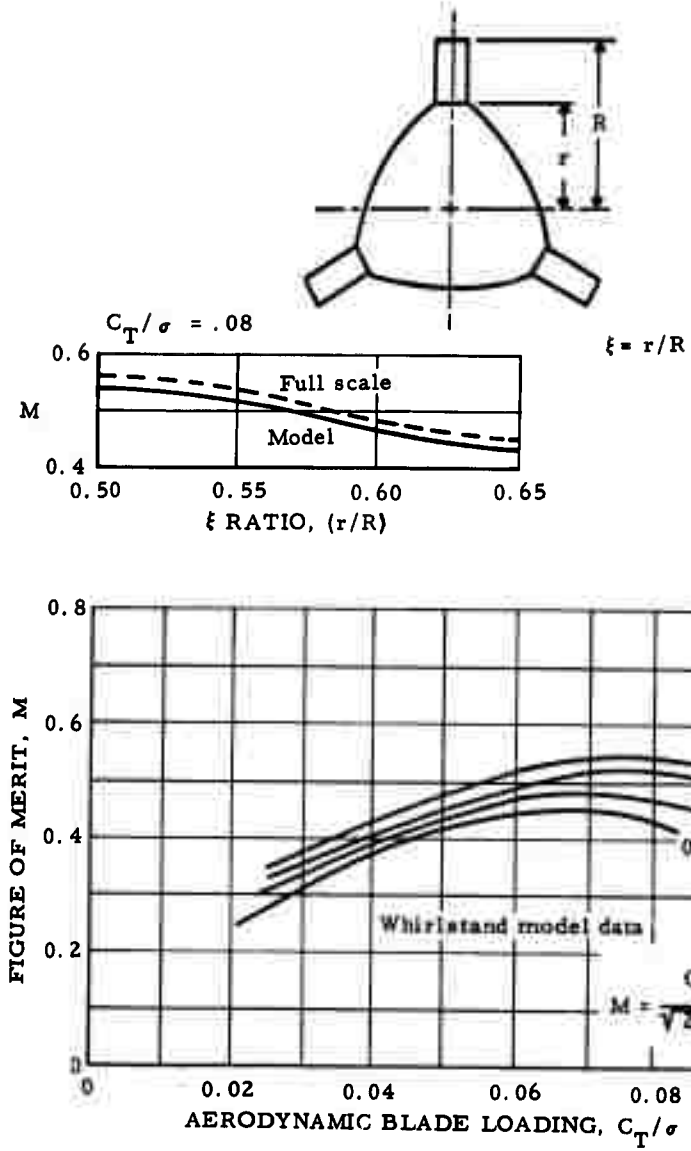

Figure 65. Hovering Figure of Merit

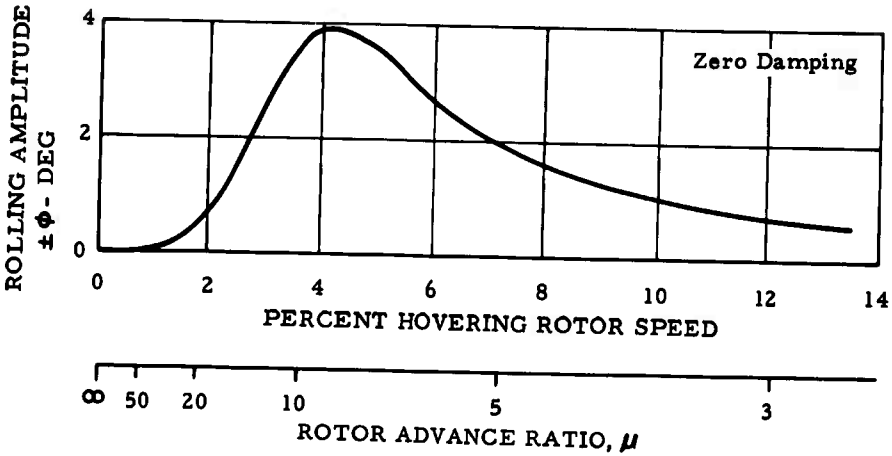

Figure 66. Aircraft Rolling Amplitudes During Conversion

CONCLUSIONS AND RECOMMENDATIONS

The analyses, whirlstand tests, and wind tunnel tests conducted with the Rotor/Wing model during this research program have shown that the performance and control in the running-rotor modes — hovering, helicopter, and autogyro — are quite similar to those of a high-performance helicopter, but with a power penalty of approximately 25 percent. This is thought to be an acceptable price to pay for a low-disc-loading VTOL aircraft that can fly efficiently at speeds up to approximately 0.8 Mach number. In the stopped-rotor mode, the Rotor/Wing behaved approximately like a delta-wing aircraft with a maximum L/D of more than 10 for full scale.

Conversion in flight between the running- and stopped-rotor modes was shown to be a simple and straightforward procedure. Test results indicate that the pilot can fly through this maneuver, both starting and stopping the rotor, without the need for special automatic equipment.

On the basis of these test results, the following configuration is recommended:

Long-nosed fuselage into which the forward blade is faired for cruise (fairing doors retract for clearance when the rotor turns)

Aft rotor blades moved to a small nose-down incidence for cruise and held fixed

All-movable horizontal tail mounted high on the vertical tail to act as both elevators and ailerons

In view of the favorable test results obtained during this program, it is recommended that consideration be given to continuing the research through investigations of a general-purpose dynamic model that would permit exploring rotor and control loads, vibration, and flutter for a spectrum of Rotor/Wing aircraft configurations. Further consideration should be given to high-Mach-number testing in the stopped-rotor mode, to investigate the aerodynamic characteristics in this speed range.

In view of the favorable test results obtained during this program, it is recommended that consideration be given to continuing the research through investigations of a general-purpose dynamic model that would permit exploring rotor and control loads, vibration, and flutter for a spectrum of Rotor/Wing aircraft configurations. Further consideration should be given to high-Mach-number testing in the stopped-rotor mode, to investigate the aerodynamic characteristics in this speed range.

REFERENCES

1 Anon, Contract for Research and Development on Rotor/Wing Concept Study, Contract Nonr-4588(00), Office of Naval Research, dated 29 June 1964.

2 Anon, Interim Report, Rotor/Wing Concept Study, Hughes Tool Company - Aircraft Division Report 64-38, October 1964.

3 LaForge, S. V., Performance Handbook, Hughes Tool Company - Aircraft Division Report XA-8016, January 1965.

4 Gessow, A. and Myers, G. C., Jr., Aerodynamics of the Helicopter, The Macmillan Company, 1952.

5 Gessow, A. and Tapscott, R. J., Charts for Estimating Performance of High-Performance Helicopters, NACA Report 1266, 1956.

6 Frost, R. C. and Rutherford, R., Subsonic Wing Span Efficiency, AIAA Journal, April 1963.

7 LaForge, S. V., Effect of Blade Stall on Rotor and Control System Loads, Hughes Tool Company - Aircraft Division Report 62-59, April 1963.

8 Bisplinghoff, R. L., Principles of Aeroelasticity, John Wiley and Sons, Inc., 1962.

9 Hall, C. F., Lift, Drag, and Pitching Moment of Low-Aspect-Ratio Wings at Subsonic and Supersonic Speeds, NACA Research Memorandum RM A53A30, 14 April 1953.

Unclassified

Security Classification

DOCUMENT CONTROL DATA - R&D

(Security classification of title, body of abstract and indexing annotation must be entered when the overall report is classified)

1. ORIGINATING ACTIVITY *(Corporate author)*
Hughes Tool Company - Aircraft Division
Culver City, California

2a. REPORT SECURITY CLASSIFICATION
Unclassified

2b GROUP
X

3. REPORT TITLE

SUMMARY TECHNICAL REPORT, ROTOR/WING CONCEPT STUDY
(Volumes I, II, and III)

4. DESCRIPTIVE NOTES *(Type of report and inclusive dates)*
Summary Report

5. AUTHOR(S) *(Last name, first name, initial)*

Head, Robert E.

6. REPORT DATE	7a. TOTAL NO. OF PAGES	7b. NO. OF REFS
September 1965		9

8a. CONTRACT OR GRANT NO.	9a. ORIGINATOR'S REPORT NUMBER(S)
Nonr-4588(00)	HTC-AD 65-15
b. PROJECT NO. NR-212-162/12-8-64	
c.	9b. OTHER REPORT NO(S) *(Any other numbers that may be assigned this report)*
d.	---

10. AVAILABILITY/LIMITATION NOTICES
U. S. Government agencies may obtain copies of this report directly from DDC. Other qualified DDC users shall request through Air Programs, Office of Naval Research, Washington, D. C. 20360

11. SUPPLEMENTARY NOTES	12. SPONSORING MILITARY ACTIVITY
	U. S. Navy, Office of Naval Research and Bureau of Naval Weapons

13. ABSTRACT

Research work including wind tunnel and whirl test of the Rotor/Wing is described. The Rotor/Wing is a dual-purpose lifting device that is a rotor with an unusually large hub. It acts as a tip-jet powered helicopter for low-speed flight and stops in flight to become a tapered and sweptback low-aspect ratio wing for cruise. Stopping the rotor in flight removes the speed limitations of the helicopter rotor and permits flight speeds up to 500 knots. Research work was supported by the U. S. Navy Office of Naval Research and Bureau of Naval Weapons. Three series of wind tunnel tests demonstrated that the powered-rotor and autorotating-rotor characteristics are similar to those of a high-performance helicopter; that the stopped-rotor characteristics are similar to a conventional low-aspect ratio wing with sweep and taper, and maximum lift/drag ratios of 12 or more should be achievable for full-scale aircraft; and that conversion from stopped- to running- rotor and vice versa is a simple and straightforward procedure.

DD FORM 1 JAN 64 1473

Unclassified
Security Classification